Subgrid is Dancing with Sediment

A Full Subgrid Approach for Morphodynamic Modelling

Volp, Nicolette

DOI
10.4233/uuid:271c4360-e242-42aa-8974-72fe012365ee

Publication date
2017

Document Version
Final published version

Citation (APA)
Volp, N. (2017). *Subgrid is Dancing with Sediment: A Full Subgrid Approach for Morphodynamic Modelling*. [Dissertation (TU Delft), Delft University of Technology]. https://doi.org/10.4233/uuid:271c4360-e242-42aa-8974-72fe012365ee

Subgrid is Dancing with Sediment

A Full Subgrid Approach for Morphodynamic Modelling

Subgrid is Dancing with Sediment

A Full Subgrid Approach for Morphodynamic Modelling

Proefschrift

ter verkrijging van de graad van doctor
aan de Technische Universiteit Delft,
op gezag van de Rector Magnificus prof.ir. K.C.A.M. Luyben,
voorzitter van het College voor Promoties,
in het openbaar te verdedigen op
dinsdag 10 januari 2017 om 10:00 uur

door

Nicolette Dominique Volp

geboren te Hellevoetsluis, Nederland

Dit proefschrift is goedgekeurd door de

promotoren:	Prof. dr. ir. G.S. Stelling and Prof. dr. J. D. Pietrzak
copromotor:	Dr. ir. B. C. van Prooijen

Samenstelling promotiecommissie:

Rector Magnificus,	Voorzitter
Prof. dr. ir. G. S. Stelling,	Technische Universiteit Delft, promotor
Prof. dr. J. D. Pietrzak	Technische Universiteit Delft, promotor
Dr. ir. B. C. van Prooijen	Technische Universiteit Delft, copromotor
Onafhankelijke leden:	
Prof. dr. S. Allen	The University of Britisch Columbia
Prof. dr. ir. A. W. Heemink	Technische Universiteit Delft
Prof. dr. ir. H. J. de Vriend	Technische Universiteit Delft
Prof. dr. ir. A. Malcherek	Universität der Bundeswehr München
Overig lid:	
Prof. dr. ir. A. J. H. M. Reniers	Technische Universiteit Delft, reservelid

Printed by: Gildeprint
Front cover: Waddenzee

ISBN 978-94-6233-506-6

An electronic version of this dissertation is available at
http://repository.tudelft.nl/

Voor Coen Volp

Preface

Imagine yourself sitting in a comfortable chair with your feet in the sand and looking over the water. Listen to the rhythm of the flow. Look at the way the flow moves and let your imagination go. Imagine being with the flow and see how he follows the contours of the bed. Observe how he temps the sediment to join him on his journey. First, nothing seems to happen. But wait, slowly, very slowly some sediment stirs. The flow picks it up, leads it away, it floats, it swirls and settles down. Now, her contours guide him into a new direction. Allowing him to tempt the sediment again. The flow leading the sediment, but he follows the bed, while she adapts to the flow. Together, they form the dance of the sediment. Let's join them in their dance.

Nicolette Dominique Volp
Delft, 2016

Contents

Summary

This thesis presents a fast and accurate method to model the hydrodynamics and morphodynamics of estuarine, riverine and coastal regions. The method aims at increasing the accuracy of simulations, for a limited increase in computational effort. This type of models are essential for a wide range of applications. At one end of the spectrum, fast results are necessary for, for example, flooding models in case of an emergency. At the other end of the spectrum, fast models are required for long term morphodynamic studies. Three phases can be distinguished in this research. Firstly, the accuracy of hydrodynamic models was improved. We continued by computing accurately the variation of the bed level in time. In the third phase, we focussed on determining the sediment concentration in combination with updating the bed level.

The computational effort is strongly related to the resolution of the computational grid, whereas the resolution significantly affects the accuracy. Even though computer power still increases, the computational effort of numerical models remains an issue. Furthermore, high resolution information of the bed level and the material become increasingly available. This type of data gives important insight in the characteristics of an estuarine, riverine or coastal environment, but often, it can not optimally be used in numerical studies. Therefore, we developed a method, that can make use of this high resolution information in hydrodynamic and morphodynamic computations, a so-called subgrid based method.

The hydrodynamic method presented in this thesis is inspired by the subgrid based approach developed by Casulli. Water levels generally vary only gradually in space, while the bathymetry, and therefore the depth, changes much more rapidly. Even when one is interested in large scale processes, an accurate description of the bed is crucial. Therefore, this type of model makes use of two grids, a (coarse) computational grid and a high resolution subgrid. At the subgrid, the high resolution (for example bathymetry and roughness) information is defined, while the computation of water levels and velocities is performed at coarse grid. By taking high resolution information into account, when solving the continuity and the momentum equations, the solution based on a coarse computational grid improves significantly. This result is obtained without a significant increase in computational cost.

For a fast and accurate method that computes the morphodynamics, the high resolution bathymetry information needs to be updated. A relation, between the coarse hydrodynamic variables and those variables defined on the high resolution subgrid, is required. High resolution water levels and water depths can be defined by interpolation, based on the bathymetry and the coarse grid water levels. However, one of the more difficult challenges was the interpolation of the velocity field. Here, an algebraic expression for the velocity on high resolution is formulated. This new

formulation is based on the coarse grid velocity, the coarse grid water level, the high resolution bathymetry and friction coefficients. The expression is based on the continuity equation and a simplified momentum equation, in which a local balance between pressure gradient and friction is assumed.

The bed evolution can be computed by solving the sediment mass balance, the so-called Exner equation. Variations in sediment fluxes determine the bed level variation. The fluxes are usually based on bed shear stresses, due to the flow velocity. By defining the flow velocity at high resolution, the sediment mass balance can be solved fully on high resolution under the assumption that lag effects are neglected. This allows to update the high resolution bathymetry.

For applications where lag effects are important, the net erosion or sedimentation depends on the capacity of the flow to keep sediment in suspension. The exchange rate of sediment between the domain of the bed and the water column depends on characteristics of the flow and the sediment. These are parametrized as terms in the bed evolution equation and in a sediment transport equation.

The transport equation for suspended sediment is resolved on the coarse grid to ensure no extra time step restrictions. However, the exchange terms need to be defined on high resolution, because the bed evolution equation is still to be solved at high resolution. Moreover, when computing the sediment concentration, high resolution effects are accounted for, as this increased the accuracy. The total increase in computational effort remained limited.

Another major challenge is the stability of morphodynamic simulations, as they are sensitive to numerical instabilities. This is because there is no natural damping term in the bed evolution equation. To improve the stability of the solution, the method to discretise the equations is changed, by defining the upwind direction based on the bed celerity. This is an alternative to the general method of choosing the upwind direction based on velocity or transport direction. It is shown that in some areas these two can oppose each other. In such a case, choosing the upwind direction based on velocity, is in principle an unstable downwind method.

We presented in three steps, a new subgrid based method for morphodynamics. The computed water levels, flow velocities, sediment concentrations and bed level variation improved due to a combination of factors. Firstly, the hydrodynamic solution is improved by taking high resolution information into account. Secondly, by an improved description of the forcing, a more accurate morphodynamic response is ensured. Moreover, by updating the high resolution bathymetry information, the accuracy of the hydrodynamic forcing is prolonged. This increase in accuracy allows simulations based on coarse grid resolution. We demonstrated a marked improvement for fast and accurate hydrodynamic and morphodynamic computations.

Samenvatting

Dit proefschrift beschrijft een nauwkeurige en efficiënte methode om de hydrodynamica en de morfodynamica van estuaria, rivieren en kustgebieden te kunnen modelleren. Deze methode kan voor vele toepassingen worden gebruikt. Deze variëren van de modellering van overstromingen bij een calamiteit tot de lange termijn berekeningen van morfologie. Het doel van de methode is om de nauwkeurigheid van berekeningen te laten toenemen, tegen een zo klein mogelijke toename in rekentijd. We kunnen het onderzoek splitsen in drie onderdelen. Het eerste onderdeel is het verbeteren van de nauwkeurigheid van hydrodynamische berekeningen. Daarna hebben we ons gericht op het nauwkeurig bepalen van bodemveranderingen in de tijd op hoge resolutie. Als derde onderdeel hebben we onderzocht hoe we naast het bepalen van bodemveranderingen ook de bepaling van de concentratie van sediment in de waterkolom konden verbeteren.

De rekentijd van simulaties is sterk afhankelijk van de resolutie van het rekenrooster, maar deze is ook in grote mate bepalend voor de nauwkeurigheid van de resultaten. Ondanks de continue toename van de snelheid van computers, is de rekentijd van berekeningen een beperkende factor. Daarnaast neemt de hoeveelheid informatie die we hebben over de bodem en bodembedekking toe, dankzij verbeterde meettechnieken. Deze informatie kan vaak niet optimaal gebruikt worden, wegens een te lange rekentijd terwijl, deze informatie sterk kan bijdragen aan de nauwkeurigheid. We hebben daarom een nieuwe methode ontwikkeld die deze hoge resolutie informatie kan gebruiken in hydrodynamische en morfologische berekeningen. Dit hebben we gedaan met een methode gebaseerd op subgrid.

De methode die we hier presenteren voor de hydrodynamica is geïnspireerd op de methode van Casulli. Ten grondslag van deze methode ligt dat over het algemeen geldt dat waterstanden minder variëren in de ruimte dan de bodem. Zelfs wanneer men geïnteresseerd is in grootschalige processen, is het belangrijk om een nauwkeurige beschrijving van de bodem te hebben. De op een subgrid gebaseerde methode maakt gebruik van twee roosters; een (grof) rekenrooster en een fijn rooster, het subgrid. Het fijne rooster bevat de hoge resolutie informatie van bijvoorbeeld de bodemhoogte en de ruwheid. Op het grove rooster worden de waterstanden en de snelheden berekend. Door de hoge resolutie effecten mee te nemen in zowel de continuïteitsvergelijking en nu ook in de impulsvergelijking, neemt de nauwkeurigheid sterk toe, zonder dat de rekentijd significant toe neemt.

Het tweede onderdeel was het vinden van een snelle en nauwkeurige methode om bodemveranderingen op hoge resolutie te bepalen. Dat betekent dat er een relatie moest worden gevonden tussen de hydrodynamische variabelen die gedefinieerd zijn op het grove rooster en de variabelen die gedefinieerd zijn op het fijne rooster. De waterstanden en waterdieptes kunnen op hoge resolutie worden bepaald door deze lineair te interpoleren. Het bepalen van snelheidsveld op hoge resolutie is moeilijker.

Op basis van de continuïteitsvergelijking en een versimpelde impulsvergelijking kan er een snelheidsveld worden bepaald op basis van de snelheid, gedefinieerd op het grove rooster, de geïnterpoleerde waterstand en de ruwheid, beide gedefinieerd op het fijne rooster. De versimpelde impulsvergelijking maakt een balans tussen de drukgradiënt en de wrijving.

De bodemverandering wordt bepaald door het oplossen van de massabalans voor sediment, de zogenaamde Exnervergelijking. De ruimtelijke variatie van sedimenttransporten bepaalt de bodemverandering. Het sedimenttransport is afhankelijk van de schuifspanning, die weer afhankelijk is van de snelheid van de stroming. Dankzij het geïnterpoleerde snelheidsveld, kan de bodemverandering op hoge resolutie worden berekend.

Voor bepaalde toepassingen wordt de netto erosie of sedimentatie (mede) bepaald door zwevend sedimenttransport. De hoeveelheid sediment die wordt uitgewisseld tussen de bodem en de waterkolom, hangt af van de stromings- en sedimenteigenschappen. De parametrisering van deze uitwisseling komt terug in zowel de vergelijking voor sedimentconcentratie als in de massabalans voor sediment. De vergelijking voor sedimentconcentratie wordt op het grove rooster opgelost, omdat er dan geen extra strenge tijdstaprestricties gelden om het systeem stabiel te houden. Desondanks moeten de uitwisselingstermen voor sediment tussen de waterkolom en de bodem wel op hoge resolutie worden gedefinieerd. Daardoor kan de bodemverandering op hoge resolutie worden berekend. Daarnaast wordt ook tijdens de berekening van de sedimentconcentratie hoge resolutie effecten verdisconteerd. Dit zorgt voor een toename in de nauwkeurigheid, zonder dat het de rekentijd beduidend laat toenemen.

Numerieke morfologische simulaties zijn gevoelig voor instabiliteiten. Dit komt doordat er van nature geen dempende term in de vergelijkingen zit. Om de stabiliteit te verbeteren hebben een nieuwe methode toegepast op de discretisatie van de massabalans voor sediment. We bepalen de 'bovenstroomse' richting op basis van de richting van de bodemkarakteristiek. Dit is in plaats van de richting van de snelheid of het sedimenttransport. Het blijkt dat in bepaalde situaties deze twee richtingen kunnen afwijken. Wanneer in zo'n situatie de bovenstroomse richting wordt bepaald op basis van de snelheidsrichting, dan wordt er eigenlijk een (instabiele) benedenstroomse methode toegepast.

De berekende waterstanden, snelheden, sediment concentraties en bodemveranderingen zijn verbeterd door een combinatie van factoren. Ten eerste, de hydrodynamische oplossing verbeterde door het gebruik van hoge resolutie informatie. Dit leidde tot een verbeterde beschrijving van de forcering van het sedimenttransport. Dit betekende dat ook de morfologische reactie nauwkeuriger bepaald kon worden. Bovendien kon met deze methode de bodemverandering op hoge resolutie worden berekend. Het voordeel van het gebruik van hoge resolutie informatie op de hydrodynamica kon hiermee worden behouden tijdens de morfologische veranderingen. De subgrid gebaseerde methode is een belangrijke stap voorwaarts richting snelle en nauwkeurige hydrodynamische en morfologische berekeningen.

1

Introduction

"The problem is not making up the steps but deciding which ones to keep."

Mikhail Baryshnikov

We will present a subgrid based approach for hydrodynamic and morphodynamic modelling. This approach is an efficient and accurate method to simulate flow and bed evolution in areas with sub-critical, friction dominated flow, as can be found in estuaries and low land rivers. In the last decades, numerous numerical methods have been developed, widely applied and improved. However, there are still various issues to be resolved to meet our need for faster and more accurate models. This thesis aims at making the next step to fulfil these needs. We will first discuss why numerical models are needed, some of the challenges that still need to be resolved and which of those will be tackled in this thesis.

1.1. Why start dancing?

Many of the most densely populated areas in the world can be found near river deltas, estuaries and coasts [1]. The Netherlands, Shanghai, Mississippi Delta and Jakarta are a few examples. Historically, these areas offer water, food and possibilities for transportation, but there has always been the risk of flooding. Due to a worldwide trend of urbanisation, other aspects than safety have become important. There is a competition for space between shipping, fisheries, agriculture, space for recreation and ecology. It is essential to guarantee safety and navigability, but also to maintain the water quality and protect the ecological system and preserve biodiversity. Climate change and human interventions (from the past, present and future) affect the deltaic system. Policy makers have to find a balance between these functions and predict the future changes. A sound understanding of the complex interaction between hydrodynamics, morphology and ecology is of utmost impor-

tance. Computer based models have proven to be essential tools for investigating these complex interactions in large areas over long periods of time.

Hydrodynamic and morphodynamic models are applied in a wide range of applications, time and spatial scales. By resolving water levels, currents and waves, the hydrodynamic models are used to forecast, for example, floods, storm surges and tsunamis. These models need to be fast and accurate when they need to supply the information for, for example, early warning systems. Efficient models are also required to simulate a range of possible measures for various conditions during the design phase of a flood protection project.

Morphodynamic models are used to predict the effects, of human intervention, such as channel deepening or the morphological evolution of an area. These models require the water levels and velocities computed by hydrodynamic models. Due to the long morphological time scales (years to decades), long simulation periods are needed. Therefore, the computational effort of this type of simulation is high and would benefit from efficient models too.

Over the years, numerous hydrodynamic and morphodynamic models have been developed for a wide range of applications. Improved computer power, new measurement techniques and better understanding of the physical system allow for different approaches, but also reveal new challenges.

1.2. So we think we can dance?

The development of numerical solutions for hydraulic problems started soon after the first computers were invented around 1944 [2]. Methods to find numerical solutions for large systems of equations needed to be developed. There was an issue of translating the set of continuous equations into a discrete system. This is claimed to be solved according to Abbott [3] by Lax [4]. However, the early laws of hydraulics go back to G. Galilei (1590). Many of the key principles that were developed in those early years are still applied today. Ever since, new approaches and techniques are introduced to improve the accuracy and the efficiency of hydrodynamic and morphodynamic models. For an overview of various types of methods and their differences see for example Wesseling [5] or Petrila and Trif [6].

The quality of the results of a numerical model depends on several aspects. Depending on the application and the objective of the model, some processes are more dominant than others. One can choose to account only for the most dominant processes, in order to improve the efficiency of the model. Obviously, the numerical implementation of these processes affect the solution too. Additionally, the quality of the physical parameters, like for example, roughness and bathymetry information, affect the overall quality of the solution. New measurement techniques, such as satellite imagery and LIDAR data, make high resolution information available [7]. Moreover, the type and the quality of the initial and the boundary conditions, strongly affect the model results, as these drive the dynamics.

For each model simulation, a choice has been made for the resolution of the grid. This is a crucial choice, for the quality of the results. When the resolution of the computational grid is too coarse, processes and the description of the flow domain are not described properly. For example, choosing a different grid resolution,

generally implies a different description of the bed, as there is only one bathymetry value defined. This has significant effects on the results. This holds also for the processes that are taken into account. Even though processes are implemented in the numerical description, when they are dominant at a scale smaller than the grid cells, then these will still not be resolved. This grid dependency poses a problem for the calibration procedures and the correct interpretation of the results. Moreover, the computational cost of simulations is strongly affected by the grid resolution. Although, the computational power of computers increases significantly, modellers still deal with issues concerning the computational cost of their models.

Although hydrodynamic and morphodynamic processes have been studied for a very long time, still, not all processes are fully understood. This makes the implementation even more difficult. This is especially true for morphodynamic processes. First, attempts in quantifying the morphological response were made by Exner [8]. He formulated a relation based on the flow velocity to compute the sediment transport rate. The morphodynamic evolution could be determined using a conservation law, this is the so-called Exner or bed evolution equation. Many more attempts are made in coupling the sediment transport to the flow characteristics. However, the description of sediment motion is difficult, as for practical applications it is still impossible to formulate a momentum equation for each grain or a group of grains [9]. Even when using the easy applicable empirical relations for sediment transport, the computational cost of morphodynamic models is high. This is mainly due to the long simulation periods. A scenario approach would be beneficial, as one can investigate the different outcomes under different conditions. When doing so, a model with a limited computational cost is essential.

Another major issue in morphodynamic modelling is the stability of the bed evolution equation. Due to the lack of a natural damping term in a conservation equation, it is very sensitive to instabilities. This was already investigated in the eighties [10]. We will use the available knowledge on sediment dynamics, to improve the accuracy, the efficiency and the stability of morphodynamic simulations. We therefore present the subgrid based approach for morphodynamic modelling.

1.3. Learning a new dance step by step

Currently, two-dimensional, depth-averaged hydrodynamic models are widely used to compute the long term morphodynamic evolution of coastal and riverine areas. Although flow is in principle a three-dimensional phenomenon, even when simplifying the system, the computational effort remains high. The hydrodynamic part of the computation is a dominant contributor for this and strongly depends on the grid resolution. As the computational cost and the grid resolution are related, one is forced to make a compromise between them, when setting up a model. This implies that in actual applications of hydrodynamic and morphodynamic models, the use of high resolution bathymetry information is limited. By incorporating this high resolution information, we take a step in a new direction to improve the accuracy and efficiency of morphodynamic simulations. We introduce a subgrid based approach to solve the equations for the hydrodynamics, the bed evolution equation and the transport. This new approach allows us to make use of the high resolution

information and to preserve it, for a limited increase in computational cost.

Our first step is to improve the accuracy of hydrodynamic models with low resolution grids. We choose to apply a so-called subgrid based approach. This approach allows the use of high resolution information, such as bathymetry and roughness data in coarse grid simulations. The incorporation of the high resolution information results in a strong increase of the accuracy at a limited computational cost. The opposite is true as well, when coarsening the grid resolution, the loss in accuracy is limited, but the computational cost is significantly reduced. The full hydrodynamic method is thoroughly described in Chapter 2. The hydrodynamic model provides water levels and velocities at coarse resolution.

The bed evolution equation will be solved at high resolution. This is feasible, because compared to the total simulation time, the relative computational cost of the morphodynamic part of a simulation is low. Moreover, the accuracy of the morphodynamic solution improves significantly when using a finer grid resolution. Therefore, we introduce a subgrid based approach for morphodynamics. This means that the hydrodynamic computations are performed using a coarse resolution grid and the bed evolution equation is solved at high resolution.

The different computational grids are coupled by interpolating water levels and velocities from the coarse to the high resolution grid. For the velocity we introduce a physics-based interpolation method. The velocities are interpolated using the continuity and a simplified momentum equations. The high resolution bathymetry and roughness information provide essential input for this interpolation. Based on the interpolated velocity field, bed shear stresses can be computed to determine the sediment transports. In addition, to increase the accuracy of the results, we propose a numerical scheme that naturally enhances the stability of the bed evolution equation. Chapter 3 elaborates on this approach and discusses its advantages and limitations.

Sediment transport is often affected by temporal and spatial lag effects. This implies that an algebraic sediment transport equation is not always sufficient. Especially for finer sediment, the transport equation for suspended sediment, including spatial and temporal lags needs to be applied. To account for suspended sediment, the sediment concentration in the water and the exchange rate between the bed and the water column need to be determined. Therefore, we extended the subgrid based approach for morphodynamic modelling by including suspended sediment and the corresponding lag effects. Moreover, we want to benefit from, and to preserve, the high resolution bathymetry information. Consequently, the exchange rates need to be defined on the high resolution grid, as these are part of the bed evolution equation. However, these exchange rates affect the bed evolution and depend on the sediment concentration in the water column. Yet, the sediment concentration, given by the transport equation for suspended sediment, scales with the hydrodynamic time scale. Therefore, it is advantageous to solve this equation with the same coarse resolution as the hydrodynamic part. In Chapter 4 we describe how the transport equation at coarse resolution is solved and how the exchange rates at high resolution are determined. Thereby, increasing the accuracy of coarse grid simulations of the sediment transport equation and preserving the high resolution

bathymetry information.

There are several other aspects we have been investigating, however, these are not all addressed in full detail. In Chapter 5 we have included two examples to illustrate the wide range of applications for which the subgrid based approach can be used. The first example is a hydrodynamic simulation of the Westerschelde. The large depth range and complex bathymetry makes it a challenging area to model with coarse resolution grids. The second example is a very simplified case of bank erosion. This is a very complex process, that occurs locally, but is affected by, and affects, a large area. A subgrid based approach can be useful in combining the different spatial scales.

The final chapter, Chapter 6 contains a discussion and an overall conclusion. It addresses the advantages and the limitations of the various aspects of the subgrid based approach. Moreover, we elaborate on present day applications of subgrid methods and a possible outlook on future applications and developments.

2

A Finite Volume Approach for Shallow Water Flow Accounting for High Resolution Bathymetry and Roughness Data

This study presents a finite volume hydrodynamic model for shallow water flow, that computes on a coarse grid, but accounts for high resolution bathymetry and roughness variations on a subgrid. The detailed information can be incorporated by using the assumption of a uniform flow direction and a uniform friction slope within a part of a coarse grid cell. It is shown in two examples, that the results of coarse grid simulations become as good as high resolution results, but at much lower computational cost.

This chapter is published as Volp, van Prooijen, and Stelling [11].

2.1. Introduction

There exists a strong interest in fast and accurate hydrodynamic models. They are used for various purposes, like flood forecasting or to form the basis for morphodynamic models. Both types of simulations need fast models for large domains and at high resolution. Flood forecasting models need to be fast, because such models are to provide results at short notice. Morphodynamic simulations need fast hydrodynamic solvers as the duration of a simulation period is generally long. Nowadays, detailed information of the bathymetry is available due to improved measurement techniques, like LIDAR. Bathymetric data with a very high spatial resolution (of the order of magnitude of meters) can be obtained. The discretization for numerical modeling is still a trade-off between accuracy and computation time. The computation time is generally a limiting factor for the use of high resolution bathymetry data. Taking into account the high resolution data on a sub-grid would therefore be a possible trade-off. There are various methods proposed to incorporate high resolution bathymetry data as some kind of sub-grid: Sanders *et al.* [12], Cea and Vázquez-Cendón [13], Bates [14], Yu and Lane [15]. Casulli [16] introduced a *sub-grid*-based hydrodynamic model, accounting for high resolution bathymetry information in coarse grid simulations. It is based on the principle that the bed level can vary strongly over short distances, while water levels vary over larger scales. The subgrid method deals with two grids, a coarse computation grid and an underlying subgrid with a higher resolution. The bed level is defined on the subgrid and the water level is assumed to be uniform within a coarse grid cell. The computation of cell volumes (cell-integrated depth) and cross-sections are performed using the high resolution bathymetry data.

Friction is represented by a non-linear function of a friction coefficient and velocity. Both can vary strongly over short distances, due to variations in roughness and depth. Coarse grid simulations use cell averaged depths and velocities, neglecting effects of variations on smaller scale. This causes an overestimation of the friction, which can be illustrated for a simple steady uniform one-dimensional flow. For such case the discharge can be computed analytically using the Chézy equation. The discharge is $Q = WC_z H^{\frac{3}{2}}\sqrt{i_b}$, with: W width of channel, C_z Chézy coefficient, H total depth, i_b bed slope. When the depth in transverse direction is not uniform, for example when half of the channel has depth H_1 and the other half H_2, the total discharge is given by $Q = \frac{1}{2}WC_z\sqrt{i_b}\left(H_1^{\frac{3}{2}} + H_2^{\frac{3}{2}}\right)$ which is always equal or larger than a discharge based on the average depth: $Q = WC_z\sqrt{i_b}\left(\frac{1}{2}H_1 + \frac{1}{2}H_2\right)^{\frac{3}{2}}$. We elaborate on this in the example of a compound channel in Section 2.3.1. Generally, the friction coefficient is lowered, during the calibration phase, to correct for this underestimation of the conveyance. However, the friction coefficient becomes contaminated with effects of a varying depth and therefore becomes grid size dependent. Already in the 1930's, the effect of a varying velocity field on the friction in one dimensional models was considered by Lorentz *et al.* [17] and Lotter [18].

There are numerous options for the spatial discretization of the flow domain. Structured and unstructured grids have both their advantages and disadvantages. For a structured grid, the discretized equations are relatively simple even for anisotropic

stresses, but the representation of arbitrary and moving boundaries, e.g. due to flooding and drying, is generally a problem. Land-water interfaces vary in type. They can be very sharp, when dealing for example with steep dikes or quays. Then, the interfaces do not move in space due to water level variations. In this case unstructured grids may have an advantage over Cartesian grids. When dealing with tidal flats or river banks with mildly sloping bottoms the land-water interfaces vary in time. In this case, unstructured grids face similar problems as structured grids. Some classical disadvantages of structured grids compared to unstructured grids have been largely removed by proposing flow solvers that deal with moving and arbitrary boundaries, such as cut-cell methods, immersed boundary methods, quad trees, etc. (Aftosmis *et al.* [19]; Ye *et al.* [20]; Causon *et al.* [21]; Mittal and Laccarino [22]; Poretti and De Amicis [23]; Liang and Borthwick [24]). The subgrid method of Casulli [16] offers an elegant algorithm to handle the (moving) boundaries accurately for unstructured grids. This approach combines the advantages of the accurate representation of both sharp and mild land-water interfaces with effectively dealing with the non-linearity of the continuity equation, due to flooding and drying. This method is also effective for structured grids. Here, we use Cartesian grids for simplicity, but the proposed method can also be applied to unstructured grids.

In this paper we present a finite volume method for shallow water flow. We use a subgrid-based formulation for the continuity (similar to Casulli [16]) and combine it with a subgrid-based momentum conservative scheme for the advection and a subgrid-based formulation for bottom friction. The formulation for bottom friction shows similarities with the effective depth defined in Defina [25], and Yu and Lane [26], but in addition to these studies the spatial variation in roughness is considered here.

Section 2.2 describes the model formulation based on the shallow water equations, detailing the incorporation of subgrid information in the coarse grid model. Section 2.3 shows two numerical steady state examples. In the first example, the flow in a compound channel is considered. The effect of varying depth and roughness on the flow is isolated. We emphasize the advantage of using local roughness and depth information. The flow in a U-shaped bend is the second example. It shows that a sufficiently refined subgrid can represent both sharp and mild land/water interfaces with satisfactory accuracy. Moreover, the example shows that the flow can be modeled well for a low resolution of the computational grid. The paper is finalized with conclusions and discussions on the applicability and limitations of the method in Section 2.4.

2.2. Model description

2.2.1. Definition of variables

A subgrid-based, two dimensional, depth-averaged finite volume model for shallow water is introduced. It accounts for bed level and roughness variations on a smaller scale than the dimensions of a computation cell. The subgrid is a small raster of subgrid cells (pixels) with a surface area of $\delta x \times \delta y = \sigma_{i,j}$ and contains all high

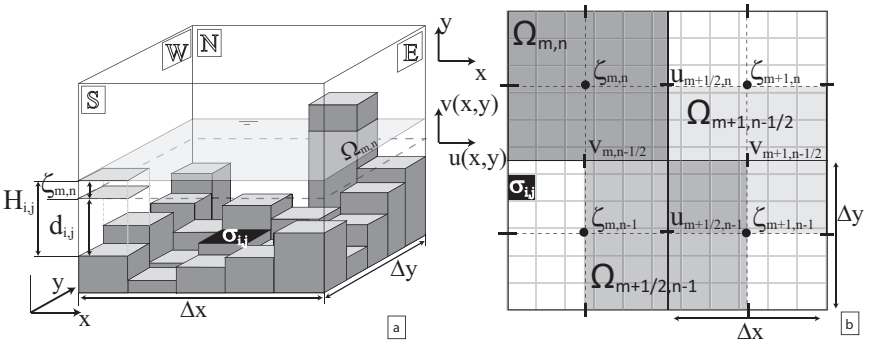

Figure 2.1: a: A schematic view of a computation cell with an underlying subgrid, where a part of the domain is dry. b: An overview of computation cells and domains with water level points in the cell centers and velocity points at the faces.

resolution data. The coarse grid has a low resolution compared to the subgrid and is similar to the computation grid of traditional models. It supports coarse grid variables such as water levels and velocities and the full time integration. In principle, this grid can be of any type, structured or unstructured. For reasons described in the introduction, we chose for a structured, staggered, Cartesian computation grid. Figure 2.1.a shows a single coarse grid cell with a non-uniform bed level which is defined on the subgrid. Water levels are defined in the coarse grid cell centers and velocities at the cell edges. Two types of computation domains are considered. A water level domain has its center at a water level point and is indicated by $\Omega_{m,n}$. A momentum domain has its center at a velocity point in either x- or y-direction, indicated by for instance $\Omega_{m+\frac{1}{2},n}$ and $\Omega_{m,n+\frac{1}{2}}$, respectively (Figure 2.1.b). The subscripts m, n always refer to the location of a coarse grid variable and the subscripts i, j to variables defined on the subgrid. The discrete variables are translated from the subgrid or the coarse grid into integrable functions using a simple step function, which is piecewise discontinuous. This so-called indicator function Υ_D is defined for domain D by:

$$\Upsilon_D(x,y,t) = \begin{cases} 1 & (x,y) \in D \\ 0 & (x,y) \notin D \end{cases} \tag{2.1}$$

The dimensions of domain D can be different for each defined variable and will be specified later. The water level $\zeta(x,y,t)$, at arbitrary location and time, is composed from the coarse grid discrete water levels $\zeta_{m,n}$. Using the indicator function, the water level is defined by:

$$\zeta(x,y,t) = \sum_{m=1}^{M} \sum_{n=1}^{N} \zeta_{m,n} \Upsilon_{\Omega_{m,n}} \tag{2.2}$$

where M and N are the maximum number of coarse grid cells in x- and y-direction, respectively. The size of domain $\Omega_{m,n}$ ranges from zero to the area of a coarse grid cell ($\Delta x \times \Delta y$). The exact size of $\Omega_{m,n}$ depends on the wet domain within the cell, i.e. the water level and the bathymetry. When parts of the $\Omega_{m,n}$ domain fall dry, its

size decreases. The bed level $d(x, y)$, based on bathymetry data, is defined positive in downward direction (Figure 2.1.a) and is defined on subgrid level:

$$d(x,y) = \sum_{i=1}^{I}\sum_{j=1}^{J} d_{i,j}\Upsilon_{P_{i,j}} \tag{2.3}$$

where I and J are the maximum number of subgrid cells in x- and y-direction and $d_{i,j}$ is the discrete bed level and is defined in the center of a pixel. $P_{i,j}$ is a domain corresponding to a wet pixel with surface area $\sigma_{i,j}$. A domain Ω, related to the coarse grid, contains at least one, but usually multiple sub-domains P. Note that the size and number of Ω-domains may vary in time. A wet pixel exists when the following condition applies locally:

$$H(x,y,t) = d(x,y) + \zeta(x,y,t) \geq 0 \tag{2.4}$$

in which H is the water depth. Within a coarse grid cell (domain $\Omega_{m,n}$) the water level is uniform, but the water depth can vary due to the subgrid scale variation of the bathymetry (see Figure 2.1.a).

Similar to equation 2.3 the friction coefficient is defined on subgrid level:

$$c_f(x,y) = \sum_{i=1}^{I}\sum_{j=1}^{J} c_{f:i,j}\Upsilon_{P_{i,j}} \tag{2.5}$$

with $c_{f:i,j}$ the discrete friction coefficient. The friction coefficient can be given by Chézy, Manning or any other friction formulation. The depth averaged velocity vector $\vec{u}$ consists of the components $u(x, y, t)$ and $v(x, y, t)$. The velocity field is defined by the discrete coarse grid velocities ($u_{m+\frac{1}{2},n}$ and $v_{m,n+\frac{1}{2}}$) and the indicator function for domain $D = \Omega_{m+\frac{1}{2},n}$ and $D = \Omega_{m,n+\frac{1}{2}}$:

$$u(x,y,t) = \sum_{m=0}^{M}\sum_{n=0}^{N} u_{m+\frac{1}{2},n}\Upsilon_{\Omega_{m+\frac{1}{2},n}} \quad \text{and} \quad v(x,y,t) = \sum_{m=0}^{M}\sum_{n=0}^{N} v_{m,n+\frac{1}{2}}\Upsilon_{\Omega_{m,n+\frac{1}{2}}} \tag{2.6}$$

For convenience later in this paper the coarse grid cells are divided into four areas: South-West (SW), South-East (SE), North-West (NW) and North-East (NE), Figure 2.2. This division is used for both water level and momentum domains. A similar notation is used to refer to the edges (s) of a cell; North (N), South (S), East (E) and West (W).

2.2.2. Continuity Equation

The continuity equation reads in finite volume formulation:

$$(V_{\Omega_{m,n}})_t = Q^u_{m-\frac{1}{2},n} - Q^u_{m+\frac{1}{2},n} + Q^v_{m,n-\frac{1}{2}} - Q^v_{m,n+\frac{1}{2}} \tag{2.7}$$

where the subscript t indicates a partial derivative with respect to time, and

$$V_{\Omega_{m,n}}(t) = \iint_{\Omega_{m,n}} H(x,y,t)\ \mathrm{d}\Omega, \tag{2.8}$$

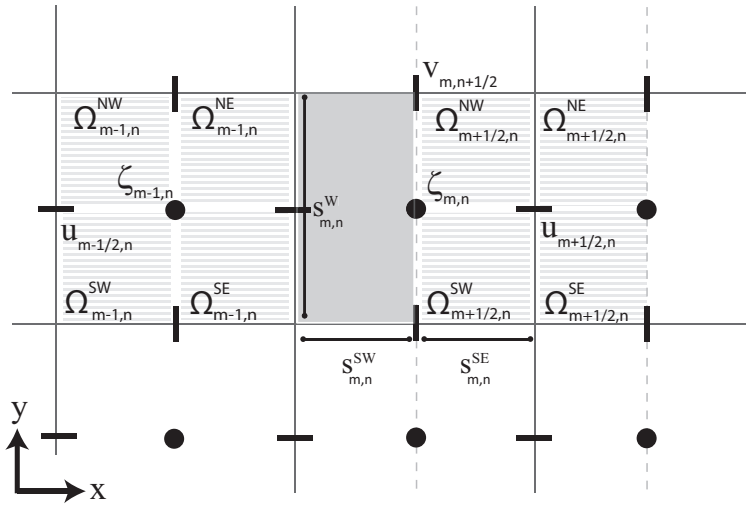

Figure 2.2: A view of the computation grid including indications of velocity, water level points and integration boundaries. Also, the sub-domains of a water level domain (left) and a momentum domain (right) are indicated as well as the control domain (gray area) used to compute the advection.

Q^u and Q^v are the discharges over the four edges of domain $\Omega_{m,n}$ in u- and v-direction. For example, the discharge at the East side of the cell is defined by:

$$Q^u_{m+\frac{1}{2},n} = u_{m+\frac{1}{2},n} A_{s^E_{m,n}} \tag{2.9}$$

$$A_{s^E_{m,n}}(t) = \int_{s^E_{m,n}} H(x,y,t)\ \mathrm{d}y \tag{2.10}$$

where A_s is the cross-sectional area of edge s.

2.2.3. Momentum Equation

Inertia, advection of momentum, pressure force and friction are considered in the momentum balance. This is explained in x-direction only, but is similar in y-direction:

$$(uV)_t + \tilde{F}^x_{adv} + \tilde{F}^x_{pres} + \tilde{F}^x_{fric} = 0 \tag{2.11}$$

where $\tilde{F}$ is a force normalized with the density, which is assumed constant. The spatial discretization for each term is described below.

Bottom Friction

In case of gravity-driven shallow-water flow, friction coefficients are often set relatively small, much smaller than would be expected based on the type of bed surface found in the area of the flow. This to correct an overestimation of the friction, due to the neglected effects of small scale variations in roughness and velocity on the

bottom friction as explained in the introduction. By making an estimate of the velocity field on subgrid-scale, we want to account for these variations. The method described below reduces in a one dimensional setting to the so-called conveyance method. This method is generally used in 1D models for the computation of river flow. Early work on this is done by Lotter [18] and Lorentz *et al.* [17]. Among others, Chow [27] and Cunge *et al.* [28] give an introduction to this concept. Yen [29] gives an overview of the hydraulic resistance in open channels and also treats various formulations for a resistance coefficient when the depth is non-uniform. In this paper, this concept is generalized for a two dimensional setting.

Based on the structure of the staggered grid, it is useful to divide the momentum domain in four quarters. First, the friction in a quarter of a cell is derived. The total friction is the sum of the friction of these quarters. The quarter-domain $\Omega^{NE}_{m,n}$ is taken as an example. The friction is then defined by:

$$\tilde{F}^x_{fric:\Omega^{NE}_{m,n}} = \iint\limits_{\Omega^{NE}_{m,n}} c_f |U_p| u_p \, \mathrm{d}\Omega \qquad \text{with} \qquad |U_p| = \sqrt{u_p^2 + v_p^2} \tag{2.12}$$

where c_f is the dimensionless friction coefficient as defined in equation 2.5 and u_p and v_p are the high resolution, depth-averaged velocities in x- and y-direction. These are defined by:

$$u_p(x,y,t) = \sum_{i=1}^{I}\sum_{j=1}^{J} u_{p:i,j} \Upsilon_{p_{i,j}} \quad \text{and} \quad v_p(x,y,t) = \sum_{i=1}^{I}\sum_{j=1}^{J} v_{p:i,j} \Upsilon_{p_{i,j}} \tag{2.13}$$

where $u_{p:i,j}$ and $v_{p:i,j}$ are the discrete, subgrid velocity components, defined in the center of a pixel. This high resolution velocity field is constructed in order to account for varying roughness and depth within a momentum domain. However, on subgrid level the spatial variation of the velocity is unknown . A relation between the subgrid velocity field and the coarse grid velocity field needs to be determined. The first step is to assume a uniform flow direction within a quarter of a momentum domain. This excludes the internal circulations, convergence and divergence of the flow within this domain. The subgrid velocity is then a linear function of the coarse grid velocity with a dimensionless factor α_p:

$$u_p = \frac{u}{\alpha_p} \quad \text{and} \quad v_p = \frac{v}{\alpha_p} \qquad \text{for} \quad (x,y) \in \Omega_{m+\frac{1}{2},n} \cap \Omega^{NE}_{m,n} \tag{2.14}$$

The friction in domain $\Omega^{NE}_{m,n}$ can be rewritten to:

$$\tilde{F}^x_{fric_{\Omega^{NE}_{m,n}}} = u_{m+\frac{1}{2},n} |U^{NE}_{m,n}| \iint\limits_{\Omega^{NE}_{m,n}} \frac{c_f}{\alpha_p^2} \, d\Omega \qquad \text{for} \qquad (x,y) \in \Omega_{m+\frac{1}{2},n} \cap \Omega^{NE}_{m,n} \tag{2.15}$$

$$\text{with} \qquad |U^{NE}_{m,n}| = \sqrt{u^2_{m+\frac{1}{2},n} + v^2_{m,n+\frac{1}{2}}}$$

Note that the absolute velocity is different for each quarter domain (equation 2.16). Especially when parts of the domain are dry, the flow is now not affected by artificial

frictional effect of inactive parts in other quarters. Finding a definition for α_p results in a modified friction coefficient, that accounts for variations in velocity due to depth and roughness variations within a momentum domain. After assuming a uniform flow direction, the derivation of α_p is performed in streamwise direction. For simplicity, the derivation of the formulation for α_p is shown for a one-dimensional flow in positive direction. The definition of α_p is however independent of the flow direction, as will become clear from equation 2.18. The coarse grid velocity within domain $\Omega^{NE}_{m,n}$ is defined as the volume average of the local subgrid velocities:

$$u = \frac{1}{V_{\Omega^{NE}_{m,n}}} \iint\limits_{\Omega^{NE}_{m,n}} H u_p \mathrm{d}\Omega \quad \text{for} \quad (x,y) \in \Omega_{m+\frac{1}{2},n} \cap \Omega^{NE}_{m,n} \tag{2.16}$$

The main assumption for defining α_p is assuming a uniform friction slope within domain $\Omega^{NE}_{m,n}$. The friction slope is the ratio between the water level gradient and the friction term, for positive flow in x-direction:

$$S = \frac{c_f u_p^2}{gH} = \text{uniform} \quad \text{for} \quad (x,y) \in \Omega_{m+\frac{1}{2},n} \cap \Omega^{NE}_{m,n} \tag{2.17}$$

The friction slope equals the water level gradient and bed slope in case of steady uniform flow. Parameter α_p can now be determined by substituting equation 2.16 into equation 2.14 and by writing u_p in terms of the friction slope:

$$\begin{aligned} \alpha_p = \frac{u}{u_p} &= \frac{\frac{1}{V_{\Omega^{NE}_{m,n}}} \iint\limits_{\Omega^{NE}_{m,n}} H u_p \,\mathrm{d}\Omega}{u_p} = \frac{\iint H \sqrt{\frac{SgH}{c_f}} \,\mathrm{d}\Omega}{\sqrt{\frac{SgH}{c_f}} V_{\Omega^{NE}_{m,n}}} \\ &= \sqrt{\frac{c_f}{H}} \frac{1}{V_{\Omega^{NE}_{m,n}}} \iint\limits_{\Omega^{NE}_{m,n}} H \sqrt{H/c_f} \,\mathrm{d}\Omega \end{aligned} \tag{2.18}$$

α_p relates the subgrid and the coarse grid velocity field. Note that S can be brought outside the integral, as it is assumed uniform within the considered domain. The friction for domain $\Omega^{NE}_{m,n}$ becomes, after substituting α_p into equation 2.15:

$$\tilde{F}^x_{fric_{\Omega^{NE}_{m,n}}} = u_{m+\frac{1}{2},n} |U^{NE}_{m,n}| \frac{V^3_{\Omega^{NE}_{m,n}}}{\left[\iint_{\Omega^{NE}_{m,n}} H\sqrt{H/c_f}\, d\Omega\right]^2} = \frac{u_{m+\frac{1}{2},n} |U^{NE}_{m,n}| V_{\Omega^{NE}_{m,n}}}{H_{f_{\Omega^{NE}_{m,n}}}} \tag{2.19}$$

$$\text{using} \qquad H_{f_{\Omega^{NE}_{m,n}}} = \left[\frac{\iint_{\Omega^{NE}_{m,n}} H\sqrt{H/c_f} \,\mathrm{d}\Omega}{V_{\Omega^{NE}_{m,n}}}\right]^2 \tag{2.20}$$

where H_f is introduced as the 'friction depth'. This friction depth is independent of the direction of the flow and can be interpreted as a weighed friction coefficient. It only depends on the subgrid depths and roughness coefficients within the considered domain. The friction depth is comparable to the 'effective depth' described by for

example Defina [25] or Yu and Lane [26]. However, the friction depth takes variations in depth as well as variations in roughness into account. It also accounts for dry areas within this domain. In the limit of one subgrid cell in a coarse grid cell, the friction depth reduces to $H_f = \frac{H}{c_f}$.

A momentum domain is covered by four sub-domains ($\Omega^{ll}_{m+\frac{1}{2},n}$ with $ll = [NE, NW, SE, SW]$) each with their local contribution to the friction (equation 2.19). The total friction of a u-momentum domain becomes:

$$\begin{aligned}\tilde{F}^x_{fric,\,\Omega_{m+\frac{1}{2},n}} &= u_{m+\frac{1}{2},n}\left(\frac{|U^{NE}_{m,n}|V_{\Omega^{NE}_{m,n}}}{H_{f_{\Omega^{NE}_{m,n}}}} + \frac{|U^{SE}_{m,n}|V_{\Omega^{SE}_{m,n}}}{H_{f_{\Omega^{SE}_{m,n}}}} + \dots\right.\\ &\left. \dots + \frac{|U^{NW}_{m+1,n}|V_{\Omega^{NW}_{m+1,n}}}{H_{f_{\Omega^{NW}_{m+1,n}}}} + \frac{|U^{SW}_{m+1,n}|V_{\Omega^{SW}_{m+1,n}}}{H_{f_{\Omega^{SW}_{m+1,n}}}}\right) \qquad (2.21)\\ &= u_{m+\frac{1}{2},n}\sum_{ll=1}^{4}\frac{|U^{ll}|V_{\Omega^{ll}_{m+\frac{1}{2},n}}}{H_{f_{\Omega^{ll}}}} \quad \text{within} \quad \Omega = \Omega_{m+\frac{1}{2},n} \qquad (2.22)\end{aligned}$$

In this way, the effect of small scale velocity variations on the friction is considered by accounting for high resolution bathymetry and roughness data.

Pressure Force

The third term of equation 2.11 is the pressure force. Assuming a hydrostatic pressure gives:

$$\begin{aligned}\tilde{F}^x_{pres\,\Omega_{m+\frac{1}{2},n}} &= \iint_{\Omega_{m+\frac{1}{2},n}} H\frac{d\mathbb{P}}{dx}\,d\Omega = \iint_{\Omega_{m+\frac{1}{2},n}} gH\frac{\zeta_{m+1,n}-\zeta_{m,n}}{\Delta x}\,d\Omega\\ &= g\frac{V_{\Omega_{m+\frac{1}{2},n}}}{\Delta x}\left(\zeta_{m+1,n}-\zeta_{m,n}\right) \qquad (2.23)\end{aligned}$$

where the pressure gradient is assumed to be uniform within a domain $\Omega_{m+\frac{1}{2},n}$.

Inertia and Advection of Momentum

Inertia and advection are given by the first two terms of equation (2.11). Rewriting these gives:

$$(uV)_t + \tilde{F}^x_{adv} = u_tV + uV_t + \bar{u}_{s^E}\bar{Q}^u_{s^E} - \bar{u}_{s^W}\bar{Q}^u_{s^W} + \bar{u}_{s^N}\bar{Q}^v_{s^N} - \bar{u}_{s^S}\bar{Q}^v_{s^S} \qquad (2.24)$$

for $(x, y) \in \Omega_{m+\frac{1}{2},n}$. Variables with an over bar, such as $\bar{u}$, indicate a value that is missing at the specific grid location. Subscript s refers to the variable at an edge of the domain $\Omega_{m+\frac{1}{2},n}$, see Figure 2.2. The last four terms represent the momentum fluxes in and out of domain $\Omega_{m+\frac{1}{2},n}$. Here, a momentum conservative scheme for advection is derived, based on Stelling and Duinmeijer [30], Kramer and Stelling [31] and Kernkamp *et al.* [32]. The missing velocity values are computed by a first order up-wind scheme. Then, only the discharges $\bar{Q}_s$ at the faces of the

momentum volume are missing. These are the discharges corresponding to multiple velocity points ($\bar{Q}^v_{s^S}$,$\bar{Q}^v_{s^N}$) and those located at a water level point ($\bar{Q}^u_{s^E}$,$\bar{Q}^u_{s^W}$). When substituting the continuity equation into equation 2.24 -and for simplicity of notation assuming positive flow direction- it can be rewritten as:

$$u_t V + \bar{Q}^u_{s^W}\left(u_{m+\frac{1}{2},n} - u_{m-\frac{1}{2},n}\right) + \bar{Q}^v_{s^S}\left(u_{m+\frac{1}{2},n} - u_{m+\frac{1}{2},n-1}\right) \tag{2.25}$$

for $(x,y) \in \Omega_{m+\frac{1}{2},n}$. The discharge over a whole face of a water level domain is known based on continuity (equation 2.9). However, the distribution of the discharge over a cell face is unknown and can be chosen. A distribution of the discharge over the face based on friction and water depth is used. The unknown discharges ($\bar{Q}^u_{s^W}$ and $\bar{Q}^v_{s^S}$) are based on the discharges at the faces of the sub-domains $\Omega^{ll}_{m,n}$ of a water level domain ($ll = SW, NW, NE, SE$, Figure 2.2). First, we compute $\bar{Q}^v_{s^S}$ and subsequently $\bar{Q}^u_{s^W}$. This results in the full advection and inertia terms.

In order to find the distribution of the discharge over a face, a subgrid velocity field is constructed. The procedure is similar to the one used for the formulation of the friction term. The construction of the subgrid velocity at face $s^S_{m,n}$ (the face of a water level domain) is used as example. To guarantee continuity, the subgrid velocity field is directly related to the discharge at the face:

$$Q^v_s = v_{m,n-\frac{1}{2}} \int_s H\ dx = v_{m,n-\frac{1}{2}} A_s = \int_s v_p H\ dx \quad \text{with} \quad (x,y) \in s = s^S_{m,n}$$

Similar to equation 2.14, the subgrid velocity is a linear function of the coarse grid velocity, using the dimensionless factor (γ_p):

$$v_{m,n-\frac{1}{2}} = \gamma_p v_p(x,y) \quad \text{with} \quad (x,y) \in s = s^S_{m,n}$$

The discharge over face $s^S_{m,n}$ is then defined by:

$$\begin{aligned} Q^v_{s^S_{m,n}} = Q^v_{s^{SW}_{m,n}} + Q^v_{s^{SE}_{m,n}} &= \int_{s^{SW}_{m,n}} v_p H dx + \int_{s^{SE}_{m,n}} v_p H dx \\ &= v_{m,n-\frac{1}{2}} \left(\int_{s^{SW}_{m,n}} \frac{H}{\gamma_p} dx + \int_{s^{SE}_{m,n}} \frac{H}{\gamma_p} dx \right) \end{aligned} \tag{2.26}$$

Similar to Equation 2.17, γ_p is determined by assuming a uniform friction slope (equation 2.17). Parameter γ_p and the corresponding friction depth (H_f) are defined in a similar way as for the derivation of α_p:

$$\gamma_p = \sqrt{\frac{c_f}{H}} \frac{\int_{s^{SE,SW}_{m,n}} H\sqrt{H/c_f}\, dx}{A_{s^{SE,SW}_{m,n}}} \tag{2.27}$$

$$H_{f_{s^{SE,SW}_{m,n}}} = \left[\frac{\int_{s^{SE,SW}_{m,n}} H\sqrt{H/c_f}\, dx}{A_{s^{SE,SW}_{m,n}}} \right]^2 \tag{2.28}$$

Considering equation 2.26 and the definition of the friction depth above, the discharge over a sub-face ($s^{SE}_{m,n}$) is:

$$Q^v_{s^{SE}_{m,n}} = v_{m,n-\frac{1}{2}} \frac{\int_{s^{SE}_{m,n}} H\sqrt{c_f/H}\,dx}{\sqrt{H_{f_{s^S_{m,n}}}}} \tag{2.29}$$

The discharges at other sub-faces can be found in a similar way. The discharge $\bar{Q}^v_{s^S_{m+\frac{1}{2},n}}$ is the sum of the discharges over the two sub-faces:

$$\bar{Q}^v_{s^S} = Q^v_{s^{SE}_{m,n-\frac{1}{2}}} + Q^v_{s^{SW}_{m+1,n-\frac{1}{2}}} \tag{2.30}$$

Discharge $\bar{Q}^u_{s_{m,n}}$, i.e. the discharge through the cell center of a water level domain, is determined by using continuity and the discharge of the sub-faces. First, a control volume is composed using the sub-domains $\Omega^{NE}_{m,n}$ and $\Omega^{SE}_{m,n}$ (gray area in Figure 2.2). Continuity in this domain implies:

$$(V_{\Omega^{NW,SW}_{m,n}})_t = Q^u_{m-\frac{1}{2},n} - \bar{Q}^u_{s_{m,n}} + \bar{Q}^v_{s^{SE}_{m,n}} - \bar{Q}^v_{s^{NW}_{m,n}} \tag{2.31}$$

The first and second term are already known, as these are based on values of the previous and the current time step. The two latter terms are determined with the aforementioned method. The discharge at the cell center ($\bar{Q}^u_{s_{m,n}}$) follows directly.

The inertia and advective terms from equation 2.24 are now defined (for positive flow direction) by using equations 2.26 and 2.31 by:

$$\begin{aligned} u_t V + \bar{Q}^u_{s^W}\left(u_{m+\frac{1}{2},n} - u_{m-\frac{1}{2},n}\right) + \bar{Q}^v_{s^S}\left(u_{m+\frac{1}{2},n} - u_{m+\frac{1}{2},n-1}\right) &= u_t V + adv(u) \\ adv(u_{m+\frac{1}{2},n}) &= \left(u_{m+\frac{1}{2},n} - u_{m-\frac{1}{2},n}\right)\bar{Q}^u_{s_{m,n}} + \dots \\ \dots + \left(u_{m+\frac{1}{2},n} - u_{m-\frac{1}{2},n-1}\right)&\left(\bar{Q}^v_{s^{SE}_{m,n}} + \bar{Q}^v_{s^{SW}_{m+1,n}}\right) \end{aligned} \tag{2.32}$$

for $(x, y) \in \Omega_{m+\frac{1}{2},n}$. This formulation is momentum conservative and accounts for subgrid scale variations in roughness and depth, including flooding and drying.

Time integration

In the previous sections, subgrid effects are considered in the evaluation of the momentum and continuity equations. The time integration is semi-implicit for the friction term and fully explicit for the advection. The time step is therefore limited by the CFL condition based on velocity. This could be avoided by applying a locally implicit method (Kramer and Stelling [31]). The so-called θ- method is used for the time integration of the advection and gravity term. The time discretization for the

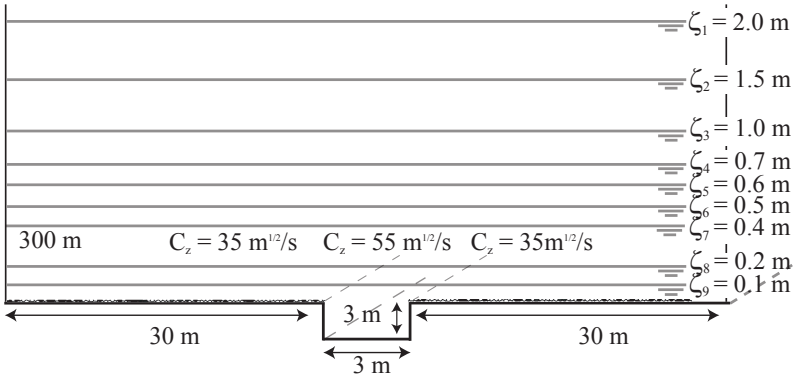

Figure 2.3: A schematic representation of the compound channel, the flood plaines are covered by vegetation, represented by a lower Chézy coefficient. Also the 9 different water levels, which serve as boundary conditions for the various simulations are indicated.

continuity and momentum equations results in:

$$\begin{aligned} \frac{V^{k+1}_{m,n} - V^{k}_{m,n}}{\Delta t} &+ u^{k+\theta}_{m+\frac{1}{2},n} A^{k}_{s^{E}_{m,n}} - u^{k+\theta}_{m-\frac{1}{2},n} A^{k}_{s^{W}_{m,n}} + \dots \\ \dots &+ v^{k+\theta}_{m,n+\frac{1}{2}} A^{k}_{s^{N}_{m,n}} - v^{k+\theta}_{m,n-\frac{1}{2}} A^{k}_{s^{S}_{m,n}} = 0 \end{aligned} \tag{2.33}$$

$$\begin{aligned} \frac{u^{k+1}_{m+\frac{1}{2},n} - u^{k}_{m+\frac{1}{2},n}}{\Delta t} &+ \frac{adv(u^{k}_{m+\frac{1}{2},n})}{V^{k}_{\Omega_{m+\frac{1}{2},n}}} + g\frac{\zeta^{k+\theta}_{m+1,n} - \zeta^{k+\theta}_{m,n}}{\Delta x} + \dots \\ \dots &+ \frac{u^{k+1}_{m+\frac{1}{2},n}}{V^{k}_{\Omega_{m+\frac{1}{2},n}}} \sum_{ii}^{4} \frac{|U^{ii}_{m+\frac{1}{2},n}|^{k} V^{k}_{m+\frac{1}{2},n}}{H^{k}_{f_{\Omega^{ii}_{m+\frac{1}{2},n}}}} = 0 \end{aligned} \tag{2.34}$$

The variables at k+θ are defined by:

$$f^{k+\theta} = (1-\theta) f^{k} + \theta f^{k+1}$$

In the examples we use $\theta = 1$ as steady state solutions are considered. In a subgrid based model the volume of a cell is not necessarily a linear function of the water level, as the (wet) cell surface area is a function of the water level as well. An iterative method is needed to solve the system of equations 4.9. Casulli [16] describes how such a weakly non-linear system can be solved by means of a Newton iteration. He gives a rigorous proof of the convergence of this method for a sparse system of non-linear equations. This method is adopted here as well.

2.3. Examples

2.3.1. Compound Channel

A compound channel is defined as a channel with a non-uniform cross-section. Examples of such systems are rivers with a main channel and flood plains or salt

marshes with channels cutting through (Fagherazzi and Furbish [33]). Especially, the channels on intertidal flats and in salt marshes are relatively small scale features compared to the size of an estuary. In order to control the computational cost, small scale bathymetric variations are often not represented well in models covering a large domain. Cross-sections and storage capacity are therefore often underestimated.

In this example, a straight compound channel is considered, emphasizing the effect of a spatially non-uniform friction, due to variations in depth and roughness. We focus on the conveyance of the system. This example is chosen to show the effect of the non-linearity of the friction term, as was described in the introduction. The dimensions of the compound channel are based on marshes found in the eastern part of the Western Scheldt, at the *Verdronken land van Saeftinghe*. The bathymetry is defined on a subgrid with pixel sizes of 1 m by 1 m. The computational domain is 63 m wide and 300 m long. The narrow channel is 3 m wide and the bed level is 3 m below the bed level of the flats. The intertidal flats are 30 m wide (Figure 2.3) and have a higher roughness due to, for example vegetation. This higher roughness is represented by lower values of the Chézy coefficient. Other formulations for the friction or drag force can be used. Water levels are imposed at the boundaries, forcing the water level gradient equal to the bed slope of 10^{-4}. Nine different water levels are imposed to show the depth dependency. All water levels are within the expected tidal range, Figure 2.3. In its steady state, the flow is (almost) uniform in streamwise direction. Differences in results are therefore caused by the formulation of the friction term.

Table 2.1: An overview of the three different models performed for the compound channel.

	Model A	Model B	Model C
Computation cell	1 m. x 1 m.	60 m. x 63 m	60 m. x 63 m
Use of subgrid	No	Continuity equation	Full set of equations
Computational cost	100 %	0.01 %	0.02 %

Three model types are applied to determine the influence of the non-linear interaction between friction coefficient, velocity and depth. Table 2.1 gives an overview of the settings of the three models. Model A is the high resolution reference run: the computation grid is equal to the high resolution subgrid. The results of the two other models are compared to the results of this model. The results of the coarser models (B and C) can in principle not be better than the result of the high resolution model. The presented method only makes an estimation of the flow on scales smaller than a coarse grid cell and thus neglects all processes except for friction on that scale. Model A uses the classic formulation for the continuity and momentum equations, as there is no underlying subgrid. Model B is a coarse grid model, that uses a subgrid-based formulation for the continuity equation only. Cross-sections

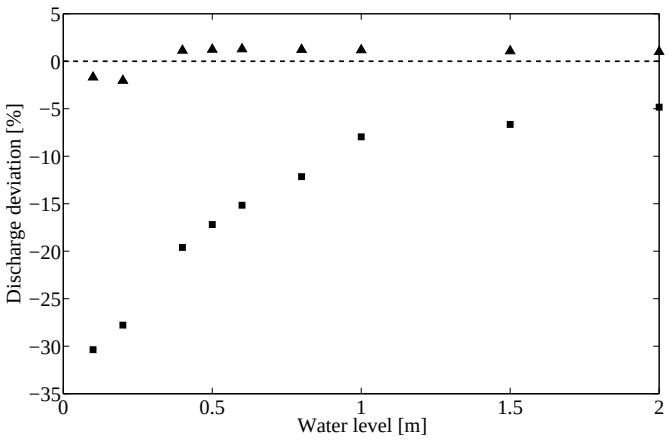

Figure 2.4: Discharge results for the compound channel example. The relative deviation of the discharge compared to the reference runs (Model A) are plotted for all water levels (Discharge deviation= $\frac{Q_B - Q_A}{Q_A}.100$). Results from Model B, subgrid-based continuity equation, are indicated by squares and those of Model C, subgrid-based finite volume approach, with triangles.

and cell volumes are subgrid-based computations, while average values for the velocity and roughness are used in the friction term (the classic approach). Model C uses the full subgrid-based finite volume method, as described in the previous section. Model B and Model C use a computation grid with only one cell in transverse direction, the computation cell size is 60 m x 63 m. As these two models have only one cell in transverse direction, effectively the flow is simulated in one dimension. Model A simulates the flow in two dimensions, including transverse interactions.

The relative deviation in conveyance (discharge) is shown for the 9 different water levels in Figure 2.4. Model B under predicts the conveyance, especially for low water levels. For these low water levels, the difference in depth between the channel and the flat is relatively large. A uniform bed friction is then a poor representation. The relative difference in depth decreases for higher water levels. A uniform bed friction becomes a more reasonable estimate. The under prediction of the conveyance can be corrected by choosing a lower friction coefficient (c_f). Unfortunately, the correction depends on the grid size and on the water level as shown in Figure 2.4. This makes a consistent calibration for c_f difficult. The results of Model C are very close to the results of Model A. For all water levels the deviation is less than 1%. The high resolution simulations of Model A show a small decrease in water level in the center of the channel. This is due to the dynamic pressure (Bernoulli's Principle), which generates a small exchange of momentum between the channel and the flats. This is not observed in the coarse grid simulations, as they have only one cell in cross-flow direction. This explains the small deviations found between Model C and Model A. We conclude that the computational cost for Model B and Model C are only a fraction of the time needed to compute the simulation with high resolution (Model A), as follows from the last row in Table 2.1. This saving in computation time is a

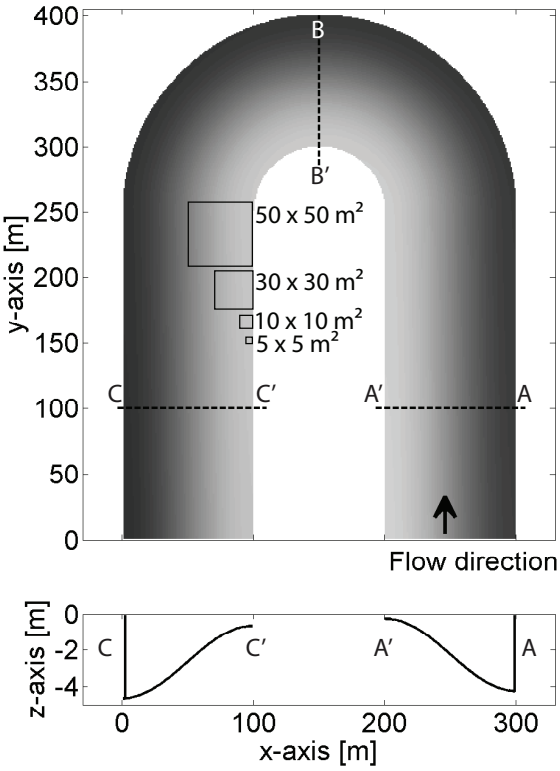

Figure 2.5: The bathymetry of the U-bend with a deep outer bend and a shallow inner bend. Transects AA', BB' and CC' are used for presenting several results.

consequence of the strong reduction in the number of computation cells. Despite the coarse resolution of the coarse grid, the results for the subgrid-based finite volume method (Model C) are accurate and the error shows no dependence on depth.

2.3.2. U-Bend

In the second example, the flow in a U-shaped bend is considered in two dimensions. A depth-averaged simulation is performed, neglecting three-dimensional flow features. We aim to show that the model is capable of simulating flow in a complex geometry with advection effects, similar to cut cell methods (Rosatti *et al.* [34]). Figure 2.5 shows a channel with a deep outer bend, a shallow inner bend and an overall bed slope of $5.0\,10^{-4}$ in flow direction. The inner radius of the bend is 50 m and the channel width is 100 m. In the lower panel of Figure 2.5, the cross-section of the bed level is plotted at the transects AA' and CC' showing a mild slope in transverse direction. The high resolution bathymetry is described on 1 x 1 m^2-sized pixels. The location of the land-water interface at the outer bend is fixed as it is defined as a vertical wall. The location of the land-water boundary at the inner bend depends on the water level and therefore on the discharge. For a cut-cell method

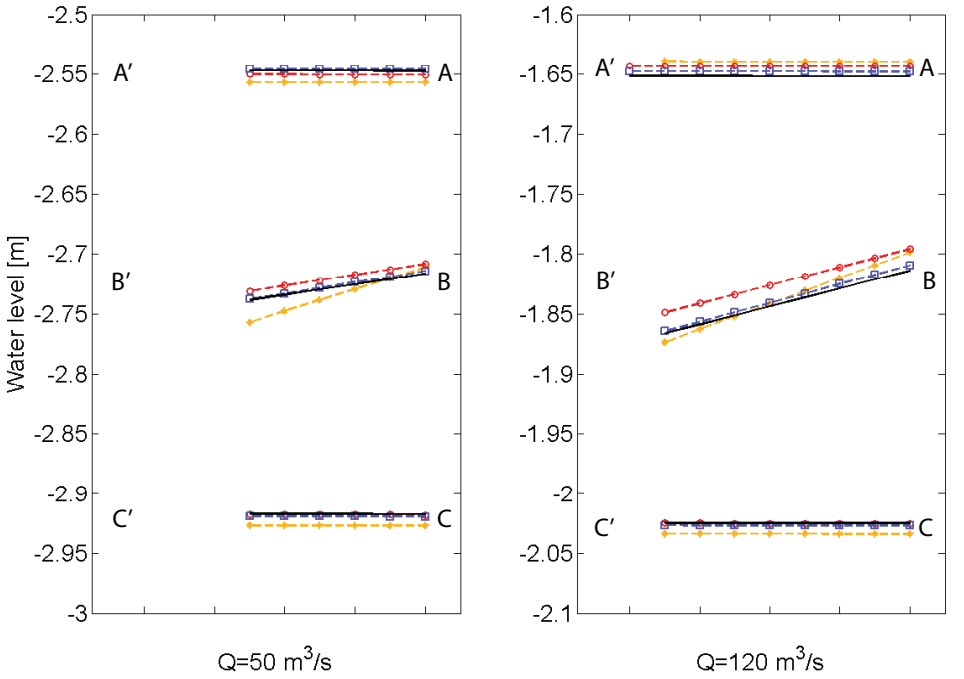

Figure 2.6: Water level results over three transects for discharges $Q = 50, 120$ m^3/s, based on simulations with subgrid and computation cells with size 5x5 m^2 (green), 10x10 m^2 (blue), 30x30 m^2 (red), 50x50 m^2 (yellow).

it is difficult to locate this inner boundary. The boundary is automatically set in this subgrid-based model, because (parts of) coarse grid cells are allowed to be dry. A constant discharge is imposed at the inflow boundary condition. At the outflow a Neumann boundary is used, imposing the water level gradient equal to the bed slope. These boundary conditions allow the flow to choose its own flow domain within the prescribed bathymetry.

A stationary solution is determined for six different discharges ($Q = 30, 50, 80, 100, 120, 300$ m^3/s). Four different computation grids with cell sizes of 5 x 5, 10 x 10, 30 x 30, 50 x 50 m^2 are used. Each simulation is run with and without using the full subgrid method.

The transects AA', BB' and CC' in Figure 2.5 are defined from the outer bend to the inner bend. Water levels along these transects are plotted in Figure 2.6 for simulations with subgrid for all different grid-sizes. For clarity, only the results of simulations forced with two different discharges are presented. The results for the four cell sizes are plotted with a different color and marking. The results show a minimum grid size dependency, especially those from the simulations based on the 5 x 5 m^2 (black line) and 10 x 10 m^2 (blue, squares) sized grids are almost equal. The error increases slightly for the larger grids (30 x 30 m^2 (red, open circles) and 50 x 50 m^2 (yellow, closed circles)). A transverse water level gradient

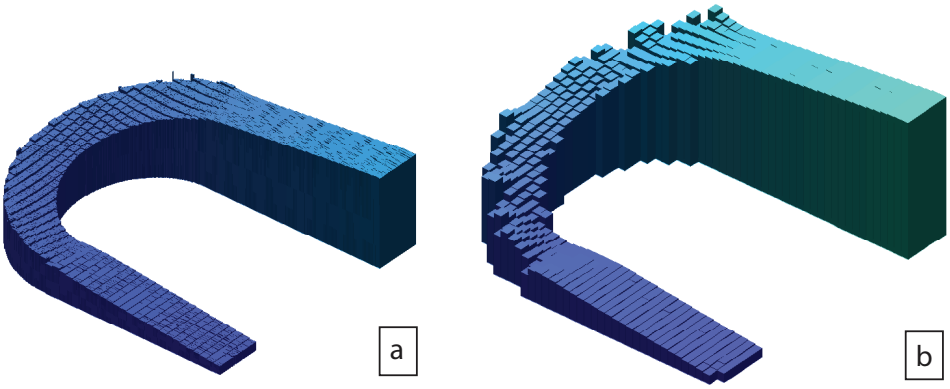

Figure 2.7: The minimum water level is subtracted from the local water level, this visualizes the increase of water level (set-up) in the channel. a) The first plot is a subgrid-based simulation with a cell size of 10x10 m^2 and a discharge of 100 m^3/s. b) The second is the counter plot without subgrid.

is found in cross-section BB' to create the required centrifugal force. The length of the transects is a measure of the wet domain. This transect increases for higher discharges and is consistent for the various grid sizes. The largest grid sizes are in the same order of magnitude as the width of the flow. Only one to three cells cover the flow in transverse direction when the channel is not completely submerged. Some flow characteristics can then not be captured anymore. The assumption of a uniform flow direction in a coarse grid cell is partly violated. However, the results of the larger grids for the higher discharge (right panel of Figure 2.6) are still in fairly good agreement.

Simulations for various grids and discharges are also performed without using subgrid. The water level results show much larger variations between the grids and only for the two smallest grid sizes, a reasonable result is obtained. Overall, the water level slope in streamwise direction is much larger than the water level slopes found for the subgrid-based simulations. This artificial friction is caused by the discretization, Figure 2.7. Note that in this figure the minimum water level in the channel is subtracted from the local water level, showing the relative set-up only. The difference between the simulations with and without subgrid is over 40% for the first case (cell size is 10x10 m^2 and $Q = 100$ m^3/s). The set-up in water level increases for larger discharges and larger cells, up to 65% (cell size is 30x30 m^2 and $Q = 300$ m^3/s) compared to the higher resolution simulations.

Obviously, the velocity field is less detailed and more patchy when using a low resolution computation grid. From the streamlines in Figure 2.8 we can however conclude that the bulk flow is modeled correctly with the subgrid model. Various streamlines are drawn starting at two different locations using a linear interpolation method within a momentum volume. Results are shown for simulations using a grid size of 5x5 m^2 (black), 10x10 m^2 (red), 30x30 m^2 (green), Q=100 m^3/s. Although the overall trajectory of the streamlines from the coarse simulations is correct, it is

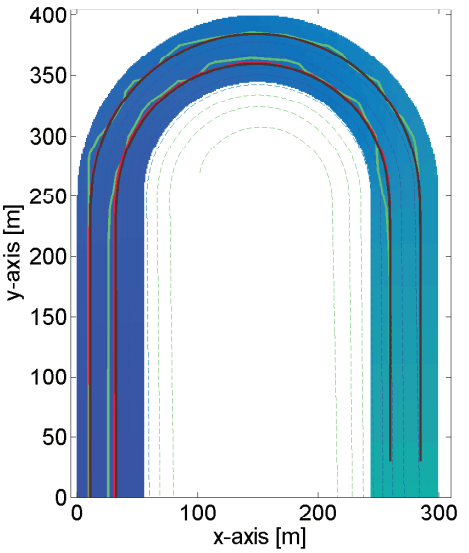

Figure 2.8: Two sets of three streamlines are drawn for a discharge of 100 m^3/s, based on 5x5 m^2 (red), 10x10 m^2 (black) and 30x30 m^2 (green). The background is the water level and the dashed lines are the depth contours of the full prescribed bathymetry, to indicate the dry area as well.

clear that a linear interpolation is used. Especially in the bend, the trajectory of the simulation with the coarsest grid shows deviations that follow from the interpolation.

The computational cost of these simulations with and without subgrid is a only few percent of the cost of the high resolution simulations. The percentages are similar to the ones found in the previous example. The reduction in computation time is mainly due to the strong reduction in computation cells. With this example of a U-bend, it is shown that the model is capable of representing the correct conveyance of a flow in a complex geometry with advection effects.

2.4. Discussion and conclusion

We presented a two dimensional, finite volume approach for shallow water flow that accounts for high resolution bathymetry and roughness data. High resolution effects are considered in coarse grid computations via a subgrid in both the continuity and the momentum equations. We aimed at increasing the accuracy of two dimensional, depth-averaged coarse grid models without a substantial increase in computation time.

To account for the small scale effects of bathymetry and roughness in formulating the friction and advection terms, a high resolution velocity field is constructed. The construction is based on two main assumptions. First, we assumed that the flow within a quarter of a cell has a uniform direction and that it scales linearly with the coarse grid velocity. Internal circulations, convergence and divergence of the flow are thereby excluded within that domain. Variations in magnitude of velocity on small

scale are however allowed. This assumption of a uniform flow direction within a cell is made in traditional models as well, but small scale variations of the magnitude of the velocity field are then excluded too. Second, a uniform friction slope is assumed for the construction of the high resolution velocity field. This assumption is especially preferred over a uniform velocity for flows in areas with a large variation in bathymetry and/or roughness. In flow domains where the variation in bathymetry and roughness is small or in domains where the friction is not the dominant process, the assumption of a uniform friction slope is as good as the assumption of a uniform velocity. In summary, the method gives significant improvement of the results in shallow flows with small scale depth and roughness variations and has no negative effects in other cases.

In theory, the size of the subgrid can be as small as available. The limitations should however be kept in mind. The model is based on the depth-averaged shallow water equations. This implies that the flow around three-dimensional roughness elements is not resolved and has to be modeled within the friction coefficient. The minimum size of the subgrid should at least be several times the size of the roughness elements. For example LIDAR data can have resolutions much smaller than this typical size. It is still a challenge to transform these small scale features in a roughness coefficient. The size of the coarse grid of the new model is mainly limited by the assumption of a uniform flow direction. If small scale flow directions have to be resolved, a small coarse grid is required. This limitation is less strict than the limitation of the grid size for traditional models. There, the horizontal scale of the variation in bathymetry and roughness determines the size of the grid cell. This is generally smaller than the size of the circulations or significant deviations in flow direction of interest. The grid size of a coarse grid in a subgrid model simulation can therefore be larger than the grid size of a traditional model without loss of accuracy. This results in a strong decrease in computational time.

The presented model offers an improvement of traditional coarse grid models and captures moving boundaries automatically without any preprocessing. The size of the computational grid is now determined by the spatial scales of the flow direction and much less on the spatial scales of bathymetry and roughness variations. The final result is a strong reduction in computational time, without loss of accuracy.

Acknowledgement
The work presented in this paper is carried out as part of the innovation programs Building with Nature and Knowledge for Climate. The Building with Nature program is funded from several sources, including the Subsidieregeling Innovatieketen Water (SIW, Staatscourant nrs 953 and 17009) sponsored by the Dutch Ministry of Transport, Public Works and Water Management and partner contributions of the participants to the Foundation EcoShape. The program receives co-funding from the European Fund for Regional Development EFRO and the Municipality of Dordrecht.

3

A Subgrid Based Approach for Morphodynamic Modelling

To improve the accuracy and the efficiency of morphodynamic simulations, we present a subgrid based approach for a morphodynamic model. This approach is well suited for areas characterized by sub-critical flow, like in estuaries, coastal areas and in low land rivers. This new method uses a different grid resolution to compute the hydrodynamics and the morphodynamics. The hydrodynamic computations are carried out with a subgrid based, two-dimensional, depth-averaged model. This model uses a coarse computational grid in combination with a subgrid. The subgrid contains high resolution bathymetry and roughness information to compute volumes, friction and advection. The morphodynamic computations are carried out entirely on a high resolution grid, the bed grid. It is key to find a link between the information defined on the different grids in order to guaranty the feedback between the hydrodynamics and the morphodynamics. This link is made by using a new physics-based interpolation method. The method interpolates water levels and velocities from the coarse grid to the high resolution bed grid. The morphodynamic solution improves significantly when using the subgrid based method compared to a full coarse grid approach. The Exner equation is discretized with an upwind method based on the direction of the bed celerity. This ensures a stable solution for the Exner equation. By means of three examples, it is shown that the subgrid based approach offers a significant improvement at a minimal computational cost.

This chapter is published as Volp, van Prooijen, Pietrzak, and Stelling [35].

3.1. Introduction

Understanding the morphodynamic evolution of low land rivers, estuaries and coastal regions is of great importance. These systems, characterized by sub-critical flows, have been studied for many decades. The first steps in using numerical methods for modelling the morphodynamic evolution were in the seventies. The early models gave substantial insight into the possibilities of morphodynamic models, but also into difficulties [10]. Morphodynamic modelling is a multi-scale problem in which the gap in time scales between the short-term hydrodynamic forcing (hours, days) and the long-term morphological response (years, decades) needs to be bridged. Several methods have been proposed to deal with this gap in time scales [36, 37]. However, this problem is still relevant today. There is an urgent need for accurate and efficient morphodynamic models, which can simulate the evolution of large areas over decades [38–41]. These models are needed to study the sustainability and management of river and coastal systems over long periods of time.

We will introduce a subgrid based method for morphodynamic modelling to bridge the gap between the different time and length scales. We aim at preserving the accuracy that is related to high resolution simulations, while reducing the computational cost. The origin of the high computational cost related to morphodynamic simulations is strongly related to the computational cost for the hydrodynamic part. This computational cost can be reduced by using a coarse computational grid. However, the accuracy of morphodynamic simulations can benefit strongly from a high resolution computational grid. Therefore, we will introduce an approach that allows the hydrodynamics to be computed on a coarse grid, while the morphodynamics is computed at high resolution.

A recent development in the context of hydrodynamic modelling is the subgrid method [16, 42]. This method has been shown to be accurate, computationally efficient and elegantly deals with flooding and drying. This method was combined with a subgrid based approach for friction and strict momentum conservation [11]. Thanks to this approach we can now take advantage of high resolution bathymetry data in numerical simulations. These data become increasingly available with the advent of new measurement techniques, such as LIDAR [43] and multibeam echosounding. Subgrid methods are ever more applied in real case applications as they significantly improve the accuracy of the results [15, 25, 44, 45]. However, to our knowledge these methods have not yet been extended to morphological models.

The subgrid method for the hydrodynamic model is based on the assumption that the water level varies more gradually than the bed [16]. Therefore, two grids are used, a coarse computational grid and a (much) finer grid called the subgrid. The subgrid contains information at high resolution, such as bathymetry and roughness data. Subgrid based simulations make use of the precise cross-sections and volumes given by the high resolution bathymetry data. On that account, the accuracy of the full hydrodynamic solution increases significantly. This even allows for a reduction in the number of computational cells and thus a strong decrease of the computational cost. Vice versa, at a similar computational cost, the accuracy of the results is increased. Whether this enhanced efficiency can be obtained in combination with morphodynamic computations is the key question of this paper. The challenge is

how to make use of, and preserve the high resolution bathymetry data when the morphodynamics is driven by a flow model using a coarse computational grid.

We present a new subgrid based approach for morphodynamic modelling that can accurately and efficiently deal with the two dimensional, depth-averaged shallow water equations and the Exner equation. Within this study, we restrict ourselves to sub-critical flows, for which the hydrodynamic and the morphodynamic equations can be decoupled. There is a large community of scientist and engineers, who currently use this type of model for studying the evolution of coastal areas and low land rivers ([37, 39, 40, 46, 47], etc). In the classic approach for morphodynamic models all variables and operators of the hydrodynamic and morphodynamic simulations are defined on a single computational grid. In contrast, the method presented here solves the hydrodynamic equations on a coarse hydrodynamic grid, while using high resolution information defined on the subgrid [11]. In addition to that, the morphodynamic computations are carried out on the bed grid. The bed grid has the same resolution as the subgrid. This implies that the high resolution bathymetry information is updated during the morphodynamic simulation. As the hydrodynamic model makes use of the high resolution bathymetry information, the hydrodynamic solution directly takes variations into account.

For this approach it is essential to interpolate water levels and velocities from the coarse grid to the bed grid. The physics-based interpolation method as introduced here uses the coarse grid discharge, a simplified momentum equation and the high resolution bathymetry and roughness data in order to construct accurate water level values and velocities on the bed grid.

In addition to the subgrid based approach, an upwind discretization scheme is introduced for the Exner equation based on the bed celerity. The Exner equation is an advection equation without natural damping terms. This makes the equation sensitive to instabilities. This requires a numerical solution that suppresses spurious oscillations. The numerical diffusion should however be small, not to dampen physical instabilities that generates new morphological features (e.g. [48]). The strong non-linear coupling between flow and morphological response makes it difficult to deal with these instabilities. Typically, a bed slope effect or a diffusion term is added to the system for stabilization [49]. Alternatively, the stability of simulations can be enhanced by various methods such as a numerical filter [50], a predictor-corrector method and a diffusion term in the Exner equation and combinations of those [51]. In any case, the stability is strongly affected by the choice of the numerical scheme as well [37, 46, 47]. Upwind methods are often used to reduce instabilities. However, the choice of the upwind direction is generally taken in the direction of the sediment transport ([52, 53]). We show here that by choosing the upwind direction based on the direction of the bed celerity, instead of on the direction of the velocity, instabilities are damped.

In Section 4.3.1 the key aspects of the subgrid based hydrodynamic model are summarized. The key aspect in this section is the interpolation of the coarse grid quantities to the bed grid. Section 4.3.2 then describes the morphodynamic model and its discretisation, including the upwind scheme based on the bed celerity. The results of three classical test cases are presented in Section 4.4. Section 3.5 contains

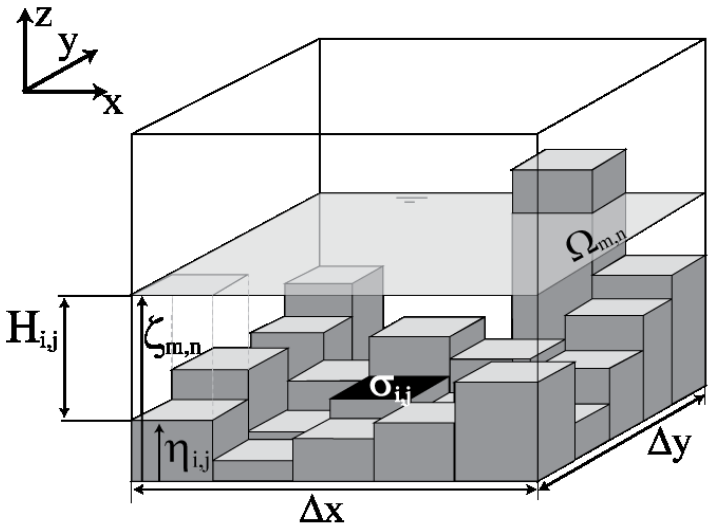

Figure 3.1: An overview of a coarse grid cell with an underlying subgrid. The water level $\zeta_{m,n}$ is uniform in the domain of a coarse grid cell, while the bed level $\eta_{i,j}$ varies within that domain. (Modified from [11])

the discussion and conclusion.

3.2. The hydrodynamic model

The hydrodynamic part is modelled with a subgrid based, two dimensional, depth-averaged model [11]. This subgrid approach is relatively new and as it forms an essential part of this paper, we will discuss the key aspects of the model. The coarse grid is the computational grid of the hydrodynamic model. A staggered, Cartesian grid is used, where water level points are located in the centre of a cell and velocity points at the cell edges. In this approach the bed level is allowed to vary within the domain of a computational cell. The bed level is defined on the subgrid, which is a fine structured grid with pixel cell sizes of $\sigma_p = \Delta x_p \Delta y_p$. Generally, this grid has the resolution of the best available bathymetry data. The varying bathymetry allows a computational cell and its cross-sections to be wet, partly wet or dry. Figure 3.1 is a sketch of a grid cell. Cell volumes, cell surfaces and cross-sectional areas become a function of the water level and the bed level. The hydrodynamic system becomes a weakly non-linear system that can be solved using a Newton iteration [16]. Within a momentum domain (the domain enclosed by two water level points), the velocity is a volume averaged quantity and is not assumed to be uniform as is generally the case. The subgrid based model allows the velocity to vary within that domain. This is important, in particular for the formulation of the friction and the advection.

Instead of determining the bed shear stress using cell averaged values for the roughness, the velocity and the water depth, the bed shear stress is defined on subgrid level. This means that local values for the water depth and the roughness are

used in combination with an estimate of the local (subgrid) velocity. This prevents an overestimation of the friction in areas characterized by strong variations in depth. For the strictly momentum conserving formulation of the advection, subgrid effects are also taken into account. For a more thorough explanation we refer to the original manuscripts [11, 16].

3.2.1. Interpolation of water levels and velocities

In the previous part it was explained that the velocities and water levels are resolved on the coarse hydrodynamic grid. To simulate the morphodynamics on the bed grid, we introduce a new method to interpolate the coarse grid quantities to the higher resolution of the bed grid. For simplicity it is assumed that the bed grid is as fine as the subgrid. The following procedure is used to obtain water levels and velocities in the centre of the pixels: i) the water level is interpolated; ii) the discharge is interpolated in streamwise direction and iii) the discharge is distributed over the bed grid cells to obtain velocities. The outcome of the interpolation method is a set of piece-wise continuous functions for the water levels and the velocities.

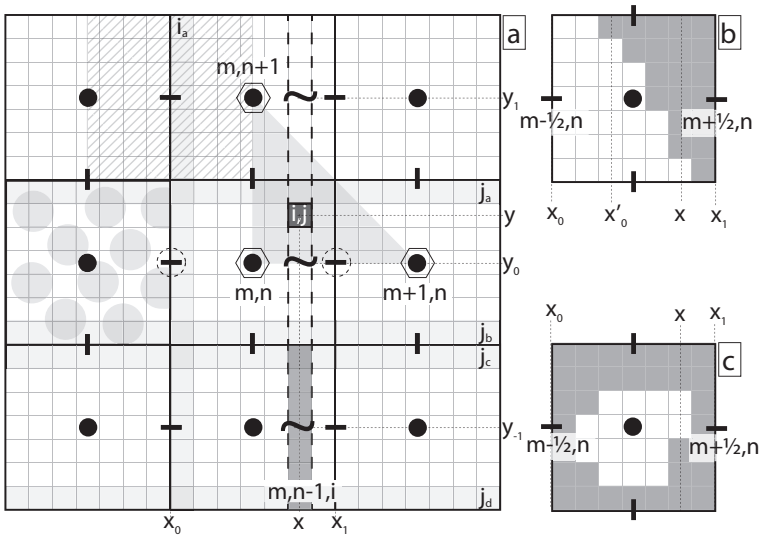

Figure 3.2: Water levels and velocities need to be interpolated from the coarse grid to the bed grid. In this sketch the variables needed for the derivation of the interpolation are included. Black dots are coarse grid water levels, stripes are coarse grid velocity points and the wiggles are locations where the friction slope is defined. The polka dotted area is an example of a water level domain, and the area with the diagonal dashes indicates an example of a momentum domain; a) fully wet cells b) partly wet cells with dry and wet faces c) partly dry cell with wet faces

The hydrodynamics can only be modelled accurately when the water level only varies gradually at length scales of the order of the grid resolution. Therefore, a linear three-point interpolation is sufficient to give a smooth water level field on the bed grid. The nearest, direct-connected neighbours of a high resolution water level point are considered for the interpolation. Coarse grid cells are connected when the

cross-sectional area at the edge of the cell is wet. For efficiency, we avoid checking the connectivity of more cells and thus using a higher order interpolation. The three surrounding coarse grid cells (indicated with the polygons in Figure 3.2.a) form a triangle. The water level in a pixel ζ_p for indices i, j is defined by the piecewise continuous function:

$$\zeta_{p:i,j} = \left(1 - \frac{(y-y_0)}{\Delta y} - \frac{(x-x_0)}{\Delta x}\right)\zeta_{m,n} + \frac{(x-x_0)}{\Delta x}\zeta_{m+1,n} + \frac{(y-y_0)}{\Delta y}\zeta_{m,n+1} \quad (3.1)$$

(for $x_1 \geq x > x_0 + \frac{1}{2}\Delta x_p$, $y_1 \geq y > y_0 + \frac{1}{2}\Delta y_p$). The variables x, y, x_0, x_1, y_0 and y_1 refer to locations in the grid, see Figure 3.2.a and $\zeta_{m,n}$ is the discrete coarse grid water level of the cell in which the pixel is located. In case a neighbouring coarse grid cell (for example with indices $m+1, n$) is dry, the water level used in equation 3.1 is assumed to be equal to that of cell (m, n). Throughout the manuscript, variables indicated with indices m, n are associated with the coarse (hydrodynamic) grid and indices i, j refer to the high resolution grids (both the subgrid and the bed grid, as these are assumed to have the same resolution).

For the interpolation of the velocities, it is key to account for the effect of variations in water depth and roughness on the flow. The velocity is however not a simple function of the local depth and the roughness. To illustrate this, we consider a uni-directional flow in a channel with a narrow trench. In the first case, the flow is in the same direction as the trench's central axis, resulting in a compound channel flow (Figure 3.3.a). For a flow in equilibrium, the velocity is determined by the Chézy equation: $u = C\sqrt{Hi_w}$ with velocity u, Chézy coefficient C, water depth H and water level gradient i_w. This explains that the highest velocities are found in the trench. In the second case, the trench's central axis is considered perpendicular to the main flow (Figure 3.3.b). If we assume a uniform water level gradient, the continuity equation leads to the relation between velocity and depth: $uH =$ uniform. Here, the lowest velocities are found in the trench.

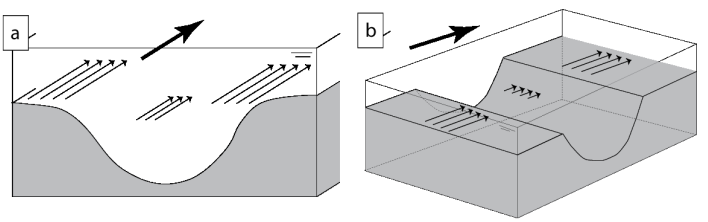

Figure 3.3: An uni-directional flow in a channel with a narrow trench. a) The central axis of the trench is in flow direction, resulting in a compound channel. b) The central axis of the trench is in perpendicular direction of the flow.

In order to construct a velocity field for both types of flow, we propose a two-step interpolation. First, the discharge is interpolated linearly in stream wise direction. Second, the simplified momentum balance for a steady, uniform flow is used for the lateral distribution of the discharge. Therefore, we call it the physics-based interpolation method. Finally, the high resolution velocity is expressed in terms of the coarse grid velocity, the local depth and roughness.

The first step in the interpolation of the velocity field is an interpolation of the discharge. The flow components in x- and y-direction are treated separately as they are located at different locations in this staggered grid. Here, we only describe the procedure in the x-direction. A similar procedure is used for the interpolation of the velocities in y-direction.

A coarse grid cell is split into several cross-sections per grid width, defined as sub-segments (indicated with a dark grey strip in Figure 3.2.a). The cross-section of sub-segment i in a coarse grid cell with index m, n is:

$$A^x_{i,n} = \sum_{j=1}^{J} H_{i,j} \Delta y_p \qquad \text{with} \qquad H_{i,j} = \max(0, \zeta_{p:i,j} - \eta_{i,j})$$

Index J is the number of pixels in y-direction per sub-segment. The water depth ($H_{i,j}$) is the difference between the water level and the bed level ($\eta_{i,j}$) (See Figure 3.1). The discharge in flow direction (here the x-direction) through such a sub-segment is determined by a linear interpolation of the coarse grid discharges ($Q^x_{m+\frac{1}{2},n} = A^x_{m+\frac{1}{2},n} u_{m+\frac{1}{2},n}$), which are defined at the edges of a cell:

$$Q^x_{i,n} = \frac{(x_1 - x)}{(x_1 - x_0)} Q^x_{m-\frac{1}{2},n} + \frac{(x - x_0)}{(x_1 - x_0)} Q^x_{m+\frac{1}{2},n} \tag{3.2}$$

$Q^x_{i,n}$ stands for the grid discharge in x-direction in a coarse cell with index n at sub-segment i, see Figure 3.2.a for further definitions. The second step is to distribute this grid discharge over the cross-section of the sub-segment, for this a simplified momentum balance is assumed. We assume that the dominant force balance is formed by the pressure gradient and the friction (see also [11]). The ratio of the two is defined as the friction slope and is assumed to be uniform over the sub-segment. The velocity can be expressed in terms of the friction slope (s) and a conveyance parameter ω:

$$u = \omega \sqrt{s} \qquad \text{with} \qquad \omega = \sqrt{\frac{g}{c_f} H} \tag{3.3}$$

in which g is the gravitational acceleration and c_f is the non-dimensional friction coefficient. Any formulation for the friction coefficient can be substituted, as for example Chézy or Manning. Note that for a steady uniform flow the friction slope equals the water level gradient. Integration over the cross-section allows the friction slope to be rewritten in terms of the discharge. At a cell with indices m, n and sub-segment i, the friction slope becomes:

$$s_{i,n} = \left(\frac{Q^x_{i,n}}{\sum_{j=1}^{J} \omega_{i,j} H_{i,j} \Delta y_p} \right)^2$$

The high resolution velocities ($u_{p:i,j}$) can now be computed. Yet, to construct a smooth velocity field, the high resolution velocities are based on the two nearest

friction slopes. In x-direction $u_{p:i,j}$ becomes:

$$u_{p:i,j} = \text{sign}\left(Q^x_{i,n}\right)\omega_{i,j}\sqrt{\left(\frac{(y_1-y)}{\Delta y}s_{i,n}+\frac{(y-y_0)}{\Delta y}s_{i,n+1}\right)} \quad \text{for} \quad j \geq \frac{1}{2}J$$
$$u_{p:i,j} = \text{sign}\left(Q^x_{i,n}\right)\omega_{i,j}\sqrt{\left(\frac{(y-y_{-1})}{\Delta y}s_{i,n}+\frac{(y_0-y)}{\Delta y}s_{i,n-1}\right)} \quad \text{for} \quad j < \frac{1}{2}J \quad (3.4)$$

The direction of the flow is based on the sub-segments discharge. Results of the interpolation are shown in Section 3.4.2.

The coarse computational cells can be dry, partly wet or wet. The method described here is suited for fully wet cells. When a cell is partly wet, the interpolation method is slightly adjusted. Two scenarios can be identified for cells that are partly wet. Either one or more of the coarse cross-sectional areas and neighbouring sub-segments are dry or the cross-sectional area of one or more of the sub-segments are decomposed in to two or more parts. Examples of these two scenarios are drawn in Figure 3.2.b and c. It is also possible to encounter a combination of these scenarios. The two scenarios require a slightly different approach.

In case when one or more of the coarse cross-sectional areas are dry, the discharge is again linearly interpolated. The interpolation is performed just for the wet sub-segments, as there cannot be a discharge at the dry segments. First, the wet sub-segments are identified. Secondly, the interpolation is performed between the first wet sub-segment and the coarse discharge known from the hydrodynamic part of the model. In case of the example of Figure 3.2.b equation 3.2 becomes:

$$Q^x_{i,n} = \frac{(x_1-x)}{(x_1-x'_0)}Q^x_{i'_0,n} + \frac{(x-x'_0)}{(x_1-x'_0)}Q^x_{m+\frac{1}{2},n}$$

in which i'_0 refers to the first wet sub-segment and $Q^x_{i'_0,n} = 0$. Note that the flow is forced to decelerate faster than when the domain is assumed to be fully wet.

Characteristic for Scenario 2 is when the wet domain of a sub-segment is not a closed area, so when one pixel or more in the middle is dry. This means that the flow is diverging. In such case the interpolation based on the discharge results in unrealistic results. Better results are obtained when the interpolation is based on the coarse grid velocity. This prevents artificially high velocities, because the cross-section is suddenly strongly reduced. In this case equation 3.2 becomes:

$$u_{i,n} = \frac{(x_1-x)}{(x_1-x_0)}u_{m-\frac{1}{2},n} + \frac{(x-x_0)}{(x_1-x_0)}u_{m+\frac{1}{2},n}$$
$$Q^x_{i,n} = u_{i,n}A^x_{i,n}$$

These two approaches can be, if necessary, combined.

Summarizing, the physics-based interpolation method is a two-step procedure. First, the coarse grid discharge is interpolated linearly in streamwise direction (Equation 3.2). Second, the discharge is distributed over a sub-segment in the cross-flow direction based on the simplified momentum equation for steady, uniform flow (Equation 3.4). This provides a smooth velocity field that can result both in increase or decrease of the velocity if the depth increases.

3.3. The morphodynamic model

3.3.1. Governing morphodynamic equations

The hydrodynamic model, which drives the morphodynamic system, is especially suited for gravity driven and friction dominated flows, which can be found in for example low land rivers and estuaries [11]. For these sub-critical type of flow systems, it is allowed to decouple the hydrodynamic and the morphodynamic systems, as long as the celerity of the water is much larger than the celerity of the bed [54]. The changes in flow and in bed level can in that case be computed successively per time step.

The evolution of the bed is described by the Exner equation, which can also be written in advective form:

$$\begin{aligned}(1-p)\frac{\partial \eta}{\partial t} &= -\frac{\partial q_x}{\partial x} - \frac{\partial q_y}{\partial y} \\ &= -\frac{\partial q_x}{\partial \eta}\frac{\partial \eta}{\partial x} - \frac{\partial q_y}{\partial \eta}\frac{\partial \eta}{\partial y}\end{aligned} \tag{3.5}$$

where η is the bed level (Figure 3.1), p the porosity of the bed and q_k with $k = x, y$ are the two components of the total sediment transport vector $\vec{q}$. Here, we already neglected temporal and spatial lag effects of suspended sediment transport [55]. The sediment flux $|\vec{q}|$ can be considered as a bed load flux (e.g. Meyer-Peter and Müller) or as a total load flux (e.g. Engelund Hanssen), see [56] for an extended overview of sediment transport formula. The terms $\frac{\partial q_x}{\partial \eta}$ and $\frac{\partial q_y}{\partial \eta}$ are the components in x- and y- direction of the bed celerity.

The simulations make use of the Morphological factor (M), to shorten the computational times[36]. The use of the morphological factor is independent of the subgrid-based approach and can be set to one. Also a diffusion term is implemented directly in the Exner equation (similar as in[51]). The diffusion is not required in order to keep the system stable, but to smooth small oscillations. This results in the following equation:

$$(1-p)\frac{\partial \eta}{\partial t} = M\left[-\frac{\partial q_x}{\partial x} - \frac{\partial q_y}{\partial y}\right] + MD\left[-|q_x|\frac{\partial}{\partial x}\left(\frac{\partial \eta}{\partial x}\right) - |q_y|\frac{\partial}{\partial y}\left(\frac{\partial \eta}{\partial y}\right)\right]$$

in which D is a dimensionless diffusion coefficient. In this case, we assumed a constant and uniform diffusion coefficient. The diffusion term can be turned off, by setting the diffusion coefficient to zero.

The sediment transport flux for all Meyer-Peter and Müller type of relations can be expressed in dimensionless form by using the Einstein parameter ([57] and references therein):

$$\begin{aligned}\Phi = \frac{|\vec{q}|}{\sqrt{RgD_{50}^3}} &= m(\theta - \theta_c)^p \qquad \text{for} \quad \theta \geq \theta_c \\ &= 0 \qquad\qquad\quad \text{for} \quad \theta < \theta_c\end{aligned} \tag{3.6}$$

in which D_{50} is the median grain diameter and $R = \frac{\rho_s - \rho}{\rho}$ is the relative density. The density of sediment and water are ρ_s and ρ, respectively. The coefficients m

and p are empirical parameters (defined in Table 3.1).The Shields parameter θ is given by:

$$\theta = \frac{\tau_b}{(\rho_s - \rho)gD_{50}} = \frac{c_f|U|^2}{RgD_{50}} \qquad \text{using} \qquad |U| = \sqrt{u^2 + v^2} \tag{3.7}$$

where τ_b is the bed shear stress and u and v are depth-averaged velocities in x- and y-direction, respectively. The critical Shields parameter θ_c gives the threshold for sediment motion. Various types of sediment transport equations can be implemented by defining m, p and θ_c differently [56]. The x- and y-component of the sediment fluxes are defined by [10, 52] :

$$q_x = \frac{u}{|U|}|\vec{q}| \qquad q_y = \frac{v}{|U|}|\vec{q}| \tag{3.8}$$

Note that the sediment transport relation is a function of the velocity, which is a function of the depth ($\vec{q}(\vec{u}) = \vec{q}(\vec{u}(\zeta, \eta))$).

Gravitational effects can influence the direction and the magnitude of the sediment transports. We have implemented this effect as described by [52]. This is a modified formulation from Bagnold (1966) [58]. The sediment flux adjusted to the slope in transport direction (q_{xs}, q_{ys}) in x- and y-direction is:

$$\begin{aligned} q_{xs} &= \alpha_s q_x \qquad \text{and} \qquad q_{ys} = \alpha_s q_y \\ \alpha_s &= 1 + f_s \left(\tan[\phi] \left(\cos\left[\tan^{-1}\left[\frac{\partial \eta}{\partial \mathrm{s}} \right] \right] \left(\tan[\phi] - \frac{\partial \eta}{\partial \mathrm{s}} \right) \right)^{-1} - 1 \right) \end{aligned} \tag{3.9}$$

where α_s is a parameter depending on the bed slope in streamwise direction ($\frac{\partial \eta}{\partial s} = \frac{q_x}{|\vec{q}|}\frac{\partial \eta}{\partial x} + \frac{q_y}{|\vec{q}|}\frac{\partial \eta}{\partial y}$, in which $|\vec{q}| = \sqrt{q_x^2 + q_y^2}$), the internal angle of the friction of the material of the bed ($\phi = 30°$) and on a tuning parameter f_s. In addition, the transport is also affected by the slope in cross-flow direction. Finally, the sediment transport including bed slope effects (q_{xsn}, q_{ysn}) becomes:

$$\begin{aligned} q_{xsn} = q_{xs} + \alpha_n q_{ys} \qquad \text{and} \qquad q_{ysn} = q_{ys} - \alpha_n q_{xs} \\ \alpha_n = f_n \sqrt{\frac{\tau_{cr}}{\tau_b}} \frac{\partial \eta}{\partial n} \end{aligned} \tag{3.10}$$

in which α_n depends on the cross-flow bed slope ($\frac{\partial \eta}{\partial n} = -\frac{q_y}{|\vec{q}|}\frac{\partial \eta}{\partial x} + \frac{q_x}{|\vec{q}|}\frac{\partial \eta}{\partial y}$), the critical and local shear stress and a tuning parameter f_n.

3.3.2. Discretisation

A finite volume method is applied for solving the Exner equation (Equation 3.5). Therefore, the sediment transport fluxes have to be known at the cell edges. However, for the computation of the sediment transport rates, information about the velocity, the roughness and the water depth are required. The physics-based interpolation method determines the flow velocities in the centre of the pixels, where the

depth and the roughness are defined. The sediment transport rates are based on these velocities, hence an upwind scheme is needed to solve the Exner equation.

The stability of the Exner equation is a known issue, as it is an advection equation without natural damping terms ([50, 51]). It can be proven that the continuous Exner equation cannot be stable without including a damping term by using a harmonic analysis technique and the theory of characteristics. A term for the bed slope effect in the sediment transport equation can serve as such a damping term.

By the lack of natural damping terms, the numerical approximation of the Exner equation is also sensitive to instabilities. The origin of the numerical instabilities can be linked to the non-linear depth dependence of the bed celerity [50]. These instabilities can become dominant over the actual evolution of the bed and can mask the natural morphodynamic behaviour. Therefore, it is essential to use a numerical method that deals with these instabilities. Adding a bed slope term is sometimes misused to stabilize the solution, as it is in fact a diffusion term. In principle, an effective method to stabilize the numerical solution is to use an upwind based discretisation scheme. This is, for example, applied in Delft3D [52] and in ROMS [53]. In these models the bed load transport vector is used to determine the upwind direction.

Characteristic theory can also show that perturbations in the bed can travel in all directions, even in the opposite direction to the sediment transport direction [49]. This can occur when the sediment transport is described as a non-linear function of the flow velocity. In such case the sediment transport direction can oppose the direction of the bed celerity. With this in mind we propose an upwind discretisation scheme based on the direction of the bed celerity. A first order method is applied, but higher order schemes are possible. First tests were already performed by [59].

With the use of a simple example, it can be illustrated that the direction of the velocity or the direction of the sediment transport can oppose the direction of the bed celerity. Therefore, consider the flow over a shallower area as shown in the four panels of Figure 3.4. Two locations are indicated: 1 represents the position in front of the shallow area and 2 the position at the top. When the expression for the celerity from Equation 3.5 is discretized at these locations, the bed celerity becomes:

$$c \approx \frac{\Delta q}{\Delta \eta} = \frac{q_2 - q_1}{\eta_2 - \eta_1} \tag{3.11}$$

For a steady, one dimensional flow in positive direction, the velocity will always increase for decreasing depth and vice versa ($u = \frac{Q}{HB}$, with B a uniform width), because of continuity (Figure 3.4.a). Therefore, in this one dimensional case the bed celerity will be in the same direction as the velocity and the sediment transport.

When considering a flow over a locally shallow area in a two dimensional system, the relation between depth and velocity is not known a priori ($u = u(Q, H, x, y, t)$). The relation between depth and velocity is complex and unknown, but the two dimensional velocity field is obviously affected by the local depth. It is possible that the flow in the shallower part is weaker than in the deeper part as the flow can go around the obstacle. In the situation illustrated in Figures 3.4.b and Figures 3.4.d the direction of the velocity opposes the direction of the bed celerity.

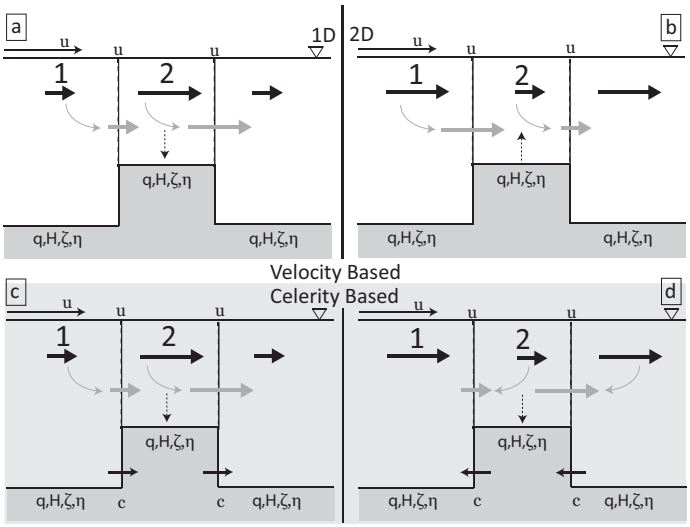

Figure 3.4: The upwind direction can be determined based on the direction of the velocity (panels a) and b)) or on the direction of the bed celerity (panels c) and d)). There is no net difference in the one-dimensional flow cases (a) and c)). See the text at equation 3.11 for a more detailed explanation.

When the wrong upwind direction is chosen the system becomes unstable, because in that case the Exner equation is actually solved with a (unstable) 'downwind' method. This is further illustrated in Figures 3.4.a-d. It is difficult to determine the bed celerity analytically as it is a non-linear function of the bed level and the shear stress, which itself is a non-linear function of the velocity. This makes it impossible for most bathymetries to determine the celerity beforehand. However, a numerical derivative as shown in Equation 3.11 allows to determine it for all types of bathymetries efficiently. It is possible to compute the celerity numerically without losing the conservative properties of the equations [60]. However, here a simplified method is applied as only the sign of the numerical derivative is used.

Considering the previous paragraphs, the Exner equation is discretized using a first order upwind method:

$$\begin{aligned}(1-p)\frac{\Delta\eta_{i,j}}{\Delta t}+ \quad & M\frac{\tilde{q}_{x:i+\frac{1}{2},j}-\tilde{q}_{x:i-\frac{1}{2},j}}{\Delta x_p}+M\frac{\tilde{q}_{y:i,j+\frac{1}{2}}-\tilde{q}_{y:i,j-\frac{1}{2}}}{\Delta y_p}+\dots \\ \dots+ \quad & MD|q_{x:i,j}|\frac{\eta_{x:i+1,j}-2\eta_{x:i,j}+\eta_{x:i-1,j}}{2\Delta x_p}+\dots \\ \dots+ \quad & MD|q_{y:i,j}|\frac{\eta_{y:i,j+1}-2\eta_{y:i,j}+\eta_{y:i,j-1}}{2\Delta y_p}=0\end{aligned} \tag{3.12}$$

where $\tilde{q}_x$ and $\tilde{q}_y$ are the sediment transport fluxes in upwind direction with respect to the celerity. Although, higher order discretisation schemes can be implemented too (for example equation 3.13), for simplicity we introduce this first order scheme.

For the x-direction:

$$\tilde{q}_{x:i+\frac{1}{2},j} = q^n_{x:i,j} \quad \text{for} \quad \frac{q^n_{x:i+1,j} - q^n_{x:i,j}}{\eta^n_{i+1,j} - \eta^n_{i,j}} > 0$$

$$\tilde{q}_{x:i+\frac{1}{2},j} = q^n_{x:i+1,j} \quad \text{for} \quad \frac{q^n_{x:i+1,j} - q^n_{x:i,j}}{\eta^n_{i+1,j} - \eta^n_{i,j}} < 0$$

$\tilde{q}_{x:i-\frac{1}{2},j}$ and $\tilde{q}_y$ are defined similarly. In case of a flat bed the equation above becomes singular and the upwind direction is determined based on the velocity direction.

3.4. Results

Three classical test cases are presented below: i) the evolution of a propagating dune; ii) the evolution of a two dimensional Gaussian peak and iii) the development of alternate bars in a straight channel. These examples are often used to test a morphological method [10, 52, 61, 62]. It was shown that the accuracy of hydrodynamic results improved significantly when the subgrid based hydrodynamic model was used [11]. To concentrate on the effect of the subgrid based method for the morphodynamics, these examples are chosen such that the hydrodynamic result is acceptable for the simulations with and without using the subgrid based approach. The first example is to show the effect of the use of a high resolution grid for the morphodynamics and its effect on the accuracy of the results. The second example shows that the observations for a one-dimensional case still hold in a two dimensional case where convergence and divergence of the flow play a role. Moreover, results of the physics-based interpolation method are shown. Finally, the third example shows that the method is also effective to generate morphodynamic features and that it works in a much more complex setting, which exists at the end of the simulation. Specific model and parameter settings are defined for each example separately, more general settings are included in Table 3.1 for all three examples.

3.4.1. Dune in straight channel

We consider a straight uniform channel with a dune that is uniform in cross-flow direction (Figure 3.5). In this example, the proposed velocity interpolation should be nearly ideal as the velocity follows almost directly from the continuity equation, see Section 3.2.1. Three aspects are investigated with this example: i) The effectiveness of the subgrid is tested by comparing results from simulations with and without subgrid to results from a full high resolution solution. ii) By varying the coarse grid resolution the effect of the ratio between coarse grid and subgrid is determined. iii) The error of the solution of the simulations based on the subgrid method is investigated. Therefore a comparison is made between the error of the discretisation method with a first order and a second order scheme.

A modelling domain of 64 m wide and 640 m long is used, in which the bathymetry is defined on a 1×1 m^2 resolution grid. The top of the dune is 0.5 m higher than the bed level of the channel. The width of the foot is about 30 m long. At the inflow boundary a constant velocity is prescribed and downstream a constant water level is set. Eleven simulations (A-K) are defined to test aspects i-iii. Simulations A-C,

Table 3.1: Input values for the three test cases. C is the Chézy coefficient, M is the morphological factor, Δt the time step and D_{50} the sediment size. Also the critical shear stress (τ_c) and the coefficients m and p of the MPM sediment formulation are given. The boundary conditions are given in terms of the water level (ζ_b), the discharge (Q_b) and the velocity (u_b). The mean water depth (H_b) is given as well. Finally, also the maximal value of the dimensionless diffusion coefficient (Dif) is included.

	Uniform dune	Gaussian peak	Alternate bars
C	50 $m^{\frac{1}{2}}$ s^{-1}	50 $m^{\frac{1}{2}}$ s^{-1}	50 $m^{\frac{1}{2}}$ s^{-1}
M	500	500	10
Δ t	0.3 s	0.3 s	200 s
D_{50}	200 μm	200 μm	100 μm
θ_c	0.0566	0.0566	0.047
m	5.7	5.7	5.7
p	$\frac{3}{2}$	$\frac{3}{2}$	$\frac{3}{2}$
Q_b	-	-	1600 $m^3 s^{-1}$
u_b	1.383 ms^{-1}	1.383 ms^{-1}	-
ζ_b	2.0 m and 7.0 m	7.0 m	0.0 m
H_b	5.0 m and 10.0 m	10.0 m	5.47 m
Dif_{max}	10^{-5}	$0 - 10^{-5}$	$3 \cdot 10^{-5}$
f_s	0	0	1
f_n	0	0	1

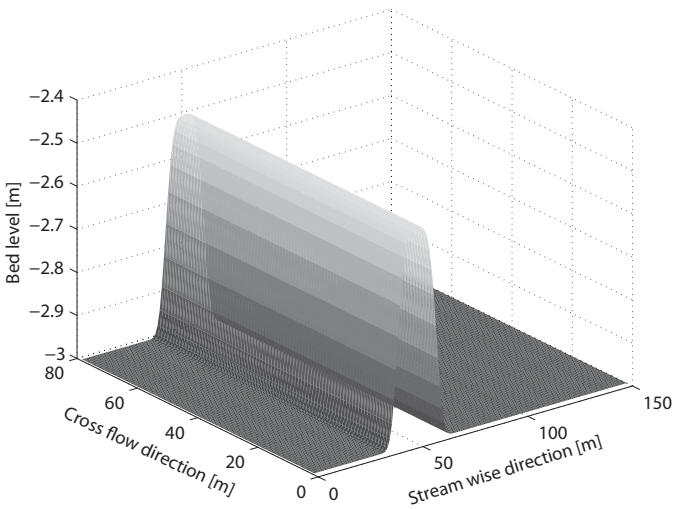

Figure 3.5: The bathymetry of the dune used in Section 3.4.1. The dune is uniform in cross flow direction.

F and I are five reference runs, for which both the hydrodynamics and morphodynamics are computed on a grid with the same resolution. Simulations A,F and I are high resolution runs, while simulations B and C are run with a coarser grid (B: $\Delta x = \Delta y = 4$m and C: $\Delta x = \Delta y = 8$m). Simulations D (G, J) and E (H, K) use the same resolution as simulations B and C, respectively. However, simulations D (G, J) and E (H, K) account for the subgrid in the hydrodynamic computations and the Exner equation is solved on the high resolution bed grid. Simulations A, D, E are very similar to simulations F, G, H, but these are run for different water levels, while simulations I, J, K use a second order accurate discretisation scheme. Tables 3.1 and 3.2 summarize the details of the simulation settings.

Table 3.2: Overview of simulations for the uniform dune

Simulation	Resolution coarse grid	Depth	Relative CPU time	Discretisation
A	$1 \times 1\ m^2$, no subgrid	5 m	100 %	first order
B	$4 \times 4\ m^2$, no subgrid	5 m	1.4 %	first order
C	$8 \times 8\ m^2$, no subgrid	5 m	0.4 %	first order
D	$4 \times 4\ m^2$, with subgrid	5 m	7.2 %	first order
E	$8 \times 8\ m^2$, with subgrid	5 m	3.0 %	first order
F	$1 \times 1\ m^2$, no subgrid	10 m	100 %	first order
G	$4 \times 4\ m^2$, with subgrid	10 m	7.2 %	first order
H	$8 \times 8\ m^2$, with subgrid	10 m	3.0 %	first order
I	$1 \times 1\ m^2$, no subgrid	10 m	100 %	second order
J	$4 \times 4\ m^2$, with subgrid	10 m	7.3 %	second order
K	$8 \times 8\ m^2$, with subgrid	10 m	3.1 %	second order

Figure 3.6 shows the development of the dune for three reference simulations (A-C). Snapshots of the longitudinal profile are plotted at various moments in time. The high resolution simulation shows the propagating dune, the diffusion and the associated lowering of the peak height. The differences between the simulations indicate a strong grid dependence. The dune propagation speed is increasingly underestimated by the use of a coarser mesh. Moreover, the diffusion increases as well for larger grid sizes. This results in an stronger lowering of the peak.

In comparison, Figure 3.7 shows the evolution of the dune for the simulations that use the subgrid based approach (D and E) and as a reference the high resolution simulation (A). Compared to the reference simulation the decrease in resolution leads to a slightly lower peak level. However, the propagation speed and width of the dune are captured very well.

The deviation in peak height increases in the first period of the evolution up to approximately 1 centimetre for simulation D and up to approximately 2 centimetres for simulation E, but it does not grow in later stages. This deviation originates from the assumption of a uniform water level within a coarse grid cell. The water level varies near the top of the dune, due to the dynamic pressure. This is not

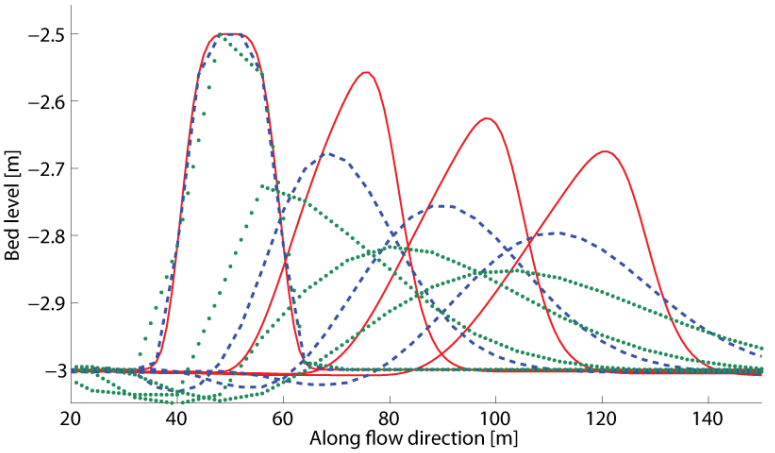

Figure 3.6: The evolution of a dune. The initial longitudinal profile and the profile at three subsequent moments in time are shown for simulations A (red line), B (blue dashed line) and C (green dotted line). These are the simulations which do not account for any subgrid information.

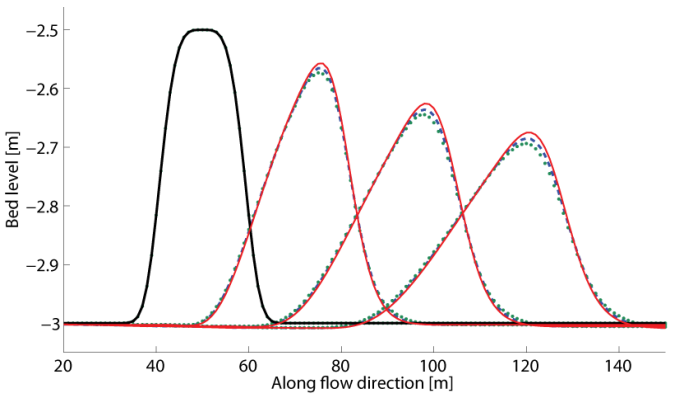

Figure 3.7: The evolution of a dune. The initial longitudinal profile and the profile at three subsequent moments in time are shown for simulations A (red line), D (blue dashed line) and E (green dotted line). Simulation A is the high resolution simulation and D and E use the subgrid information.

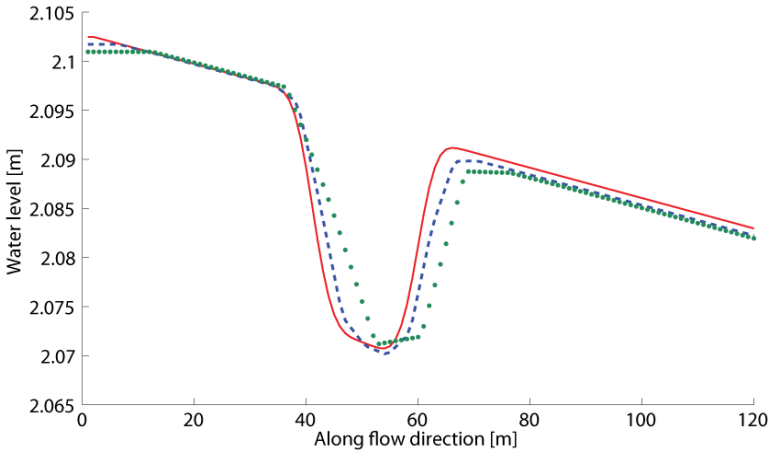

Figure 3.8: The water level at the beginning of the morphodynamic simulation, for simulations A (red line), D (blue dashed line) and E (green dotted line).

captured accurately by simulations D and E due to lack of water level points as can be seen in Figure 3.8. Here, the water level is plotted for simulations A, D and E at the beginning of the simulation. At later stages, when the dune decreases in height, the relative effect of the dynamic pressure is smaller. This is confirmed, when simulations similar to A, D and E are performed only with a larger water depth (Simulations F, G and H, Figure 3.9).

For a purely kinematic simulation (no water level variation, no diffusion, no friction), the dune will only propagate and deform. The front will become steeper and the tail milder. However, when modelling a kinematic wave neither the effect of the dynamic pressure nor the bottom friction is taken into account. Nevertheless, the decrease of the dune in Figure 3.6 is mainly caused by numerical diffusion, as the diffusion term was very small. This diffusion could be caused by the subgrid assumptions, the interpolation and by the numerical scheme of the morphodynamic simulation. As the reference run shows diffusive behaviour as well, the diffusion is expected to originate mainly from the numerical scheme. To decrease the numerical diffusion, a second order upwind scheme [1] is implemented as well. Figure 3.9 shows the results for the first order and second order upwind scheme. As expected the

[1] Equation 3.13 becomes for a second order upwind scheme:

$$(1-p)\frac{\eta_{i,j}^{n+1}-\eta_{i,j}^{n}}{\Delta t}+\frac{\tilde{q}_{x:i+\frac{1}{2},j}-\tilde{q}_{x:i-\frac{1}{2},j}}{2\Delta x_p}+\frac{\tilde{q}_{x:i,j+\frac{1}{2}}-\tilde{q}_{y:i,j-\frac{1}{2}}}{2\Delta y_p}=0$$

in which:

$$\begin{aligned}\tilde{q}_{x:i+\frac{1}{2},j}&=3q_{x:i,j}^{n}-q_{x:i-1,j}^{n} \quad \text{for} \quad \frac{q_{x:i+1,j}^{n}-q_{x:i,j}^{n}}{\eta_{i+1,j}^{n}-\eta_{i,j}^{n}}>0\\ \tilde{q}_{x:i-\frac{1}{2},j}&=3q_{x:i-1,j}^{n}-q_{x:i-2,j}^{n} \quad \text{for} \quad \frac{q_{x:i,j}^{n}-q_{x:i-1,j}^{n}}{\eta_{i,j}^{n}-\eta_{i-1,j}^{n}}<0\end{aligned} \tag{3.13}$$

And a similar discretisation in y-direction.

damping of the dune is smaller for the second order scheme. Important to note is that the the diffusivity due to the discretisation is dominant over the diffusivity caused by the subgrid based approach for the hydrodynamics and the velocity interpolation.

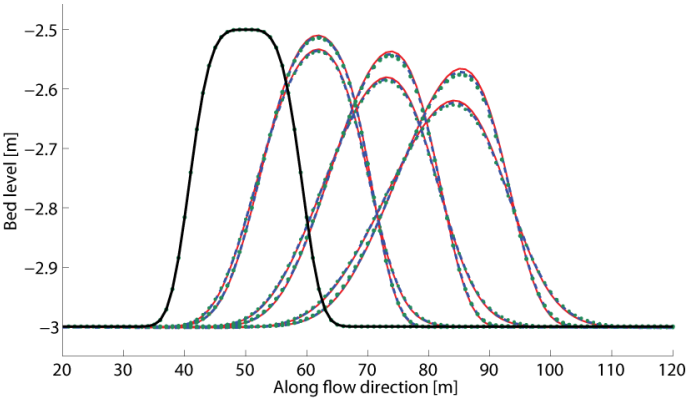

Figure 3.9: The bed evolution of the dune is given for simulations F-K. Simulations F and I are the high resolution simulations (red line), simulations G, J (blue dashed line) and H, K (green dotted line) use a coarser computational grid. The lower successive dunes are modelled with a first order discretisation and the top successive dunes with a second order discretisation.

The computational cost of the simulations are expressed in terms of the CPU-time. The computational cost of the simulations are given in Table 3.2 in percentages of the high resolution simulation. A percentage of for example 10 % would imply that the simulation is 10 times faster than the high resolution simulation. Reducing the resolution of the hydrodynamic grid leads to a significant reduction in computational cost. In case of the subgrid based simulations, this reduction comes with a minimal loss in accuracy.

3.4.2. A 2D Gaussian peak

The second example is the evolution of a 2D Gaussian peak. It shows the performance of the model in a two-dimensional setting. The difficulty of this example is that the flow diverges in front and converges behind the peak. Nevertheless, this example shows that generally the same performance of the subgrid based approach in 2D is achieved compared to the one dimensional case. Results from the velocity interpolation are shown and compared to the high resolution velocity field.

The domain is 250 m wide and 450 m long. The peak in bed level is defined by a Gaussian function with standard deviation $\sigma = 13$ m and a maximum of $\eta_{max} \approx 1$ m (Figure 3.10). A constant velocity in x-direction and equilibrium bed load transport is prescribed at the inflow boundary and a constant water level is set at the outflow boundary. The resolution of the bathymetry is 1×1 m^2, which is also the resolution of the subgrid and the bed grid.

Results for five different simulations are shown. Simulation A is the reference run for which the resolution of the hydrodynamic grid equals the resolution of the bed grid (1×1 m^2). Simulations B and C use a coarse computational grid for the

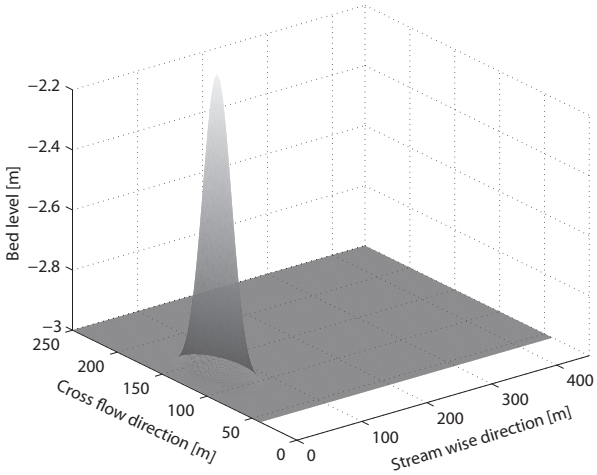

Figure 3.10: The bathymetry of the Gaussian peak as described in Section 3.4.2.

Table 3.3: Overview of simulations for the 2D Gaussian peak.

Simulation	Resolution coarse grid	Relative CPU time	Upwind	D
A	$1 \times 1\ m^2$	100 %	Celerity	10^{-5}
B	$5 \times 5\ m^2$	2.9 %	Celerity	10^{-5}
C	$10 \times 10\ m^2$	1.8 %	Celerity	10^{-5}
D	$10 \times 10\ m^2$	1.8 %	Celerity	0.0
E	$10 \times 10\ m^2$	1.8 %	Velocity	0.0

hydrodynamic part and a high resolution grid to solve the Exner equation. Simulations B and C use a coarse grid with cells of 5×5 m^2 and 10×10 m^2, respectively. The resolution of the bed grid is the same as used for the reference simulation. In order to compare the effect of choosing the upwind direction based on the celerity instead of the velocity direction, simulations D and E are performed. Simulation D and E have the same settings as simulation C, but the diffusion coefficient is zero. Moreover, for simulation E the upwind direction is based on the velocity direction. The results of the reference runs with a similar grid resolution as simulations B and C are not shown, as they show comparable poor behaviour as was seen in the uniform dune example. The settings of the simulations A-E are given in Tables 3.1 and 3.3.

First, the interpolated velocities from simulation C are compared with those of the reference simulation A. Figure 3.11 shows the velocities in x- and y-direction for simulation A (sub-figures a,b), the coarse grid velocities in both directions of simulation C (sub-figures c,d) and the interpolated velocities on the high resolution

grid (sub-figures e,f). Even though the coarse grid velocity is rather patchy, good agreement is found between the velocities of the reference run and the interpolated velocities of simulation C.

Secondly, the evolution of the bed level is plotted in Figure 3.12, which shows four snapshots of the evolution of the peak (simulation C). The three-point-star shape [10] is well captured even though the flow is modelled with a relatively coarse grid. To make a more quantitative comparison, cross-sections of the bed level along the centre-line are drawn in Figure 3.13 at several moments in time. Similar to the one dimensional case, good agreement is found between the subgrid based simulations with coarse grids (B and C) and the reference simulation A. The peak of simulation C is however slightly lagging behind the peaks of simulations A and B. The wavelength of the dune of simulation C becomes longer and the peak has decreased more.The high resolution velocity field from this coarsest model is difficult to capture correctly as the flow diverges and converges within a small spatial domain relative to the coarse grid size. For resolutions that are much coarser, the triangular spreading of the peak is not captured well.

The computational cost is expressed in percentages of the CPU time of simulation A. Table 3.3 shows that simulation C needs only 1.8 % of the computational time of simulation A. This is achieved by reducing the resolution of the hydrodynamic model, while the morphodynamic solution is still accurate.

In Section 3.3.2, it is proposed to use the sign of the bed celerity to define the upwind direction. Figure 3.14 shows the sign of the bed celerity in x-direction. There are large regions where the celerity opposes the direction of the flow. For comparison simulation E is run, in which the upwind direction is based on the velocity direction. Figure 3.15 shows the bed evolution for simulations D and E. The difference lies in the method for choosing the upwind direction. In simulation D the upwind direction is still based on the bed celerity and in simulation E on the velocity. In both simulations there is no additional diffusion added to the system (Table 3.3). After 21100 time steps, simulation E becomes unstable. Before that moment, the development of the bed level is not well represented: the propagation of the peak is underestimated. Such instabilities could be controlled by adding extra diffusion to the system, but this will influence the solution too by lowering and widening of the peak.

3.4.3. Development of Alternate Bars

In the previous examples, the development of a pre-defined bed shape was simulated. In this example, we simulate the generation of morphological features at a scale of a real life case. We base the parameter settings on a typical low land river (Table 3.1) with a width to depth ratio of 45. According to non-linear perturbation theory bars will develop for such a specific ratio (see [48, 63–65]). Based on the theoretically fastest growing mode, bars of a length of approximately 870 m are predicted with an amplitude of about 80% of the equilibrium water depth. However, these weakly non-linear perturbation theories tend to underestimate the length of the bars as at a certain moment the non-linear effects dominate the behaviour. Moreover, analytical studies show that the fastest growing mode is only moderately

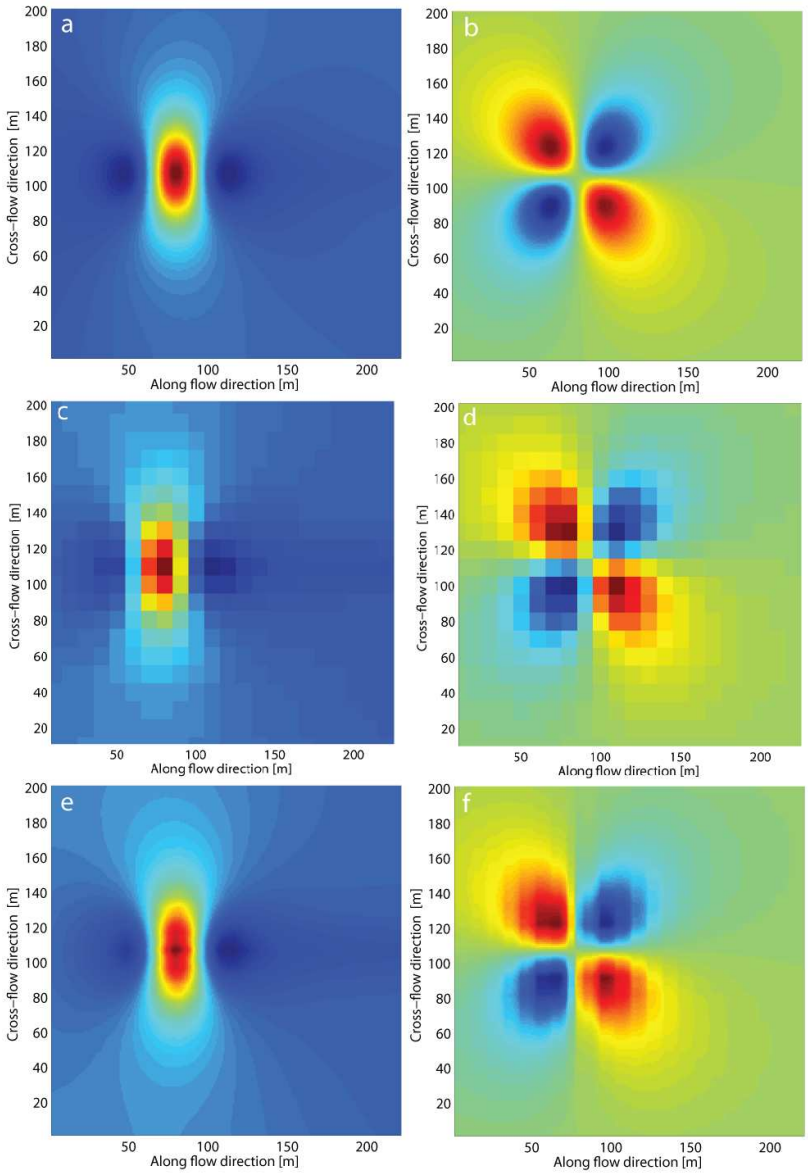

Figure 3.11: The velocity field for simulations A and C. a) Simulation A x-direction b) Simulation A y-direction c) Simulation C coarse grid x-direction d) Simulation C coarse grid y-direction e) Simulation C subgrid x-direction g) Simulation C subgrid y-direction. The velocity in x-direction ranges from blue (1.36 ms^{-1}) to red (1.45 ms^{-1}) and in the y-direction from blue (-0.02 ms^{-1}) to red (0.02 ms^{-1}) .

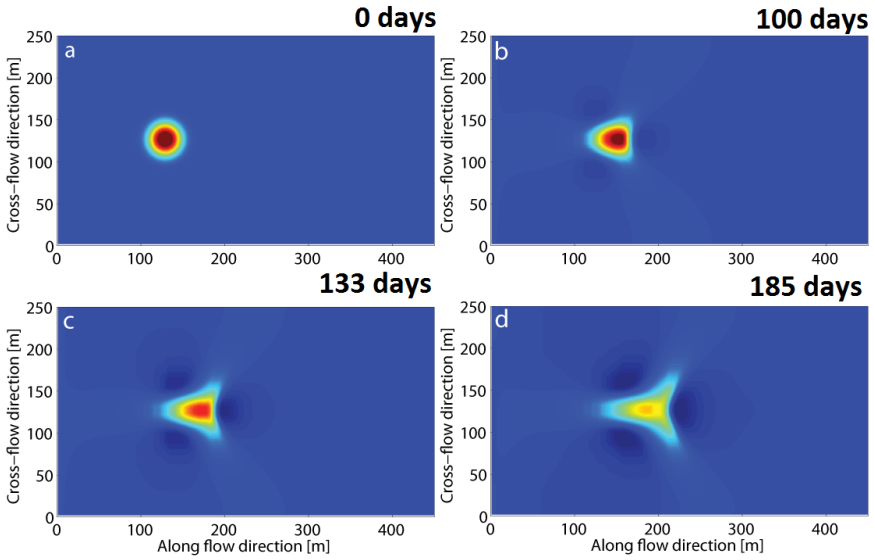

Figure 3.12: Four snap shots in time (a, b, c, d) of the evolution of the Gaussian peak. Warm colours indicate a higher bed level.

selective on wave number [48]. This was found in laboratory experiments [66] and in numerical simulations [67].

We consider a channel with a width of 250 m and a length of $15 \cdot 10^3$ m. The bed is defined on a mesh with a resolution of $5 \times 5\,\mathrm{m}^2$. Initially, the bed level is set to the equilibrium condition with a slope of $1.0 \cdot 10^{-4}$. Small perturbations of about 5% of the equilibrium depth ($H_{eq} = 5.47$ m) were imposed to initiate the generation of instabilities. At the inflow boundary a discharge and a sediment load is prescribed and downstream a water level is set, which all correspond to their equilibrium values. The result of seven simulations (A-G) are here presented. Simulations A-C are reference runs that use the same grid resolution for the hydrodynamics and for the morphodynamics. Simulation A has a resolution of $5 \times 5\,\mathrm{m}^2$ and is the high resolution simulation. Simulations B and C have a grid resolution of $30 \times 5\,\mathrm{m}^2$ and $40 \times 15\,\mathrm{m}^2$. The subgrid based simulations are D-G of which the hydrodynamic grid varies from fine to coarse: $30 \times 5\,\mathrm{m}^2$, $40 \times 15\,\mathrm{m}^2$, $80 \times 50\,\mathrm{m}^2$ and $160 \times 100\,\mathrm{m}^2$, respectively. They all use the high resolution grid of simulation A to solve the Exner equation.

The bars that develop in the channel are migrating bars. Figure 3.16 shows the bathymetry for the various simulations at the same moment in time. To visualize the bars, the equilibrium depth is subtracted from the bed level. We focus on the down stream half of the channel as that is where the mobile bars are best developed, which is also observed in experiments [66]. The Figures 3.16.a to g correspond to simulations A to G.

The bars of simulation A have a length of ± 1000 m and an amplitude of ±

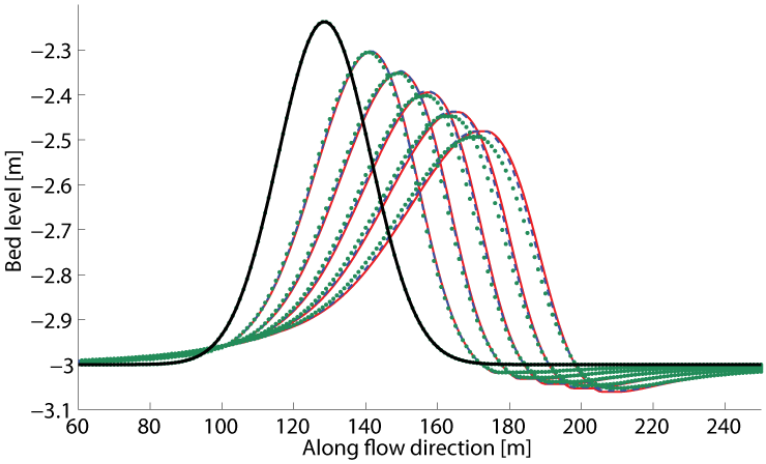

Figure 3.13: The longitudinal profile of the Gaussian peak. The bold line is the initial profile, five successive dunes are given for simulations A (red line), B (blue dashed line) and C (green dotted line).

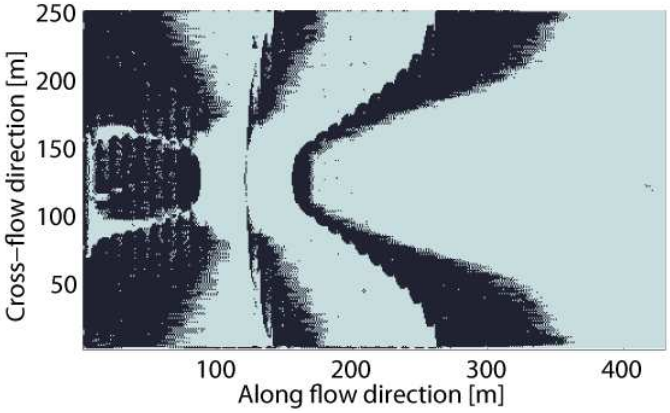

Figure 3.14: The sign of the x-component of the bed celerity for the initial bathymetry, light is positive, black is negative.

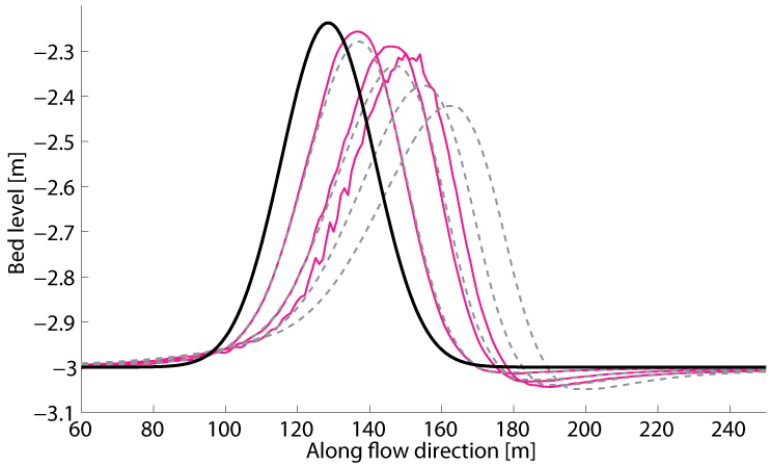

Figure 3.15: The longitudinal profile of the Gaussian peak. The bold, black line is the initial profile, five successive dunes are given for simulations D (gray dashed line) and E (pink line).

4.3 m. The length is indeed somewhat longer than which is estimated based on the analytical models. The reference simulations B and C based on the coarser grid resolutions are not able to generate any bars. However, bars did develop in the simulations with a similar computational grid size when using the subgrid based approach (simulations D and E). Even for the simulations using a more coarse hydrodynamic grid, bars appear. The shape of the bars varies for various resolutions. Especially, the coarsening of the grid in cross-flow direction has a significant effect. However, the bars in simulations D and E have an amplitude of $4 - 4.5$ m, which is about $73 - 82$ % of the total water depth. The amplitude of the bars in simulation F is approximately 2.0 m. The grid is too coarse to capture the dynamics properly. Although, in later stages of the simulations, the bars from simulation F grow further to larger amplitudes. In simulation G this is even more clear, the bars have only a very limited amplitude, a different colour scale is used. We adjusted the scale in order to visualize that the structures that develop, although small, are similar to the alternate bars. The length of the bars from simulations D to G are between $1000 - 1200$ m, similar to the reference simulation A. Initially, bars with a length of about 600 m started to grow. In later stages the length increased when the amplitude grew too. Although the shapes of the bars are varying with the resolution, the length of the bars in plots A, D to G is similar.

In simulations A and D are some wiggles present. These features migrate, but do not grow in time. These can be suppressed by adding more diffusion or numerical filters. Such methods can be added to the system, but the subgrid based approach is here presented in a simple form. Methods to smooth results as described in for example [51], can be applied, as this is independent of the subgrid method.

The coarse grid simulations B and C do not perform well, due to the sensitivity of this system for the amount of diffusion. Too much diffusion suppresses the growth of the perturbations to bars. Diffusion can originate from the numerical scheme

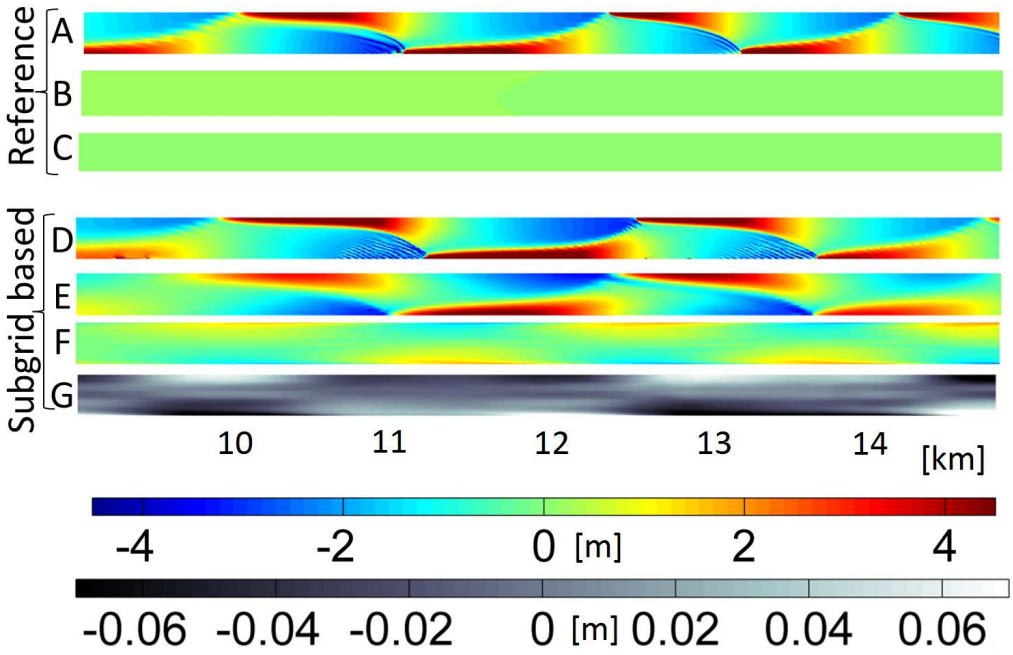

Figure 3.16: Bathymetry plots of second half of the channel for simulations A-G. Colour-bars show the amplitudes of the bars in [m]. The bathymetry values are normalized for the overall bed slope, for better visualization.

and from the added diffusion term. In these coarse grid simulations the numerical diffusion in the system is significantly larger compared to the simulations performed on the high resolution bed grid. This is a consequence of the dependence of numerical diffusion to the grid size. The diffusion coefficient used in these examples is the same for all cases. The results of the coarse grid simulations are also affected by an underestimation of the local bed slope effect (Equations 3.9 and 3.10), as the slope is spread over a larger domain.

The coarse grid simulations that make use of the bed grid are also affected by the forcing on coarse grid scale, however not as strong as the simulations that do not make use of the subgrid based approach. In these coarse grid simulations (F and G), the lateral flow cannot develop properly. In those cases the lateral forcing is not simulated correctly in the hydrodynamic flow due to a lack of resolution.

3.5. Discussion and conclusion

In various papers it was shown that simulations run with a subgrid based hydrodynamic model are accurate, even when large computational cells were used [11, 16, 25, 26, 42, 44]. The increase in accuracy is obtained with a limited computational cost. The accuracy increased because the bathymetry of the system is well described even in coarse grid simulations. The key question here was whether this enhanced efficiency could also be used in combination with morphodynamic simulations. Therefore, the high resolution information should be preserved and updated during the simulations. We developed a subgrid based approach for morphodynamic simulations in order to increase the accuracy of the morphodynamic simulations and to make use of the efficiency of the subgrid based approach.

The focus is on two dimensional, depth averaged morphodynamic simulations forced by sub-critical flow. In this case the hydrodynamic and the morphodynamic equations can be decoupled. Various studies have shown that these type of models are adequate for many applications [39, 68, 69]. The subgrid based approach uses two different grid resolutions. The hydrodynamics are modelled on a coarse computational (hydrodynamic) grid. The model uses a subgrid to take high resolution bathymetry and roughness data into account. The bed grid is equal to the subgrid in the hydrodynamic model and is used to solve the Exner equation. The coarse grid variables are interpolated to the bed grid using a physics-based interpolation method. The high resolution velocity field should be realistic and smooth for a wide range of applications. Therefore, a simple linear interpolation is not sufficient. The new physics-based interpolation method uses continuity and a simplified momentum balance (pressure gradient in balance with friction) in order to determine the high resolution velocity field. Based on this velocity field sediment transports rates are computed and the Exner equation is solved. This improved the morphodynamic solutions significantly when compared to simulations that do not use the subgrid based approach and endured only a slight increase in computational cost.

The aim of the subgrid based approach is to improve the accuracy of coarse grid simulations. The use of the various grid resolutions does improve the result. Nonetheless, certain processes are not captured when using a coarse grid. One should be aware of the restrictions of the method. The limitations of the hydrodynamic

model are known [11]. However, the key aspects are summarized here, as the morphodynamic model inherits these limitations from the hydrodynamic model. Three assumption were required to set up the hydrodynamic model; i) the water level is uniform within a coarse grid cell; ii) the flow within a coarse grid cell has a uniform direction and iii) the high resolution velocity scales linearly with the coarse grid velocity. The first assumption implies that in areas where the water level changes rapidly, for example due to the dynamic pressure, the water level gradient is not resolved completely. This could have consequences for the direction and magnitude of the flow. The other two assumptions exclude convergence and divergence of the flow within a cell as well as circulations within such a domain.

The assumption of excluding circulations and divergence or convergence of the flow within a cell is also made for the interpolation of the velocity field. The continuity and momentum equations are solved on the coarse hydrodynamic grid only and thus circulations within the cell are not constrained naturally within a grid cell. Therefore, when interested in specific circulations, the coarse grid resolution should be chosen fine enough to capture those. They cannot be captured on subgrid level. The high resolution velocities are based on the local depth, the coarse grid velocities and the interpolated water level. The high resolution velocities do not conserve mass and momentum. However, the velocities are just used to compute the sediment transports, which are empirical relations. Meantime, at coarse grid the mass and momentum of water is fully conserved and the sediment mass is conserved at high resolution. Therefore there is no violation of continuity. There is no feedback from the high resolution velocities to the hydrodynamic system.

The restrictions described here imply that the choice of resolution of the hydrodynamic grid and the morphodynamic grid should be made carefully. Generally, the resolution of the morphodynamic grid can be chosen higher than that of the hydrodynamic grid. In principle, the resolution of the subgrid is the resolution of the best available bathymetry data. If the resolution of the data becomes very high, in the order of magnitude of the bed roughness features, the friction formulation used here, might overestimate the friction. When choosing the coarse grid one needs to investigate what the essential flow characteristics are that one has to capture within the grid. However, it is not possible to provide an ideal ratio between the grid resolutions. This depends not only on the availability of the bathymetry data, but also of the type of flow, the bed characteristics and also the processes one is interested in. This is not different from setting up any other model.

In this paper the resolution of the morphodynamic grid was chosen equal to that of the subgrid. However, a different grid resolution can be used for the morphodynamic model. From the computational times in the examples, it is clear that the cost does increase by computing the morphodynamics with a high resolution. However, the set up of the presented model, the algorithms of both the velocity reconstruction and solving the Exner equation can be parallelised easily, as the stencils are small and the outcomes are independent of each other. This will result in an even lower computational cost.

A celerity based upwind method was introduced for the discretisation of the Exner equation. The formulation proved to have a stabilizing effect on the morpho-

dynamic solution. Although, a first order upwind scheme is a relatively diffusive system, the solutions did not remain stable when the upwind direction was chosen based on the sediment transport direction when no extra diffusion was added.

We presented here the subgrid based approach for a structured Cartesian grid. However, the basic idea of using different grids for the morphodynamics and the hydrodynamics can be applied to any grid structure. It is the interpolation of the water levels and velocities that connects the different grids. The water level interpolation from the coarse to the fine resolution grid is a simple linear formulation, which can be applied to any grid structure. However, for the velocity a physics-based interpolation method is introduced. The method interpolates the velocity in flow direction based on discharge and in cross-flow direction based on friction. This is, in principle, independent of the grid structure as well and can be applied to grid structures that allows local grid refinements. The method introduced here can be applied directly to, for example, quad-tree based refined grids (see for example in combination with subgrid [45]). However, when applied to unstructured grid models [42], the implementation of the interpolation needs to be adjusted to that specific grid structure.

We have shown that a subgrid based hydrodynamic model can be coupled to a high resolution morphodynamic model. In order to connect the models a physics-based interpolation of the velocity field is required. Furthermore, we have shown that this leads to a substantial increase in accuracy for a minimal computational cost.

Acknowledgement

The work presented in this paper is carried out as part of the innovation program Building with Nature. The Building with Nature program is funded from several sources, including the Subsidieregeling Innovatieketen Water (SIW, Staatscourant nrs 953 and 17009) sponsored by the Dutch Ministry of Transport, Public Works and Water Management and partner contributions of the participants to the Foundation EcoShape. The program receives co-funding from the European Fund for Regional Development EFRO and the Municipality of Dordrecht.

4

A Subgrid Based Approach for Suspended Sediment

Numerical models for the simulation of sediment dynamics have proven to be indispensable for many studies. They are used, for example, to assess the effects of anthropogenic interferences and climate change on rivers, estuaries, and coastal seas. For these types of investigations, there is a need for fast and accurate morphodynamic models. We present a fundamentally new approach to simulate morphodynamics due to suspended sediment transport. Using different resolutions to solve the set of equations, the accuracy of a simulation is increased significantly, for a limited increase in computational effort. Using the so-called subgrid-based approach, high resolution information is used to solve the hydrodynamics and the sediment transport equation at coarse resolution. Moreover, the bed evolution equation is fully solved at high resolution. The coarse resolution ensures a limited computational cost, while the use of high resolution information is essential to preserve the accuracy. In this manuscript, the new method is derived and results of two examples are presented. These estuarine examples illustrate the abilities and the limitations of this subgrid-based approach.

4.1. Introduction

Numerical models that simulate sediment dynamics have proven to be indispensable for morphological studies in rivers, estuaries and coastal seas [71]. Deltas and estuaries such as the Wadden Sea, the Westerschelde, and the Yangtze estuary are morphodynamic systems of great ecological and economical value. Many estuaries are protected by international regulations like Natura 2000 (European collaboration to protect Europe's species and habitats [72]). Human interventions therefore, need careful considerations, including morphological changes [73]. Morphodynamic models need to simulate the hydrodynamics accurately, as well as sediment erosion,

This chapter will be published as Volp, van Prooijen, Pietrzak, and Stelling [70].

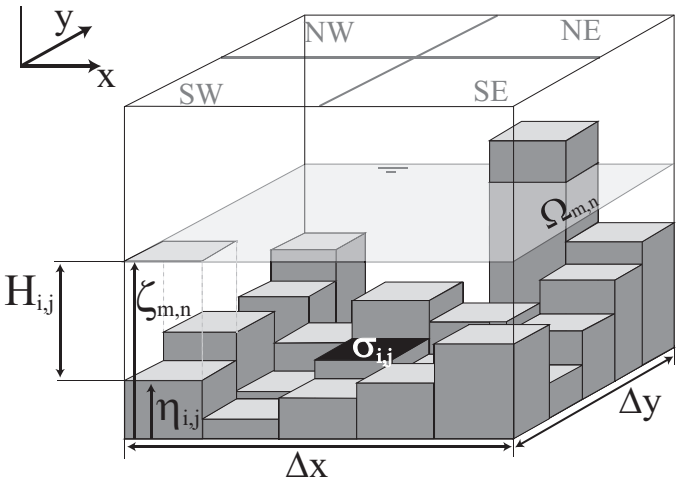

Figure 4.1: Overview of a coarse grid cell with an underlying subgrid. (Reprint from [35]). The bed update is performed on the high-resolution grid. Volumes and cross-sectional areas are determined using this high-resolution information and the computed variables at the coarse grid.

transport and deposition. This results in variations of the bathymetry and of the suspended sediment concentration (SSC). SSC is an important indicator for light attenuation, which is crucial for ecological primary production [74].

With increasing computer power significant advances in morphodynamic modelling have taken place [75]. Hibma (2004) [40] was one of the first to study numerically the formation of channel-shoal patterns over long periods of time (up to 300 years). Ever since, various long-term studies have been performed (e.g. [76] [77], [78]). Although the morphological response to changing conditions can be in the order of decades or even centuries, the forcing conditions change in the order of hours. Consequently, this multi-scale problem requires both long simulation periods to determine the morphodynamic response, and high frequency forcing. Moreover, bed forms that are much smaller than the model domain can have a significant effect on the full dynamics. Therefore, high resolution spatial and temporal simulations are required to accurately capture the dynamics of these type of systems. Unfortunately, the computational effort for morphodynamic simulations is substantial. Therefore, a trade-off should be made between spatial resolution, simulated period, accuracy, and number of scenario runs. A fundamentally new approach for morphodynamic modelling is here presented, that can support modellers struggling with the computational effort.

Although various methods are available to reduce the computational effort [36], the resolution of the grid (and hence the accuracy) remains limited. Recently, Volp et al. (2015) [35] presented a subgrid-based method that offers a new perspective on this issue. This method combined a subgrid-based hydrodynamic model with a high resolution morphodynamic model. However, the effects of suspended sediment transport were neglected.

An efficient and accurate approach that reduces the computational effort in hydrodynamic simulations is the subgrid-based method ([11, 16, 42, 67]). Subgrid-based methods, inspired by the approach of Casulli (2009) [16], combine two different grids. The subgrid contains information that is available at high resolution, for example bathymetry and roughness data. The computation of water levels and velocities is carried out on a coarse resolution grid. However, for the computation of various variables, for example cell volumes, cross-sectional areas, and friction, the high- resolution information is taken into account. Figure 4.1 shows the two grids. The accuracy of the solution improves significantly, with a limited increase in computational effort. Moreover, such a subgrid-based method allows for an elegant flooding and drying algorithm, which is important for applicability in estuarine environments.

For the subgrid-based approach for morphodynamic modelling presented by Volp et al. (2015) [35], the hydrodynamic forcing is computed on a coarse grid using a subgrid-based approach [11]. The bed level updates are computed on the high-resolution subgrid. The main shortcoming of this morphodynamic model, is the assumption that sediment transport is proportional to flow velocity. This assumption is valid for pure bed load transport or for (almost) stationary flows, where the suspended sediment concentration equals the equilibrium concentration. However, in tidal systems this assumption is not always valid. Spatial and temporal lags lead to a difference between the actual concentration and the equilibrium concentration. Resolving the transport equation with an exchange term between water and bed is required. A proper simulation of the lag effects will lead to a better prediction of the instantaneous sediment concentration. This can be used for studies on primary production, but it will also lead to better estimates of the net sediment fluxes through, for example, tidal inlets the Wadden Sea. To estimate SSC, the sediment transport equation (or sediment balance equation) must be solved. Following traditional methods (e.g., [52]), this can be done at the same resolution as the bed evolution equation (i.e., on the high-resolution subgrid scale). However, typical time scales for the sediment transport equation are on the same order of those of the hydrodynamic system. Numerically, time-step restriction depends on the grid size, the celerity and the velocity. To guarantee that the time-step restriction for solving the full numerical system does not increase, it is favourable to solve the sediment equation on the same grid as the hydrodynamic system. Therefore, we developed a subgrid method for solving the sediment transport equation on the coarse grid, while taking high resolution effects into account. Crucial is the treatment of the sediment exchange terms between the water column and the bed. These terms are used in the sediment transport equation, but also in the bed evolution equation, which is solved at high resolution. Erosion rates can be computed directly at high resolution, but for an accurate solution, high-resolution effects are also needed to define the deposition rates.

The paper is structured as follows. The hydrodynamic and the morphodynamic systems are introduced in Section 4.2. The discretisation of the hydrodynamic part of the model is briefly explained in Section 4.3.1. The sediment transport equation and the equation for bed evolution are derived at the different grid resolutions in

Section 4.3.2. It is important to note the coupling between these equations, as this is key to the method. The results of two examples are presented in Section 4.4. The examples are chosen to illustrate the functioning of the presented approach. The first example describes the flow through a creek in a tidal flat. This example highlights the advantages and the limitations of the method for the transport equation as presented here. The second example considers the morphological development of an estuary starting with a uniformly sloping bed level. For this example we simulate the morphodynamic development over eighty years. A discussion and concluding remarks are given in Section 4.5.

4.2. Governing equations

A three-dimensional model is needed to describe the transport of (fine) sediments. This is especially the case for areas where baroclinic processes play a key role, as in river plumes [79]. However, two-dimensional, depth-averaged models are still commonly used to simulate sediment dynamics ([80], [69], [81], [82]), as these models are significantly faster and give reasonable to good results. Therefore, we restrict ourselves to the two-dimensional space.

The flow is described by the depth-averaged, two-dimensional shallow water equations. The bed evolution is described by a mass balance of all sediment fluxes. The total sediment transport is split into a bed load and a suspended load components. The behaviour of suspended load in such a depth-averaged model can be described by a transport equation, as was initially derived by [55]. The net erosion or deposition of sediments depends on the ratio between the concentration and an equilibrium concentration. The bed load transport can be computed using various empirical relations based on bed shear stress, given by, for example, [83–85].

The set of equations is composed of the shallow-water equations, the transport equation, and the bed evolution equation (sediment mass conservation equation):

$$\frac{\partial u}{\partial t} + u\frac{\partial u}{\partial x} + u\frac{\partial u}{\partial y} = -g\frac{\partial \zeta}{\partial x} - \frac{c_f}{H}u||\vec{u}|| \tag{4.1}$$

$$\frac{\partial v}{\partial t} + u\frac{\partial v}{\partial x} + v\frac{\partial v}{\partial y} = -g\frac{\partial \zeta}{\partial y} - \frac{c_f}{H}v||\vec{u}|| \tag{4.2}$$

$$\frac{\partial H}{\partial t} + \frac{\partial (uH)}{\partial x} + \frac{\partial (vH)}{\partial y} = 0 \tag{4.3}$$

$$\frac{\partial (cH)}{\partial t} + \frac{\partial (cuH)}{\partial x} + \frac{\partial (cvH)}{\partial y} = \frac{H\left(c_{eq} - c\right)}{T} \tag{4.4}$$

$$\begin{aligned}(1-p)\frac{1}{\mathrm{M}}\frac{\partial \eta}{\partial t} + \frac{\partial q_b^x}{\partial x} + \frac{\partial q_b^y}{\partial y} &= -\frac{H\left(c_{eq} - c\right)}{T} + \dots \\ \dots + \left[\frac{\partial}{\partial x}\left(\epsilon_x \frac{\partial \eta}{\partial x}\right) + \frac{\partial}{\partial y}\left(\epsilon_y \frac{\partial \eta}{\partial y}\right)\right] &\end{aligned} \tag{4.5}$$

where $\vec{u} = (u, v)$ is the depth-averaged velocity in x- and y-direction and $||\vec{u}|| = \sqrt{u^2 + v^2}$. The water level ζ and the bed level η, form the water depth $H = \zeta - \eta$. g represents gravitational acceleration. The viscous and Coriolis terms are neglected

for simplicity, although they can be included, c is the instantaneous, dimensionless concentration. The equilibrium concentration, c_{eq}, represents the situation where the erosion and deposition fluxes are equal. In this case, the definition for c_{eq} by [86] is used. The time scale to adapt to the equilibrium concentration is represented by T, the Galappatti time scale [55]. This timescale depends on sediment distribution over the water column and the fall velocity. Here, we adopt the expression $T = \alpha \frac{H}{w_s}$, where α represents the vertical profile of the concentration. In this paper, we apply $\alpha = \frac{1}{3}$. However, other algebraic expressions for α, can easily be implemented.

The bed porosity, p, is considered constant and uniform. Bed load transport is represented by $\vec{q_b} = (q_b^x, q_b^y)$. There are various formulations in use to describe bed load transport. Here we use the formulation by [87]. Independently of the chosen formulation, the bed load transport can be affected by the local bed slope. The same relation is used as is presented by [35], which is based on the descriptions of [52] [88] [58]. The last term of equation (4.5) is a diffusion term, which can be scaled, or switched off by setting the diffusion parameter. This method for diffusion is similar to that proposed by [51], in which $\vec{\epsilon} = (\epsilon_x, \epsilon_y)$ is defined as: $\epsilon_x = \tilde{\epsilon} \frac{|q_b^y|}{||q_b||}$, $\epsilon_y = \tilde{\epsilon} \frac{|q_b^x|}{||q_b||}$. $\tilde{\epsilon}$ is a dimensionless scaling factor for diffusion. The described method allows the use of a morphological factor, M, [36] to speed up morphological simulations. Equations (4.1)-(4.5) form the basis of the numerical model.

4.3. Discretisation

To extend the morphodynamic model, with the new approach for suspended sediment, a good understanding of the hydrodynamic method in combination with the high resolution morphodynamic method is crucial. Therefore, the key elements of both methods ([11], [35]) are briefly described here. Subgrid-based methods use two grids with different resolutions. On the (coarse) computational grid, water levels and velocities are computed. The bathymetry and roughness information is defined on the subgrid. The subgrid is a grid with a (much) higher resolution than the computational grid. The water level is assumed to be uniform in a computational cell. However, the bathymetry within that domain is allowed to vary, which means that the wet domain within a computational cell can vary.

The coarse grid is a Cartesian, structured, staggered grid, where water levels and concentration values are defined in the cell centres and velocities at the cell edges (Figure 4.2). The high-resolution bed grid or subgrid is also a structured grid, where all variables (including velocities) are defined in the cell centres. The discrete variables that are defined on the coarse grid have indices m, n, where m ($1 \geq m \geq M$) appoints the cells in the x direction and n ($1 \geq n \geq N$) those in the y direction. Similarly, variables defined on the bed grid (subgrid) have indices i, j ($1 \geq i \geq I$, $1 \geq j \geq J$). The cardinal directions are used to appoint the edges and sub-domains within momentum and water-level domains, c.q. North (N), East (E), South (S) and West (W). Specific locations and definitions of the grid used during the derivation are explained in Figure 4.2.

A finite volume approach is chosen for the discretisation of equations (4.1)-(4.5). Therefore, the equations will be integrated over a cell domain. Three different cell

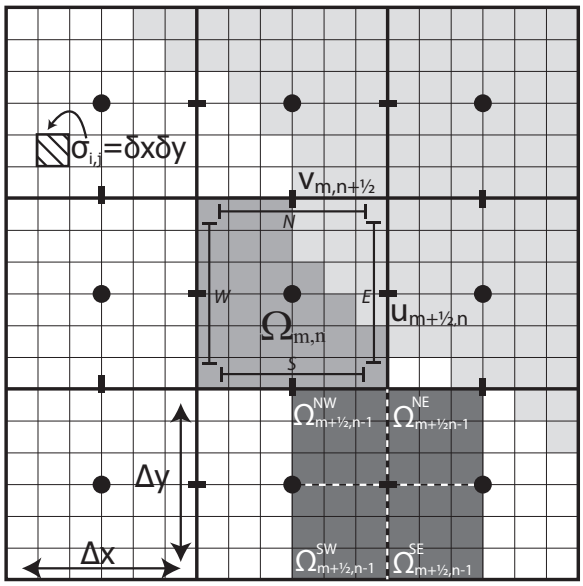

Figure 4.2: Overview of the grid including definitions for the derivation in Section 4.3.2. As an example, the light grey area in the cells is dry. Therefore, the size of Ω is just the dark grey area, while it could be maximally $\Delta x \Delta y$. The coarse grid is the hydrodynamic grid, with water levels in the cell centres (dots) and velocities at the cell faces (dashes).

domains can be defined. The first domain is for coarse-grid variables defined at cell centres: $\Omega_{m,n}$, which is the wet part of a coarse-grid cell. The size of domain $\Omega_{m,n}$ can change in time and varies between zero and the full area of the grid cell ($\Delta x \Delta y$). The second domain is for coarse-grid variables defined on the edges of a cell, the domain is shifted half a cell to form a momentum domain: $D = \Omega_{m+\frac{1}{2},n}$ and $D = \Omega_{m,n+\frac{1}{2}}$ for the velocities in x and y direction, respectively. The third domain is for variables defined on the high-resolution bed grid like bathymetry and roughness: $D = P_{i,j}$. This domain, $P_{i,j}$, corresponds to a wet pixel with a surface area of $\sigma_{i,j}$. For an overview of the domains, see Figure 4.2. A pixel is wet if: $H(x,y,t) = \zeta(x,y,t) - \eta(x,y,t) > 0$.

To discretize the governing equations, the set of equations is integrated over the designated domains. Therefore, piece-wise discontinuous functions are defined based on the discrete variables using a step function, the so-called indicator function ([11]):

$$\Upsilon_D = \begin{cases} 1 & (x,y) \in D \\ 0 & (x,y) \notin D \end{cases} \tag{4.6}$$

The domain D is different for variables defined in cell centres, at edges and for the variables defined on the coarse grid, the subgrid and the bed grid. As an example, the piece-wise discontinuous water level, bed level and depth-averaged velocities in,

x and y directions (u, v) at coarse and high resolution are defined, respectively as:

$$\zeta(x,y,t) = \sum_{m=1}^{M}\sum_{n=1}^{N} \zeta_{m,n}\Upsilon_{\Omega_{m,n}} \qquad \eta(x,y,t) = \sum_{i=1}^{I}\sum_{j=1}^{J} \eta_{i,j}\Upsilon_{P_{i,j}}$$

$$u(x,y,t) = \sum_{m=0}^{M-1}\sum_{n=0}^{N-1} u_{m+\frac{1}{2},n}\Upsilon_{\Omega_{m+\frac{1}{2},n}} \qquad v(x,y,t) = \sum_{m=0}^{M-1}\sum_{n=0}^{N-1} v_{m,n+\frac{1}{2}}\Upsilon_{\Omega_{m,n+\frac{1}{2}}}$$

$$u_p(x,y,t) = \sum_{i=1}^{I}\sum_{j=1}^{J} u_{p:i,j}\Upsilon_{P_{i,j}} \qquad v_p(x,y,t) = \sum_{i=1}^{I}\sum_{j=1}^{J} v_{p:i,j}\Upsilon_{P_{i,j}}$$

All variables of equations (4.1)-(4.5) are redefined using indicator function. Similar definitions are also applied to the other variables. Using these discontinuous variables, the governing equations (4.1)-(4.5) are discretised in the following sections.

4.3.1. Hydrodynamic Model

The hydrodynamic equations are discretized using a finite volume approach as presented by [11]. The rationale to use two different grids is that generally the water level varies much more gradually than the bed, while it is essential for an accurate solution to capture the bathymetry accurately. Within a computational cell, the water level is assumed to be uniform and the bed level is allowed to vary. Cell volumes and cross-sections are based on information from both grids. The cell volume (V_Ω) is defined as the surface integral over the depth within a domain Ω.

$$V_\Omega = \iint_\Omega H \, d\Omega \qquad \Omega \in \Omega_{m,n} \tag{4.7}$$

Note that the domain Ω is the wet area within a cell and therefore can vary in time. The cross-sectional area of a cell ($A_{\Omega:l}$, l = E, W, N, S) is the depth-integrated area over the cell edge. As example, the cross-section on the east (E) side of the cell is:

$$A_{\Omega:\mathrm{E}} = \int_{\Omega^{\mathrm{E}}} H \, dy_\Omega \qquad \Omega \in \Omega_{m,n} \tag{4.8}$$

This implies that a cell and its cross-sections can be wet, partly wet, or dry (Figure 4.2). In this way the volume becomes a non-linear function of the water level, which can be solved by applying Newton iteration [16]. Moreover, in this way flooding and drying can be taken into account naturally as a volume is always larger than or equal to zero.

Integrating equations (4.1) and (4.2) over a momentum domain and equation (4.3)

over a water level domain, the hydrodynamic equations, because:

$$\frac{V_{m,n}^{k+1} - V_{m,n}^{k}}{\Delta t} + u_{m+\frac{1}{2},n}^{k+\theta} A_{s_{m,n}^{\mathrm{E}}}^{k} - u_{m-\frac{1}{2},n}^{k+\theta} A_{s_{m,n}^{\mathrm{W}}}^{k} + v_{m,n+\frac{1}{2}}^{k+\theta} A_{s_{m,n}^{\mathrm{N}}}^{k} - v_{m,n-\frac{1}{2}}^{k+\theta} A_{s_{m,n}^{\mathrm{S}}}^{k} = 0 \tag{4.9}$$

$$\frac{u_{m+\frac{1}{2},n}^{k+1} - u_{m+\frac{1}{2},n}^{k}}{\Delta t} + adv(u^k) + g\frac{\zeta_{m+1,n}^{k+\theta} - \zeta_{m,n}^{k+\theta}}{\Delta x} + B_f(u^k, v^k, u^{k+1}) = 0 \tag{4.10}$$

$$\frac{v_{m,n+\frac{1}{2}}^{k+1} - v_{m,n+\frac{1}{2}}^{k}}{\Delta t} + adv(v^k) + g\frac{\zeta_{m,n+1}^{k+\theta} - \zeta_{m,n}^{k+\theta}}{\Delta y} + B_f(u^k, v^k, v^{k+1}) = 0 \tag{4.11}$$

The time integration variables k+θ are defined according to the θ-method by:

$$f^{k+\theta} = (1-\theta)f^k + \theta f^{k+1}$$

The terms adv and B_f are the advection and bed friction terms. In deriving these terms, high-resolution effects are taken into account. More details about the hydrodynamic model can be found in the work of [11]. The model computes water levels and velocities at coarse resolution. Using a physics-based interpolation method, the coarse-grid variables are interpolated to the high-resolution grid. These high-resolution variables are also used to drive the morphodynamic system [35].

4.3.2. Morphodynamic Model

The bed evolution equation and the suspended sediment transport equation share the erosion and deposition terms. For efficiency reasons, the bed evolution equation will be solved on the high-resolution bed grid and the sediment transport equation on the coarse grid. For that, it is essential to find a mass conserving connection between the two. In the next sections, the suspended sediment transport equation is integrated over the domain of a coarse-grid cell and the bed evolution equation over the domain of a bed grid cell.

Sediment Transport Equation

The hydrodynamic solution improved significantly by taking high-resolution information into account. Aiming for the same advantages, the discretization of the sediment transport equation is performed using a similar approach. Therefore, equation (4.4) is integrated over a domain Ω, which is centred around a water level/concentration point.

For the integration of the first term, the order of integration and differentiation is changed. The corresponding Leibnitz terms are zero, which allows one to write:

$$\iint_{\Omega} \frac{\partial (cH)}{\partial t}\, d\Omega = \frac{\partial}{\partial t} \iint_{\Omega} cH\, d\Omega = \frac{\partial (c_\Omega V_\Omega)}{\partial t} \qquad \Omega \in \Omega_{m,n} \tag{4.12}$$

for which a cell averaged concentration is defined as:

$$c_\Omega \equiv \frac{1}{V_\Omega} \iint_{\Omega} cH\, d\Omega \qquad \Omega \in \Omega_{m,n}, \tag{4.13}$$

in which V_Ω is the total water volume in the computational cell (equation (4.7)).

The integration procedure for the advective terms with derivatives in x- and y-direction of the sediment transport equation is similar. Therefore, only the integration of the second term of equation 4.4 is given in detail. Integration over the width (in x-direction) of the second term results in:

$$\iint_\Omega \frac{\partial (cuH)}{\partial x}\, d\Omega = \int_{dy} [cuH]_{\Omega:\mathrm{E}} - [cuH]_{\Omega:\mathrm{W}}\; dy \tag{4.14}$$

The concentration is defined in the centre of a cell, to determine the concentration at the cell edge a first order upwind method is applied. Assuming the volume averaged concentration to be uniform over the cell edge:

$$\int_{dy} [c^* uH]_{\Omega:\mathrm{E}} - [c^* uH]_{\Omega:\mathrm{W}} = Q^x_{\Omega:E} c^*_{\Omega:\mathrm{E}} - Q^x_{\Omega:W} c^*_{\Omega:\mathrm{W}} \tag{4.15}$$

where c^* is the upwind concentration based on the direction of the discharge and the discharge defined as:

$$Q^x_{\Omega:\mathrm{W}} = \int_{\Omega:\mathrm{W}} uH \quad dy_{\Omega:\mathrm{W}} \tag{4.16}$$

The next step is to decompose the time derivative (Equation (4.12)). After which, the hydrodynamic mass conservation equation can be substituted, similar to the procedure used by [11]. Consequently, the downstream terms cancel out, which results in:

$$\begin{aligned} V_\Omega \frac{\partial c_\Omega}{\partial t} + c_\Omega \frac{\partial V_\Omega}{\partial t} + Q^x_{\Omega:\mathrm{E}} c^*_{\Omega:\mathrm{E}} - Q^x_{\Omega:\mathrm{W}} c^*_{\Omega:\mathrm{W}} + Q^y_{\Omega:\mathrm{N}} c^*_{\Omega:\mathrm{N}} - Q^y_{\Omega:\mathrm{S}} c^*_{\Omega:\mathrm{S}} \\ = V_\Omega \frac{\partial c_\Omega}{\partial t} + max\left[0, Q^x_{\Omega:\mathrm{W}}\right](c_{m,n} - c_{m-1,n}) + \dots \\ + min\left[0, Q^x_{\Omega:\mathrm{E}}\right](c_{m+1,n} - c_{m,n}) + \dots \\ + max\left[0, Q^y_{\Omega:\mathrm{S}}\right](c_{m,n} - c_{m,n-1}) + \dots \\ + min\left[0, Q^y_{\Omega:\mathrm{N}}\right](c_{m,n+1} - c_{m,n}) \end{aligned} \tag{4.17}$$

The interpolated high-resolution water level and velocity results allow the equilibrium concentration and the Galappatti time scale to be defined on the high-resolution grid and to vary at this scale. In principle, also the sediment composition could vary at this resolution, but for simplicity only one sediment fraction is taken into account. To make use of the high-resolution information, the concentration within a coarse computational cell can be non-uniformly distributed. To define the variation, a relation between the volume-averaged concentration and the local concentration is required. The concentration depends, however, not only on local processes. Due to spatial and temporal lag effects, the concentration will deviate from the equilibrium concentration. The spatial lag depends on the adjustment length $L = \frac{uH}{w_s}$ and the horizontal scale of the bed level variation. In case the length scale L is larger than the coarse grid, the spatial lag will automatically be

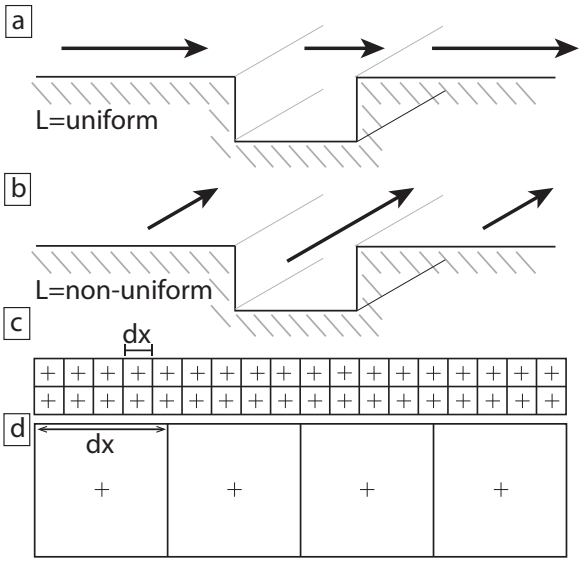

Figure 4.3: Two idealised, extreme situations for local variations in the bed and two grids with different resolution. a) the main flow crosses a small channel. b) the main flow is parallel to a small channel. c) Compared to bed features, a fine resolution grid, and d) a coarse resolution grid.

resolved by the model. When the length scale L is varies within a coarse-grid cell, this effect needs to be estimated (Figure 4.3). To make this estimation we identify two idealized flow cases. We consider a uniform bed with a channel cutting through (Figure 4.3.a). The width of the channel is small compared to the length scale L. If the flow is perpendicular to the channel, the concentration has no space to adapt to its new equilibrium concentration and the best estimate for the concentration in the channel is the equilibrium concentration outside the channel. In this idealized flow case, the adjustment length does not change in space, as $uH = q$ (q the discharge). Meaning, even though the bed level changes, the adjustment length remains the same within a cell. The second case is when the flow is in the direction of the channel (Figure 4.3.b). Now, the width of the channel is not the relevant length scale any more. In that case the equilibrium concentration in the channel is the best estimate for the concentration in the channel. Two different adjustment lengths can be defined, one inside and another outside the channel. The effect of this variation can accumulate over various cells. Therefore, such variation can affect the concentration at large scales.

We can then identify two estimates for the subgrid concentration in steady-state flow. First, the subgrid concentration is equal to the coarse-grid equilibrium concentration. This is the trivial concentration. Second, the concentration is equal to the subgrid equilibrium concentration. These two estimates can be extended to situations for unsteady flow, including temporal lag effects. In case of the first estimate, the subgrid concentration is simply the coarse-grid concentration. In the case of the second estimate, we need to estimate the local temporal lag effects. For

simplicity, however, we assume that the subgrid concentration scales linearly with the coarse-grid concentration.

To write this in mathematical terms, the relation between the cell-averaged concentration and the concentration at high resolution is linear:

$$\beta = \frac{c_\Omega}{c} \tag{4.18}$$

β determines the distribution within a cell. The trivial choice would be to set:

$$\beta_I = 1 \tag{4.19}$$

which implies a uniform distribution of the concentration. To define β_{II} based on the second assumption, a similar approach was taken as in the work of [11]. According to analyses made by [55] and [89], for many applications the dominant balance of the equation is between erosion and deposition term. Most systems tend toward equilibrium. For shallow water environments, the formulation based on the equilibrium concentration was derived, for which the zeroth order solution is:

$$c = c_{eq} \tag{4.20}$$

Note, that the equilibrium concentration depends on variables, which are known on high resolution. The distribution of the concentration will be based on this zeroth order solution, for that reason the distribution is based on the equilibrium concentration.

$$\frac{c}{c_{eq}} = uniform \tag{4.21}$$

When this assumption and the definition for the volume averaged concentration (4.13) are substituted in to equation (4.18), β_{II} is:

$$\beta_{II} = \frac{\frac{c_{eq}}{c}\iint_\Omega cH\, d\Omega}{c_{eq}\iint_\Omega H\, d\Omega} = \frac{\iint_\Omega c_{eq}H\, d\Omega}{c_{eq}V_\Omega} \tag{4.22}$$

The factor β is substituted in the final term of the transport equation (4.4):

$$\begin{aligned}
\iint_\Omega \frac{H\,(c_{eq}-c)}{T} d\Omega \qquad &= \qquad \iint_\Omega \frac{H\left(c_{eq}-\frac{c_\Omega}{\beta}\right)}{T} d\Omega \\
\beta_I\text{:} \qquad &\Rightarrow \qquad \iint_\Omega \frac{Hc_{eq}}{T}\, d\Omega - c_\Omega \iint_\Omega \frac{H}{T}\, d\Omega \\
\beta_{II}\text{:} \qquad &\Rightarrow \qquad \iint_\Omega \frac{Hc_{eq}}{T}\, d\Omega \left(1 - \frac{V_\Omega c_\Omega}{\iint_\Omega c_{eq}H\, d\Omega}\right)
\end{aligned}$$

Note, that the term depending on the equilibrium concentration (the erosion term) is the same for both assumptions. However, in the expression based on β_{II}, the term depending on the concentration (the deposition part) scales with the equilibrium concentration, which is defined on the bed grid.

Finally, collecting terms of the suspended sediment transport equation, it becomes in full discretized form:

$$
\begin{aligned}
V_{m,n}^{k+1}\frac{c_{m,n}^{k+1}-c_{m,n}^{k}}{\Delta t} &+max\left[0,Q_{m-\frac{1}{2},n}^{x:k+1}\right]\left(c_{m,n}^{k+\theta}-c_{m-1,n}^{k+\theta}\right) \\
&+min\left[0,Q_{m+\frac{1}{2},n}^{x:k+1}\right]\left(c_{m+1,n}^{k+\theta}-c_{m,n}^{k+\theta}\right) \\
&+max\left[0,Q_{m,n-\frac{1}{2}}^{y:k+1}\right]\left(c_{m,n}^{k+\theta}-c_{m,n-1}^{k+\theta}\right) \\
&+min\left[0,Q_{m,n+\frac{1}{2}}^{y:k+1}\right]\left(c_{m,n+1}^{k+\theta}-c_{m,n}^{k+\theta}\right)=\ldots \\
\beta_I\text{:}\quad \Rightarrow\quad \cdots &= \sum_{i_0}^{i_1}\sum_{j_0}^{j_1}\frac{H_{i,j}^{k+1}c_{eq:i,j}^{k+1}}{T_{i,j}^{k+1}}\delta x\delta y - c_{m,n}^{k+1}\sum_{i_0}^{i_1}\sum_{j_0}^{j_1}\frac{H_{i,j}^{k+1}}{T_{i,j}^{k+1}}\delta x\delta y \\
\beta_{II}\text{:}\quad \Rightarrow\quad \cdots &= \sum_{i_0}^{i_1}\sum_{j_0}^{j_1}\frac{H_{i,j}^{k+1}c_{eq:i,j}^{k+1}}{T_{i,j}^{k+1}}\delta x\delta y\left(1-\frac{V_{m,n}^{k+1}c_{m,n}^{k+1}}{\sum_{i_0}^{i_1}\sum_{j_0}^{j_1}H_{i,j}^{k+1}c_{eq:i,j}^{k+1}\delta x\delta y}\right)
\end{aligned}
\tag{4.23}
$$

in which the advective terms are taken into account explicitly and the deposition (sink) term implicitly. However, the time discretisation of the advective terms can be chosen differently. The hydrodynamic variables and those which are based on these, such as the equilibrium concentration, are updated variables, and known whilst evaluating the sediment transport equation.

Bed Evolution Equation

The bed evolution equation is discretized by integrating it over the domain of a bed grid cell:

$$
\iint_{\sigma}(1-p)\frac{\partial\eta}{\partial t}+\frac{\partial q_b^x}{\partial x}+\frac{\partial q_b^y}{\partial y}\,d\sigma=-\iint_{\sigma}\frac{H}{T}(c_{eq}-c)\,d\sigma \qquad \sigma\in\sigma_{i,j} \tag{4.24}
$$

Based on the interpolated velocities, the bed load transport is computed at the centre of a bed grid cell. The first three terms of equation (4.24) become, after integration and in discretized form, respectively:

$$
\begin{aligned}
&(1-p)\,\tfrac{\partial\eta_\sigma}{\partial t}+\tfrac{q_b^x|_{x_b}-q_b^x|_{x_a}}{\delta x}+\tfrac{q_b^y|_{y_b}-q_b^y|_{y_a}}{\delta y} \qquad \Rightarrow \\
&(1-p)\,\tfrac{\eta_{i,j}^{n+1}-\eta_{i,j}^{n}}{\Delta t}+\tfrac{\tilde{q}_{b:i,j}^x-\tilde{q}_{b:i,j}^x}{\delta x}+\tfrac{\tilde{q}_{b:i,j}^y-\tilde{q}_{b:i,j}^y}{\delta y}
\end{aligned}
$$

δx and δy are the dimensions of a bed grid cell. The fluxes ($\tilde{q}_b^x$, $\tilde{q}_b^y$) at the cell edges are determined using a first order upwind method. A more elaborate discussion of the upwind method is given in the next section.

To guarantee conservation of mass, the erosion and deposition terms of the bed evolution equation and the concentration equation need to be exactly equal when integrated over a domain Ω. Therefore, the same assumptions defined in equations (4.18), (4.19) and (4.22) are substituted in the final term of the bed evolution

equation (4.24):

$$-\iint_\sigma \frac{H}{T}(c_{eq}-c)\,d\sigma = -\iint_\sigma \frac{H}{T}(c_{eq}-\frac{c_\Omega}{\beta})\,d\sigma \qquad \text{for} \quad \sigma \in \Omega \tag{4.25}$$

$$\beta_I\text{: } \Rightarrow \qquad \ldots = -\frac{H}{T}\left(c_{eq}-c_\Omega\right)$$

$$\beta_{II}\text{: } \Rightarrow \qquad \ldots = -\frac{Hc_{eq}}{T}\left(1-\frac{V_\Omega c_\Omega}{\iint_\Omega c_{eq}H\,d\Omega}\right)$$

The final form of the bed evolution equation in full discretized form is:

$$\frac{\eta_{i,j}^{k+1}-\eta_{i,j}^{n}}{\Delta t}+\frac{\tilde{q}_{b:i+\frac{1}{2},j}^{x*}-\tilde{q}_{b:i+\frac{1}{2},j}^{x*}}{\delta x}+\frac{\tilde{q}_{b:i,j-\frac{1}{2}}^{y*}-\tilde{q}_{b:i,j+\frac{1}{2}}^{y*}}{\delta y}=\ldots \tag{4.26}$$

$$\beta_I\text{: } \Rightarrow \quad \cdots = -\frac{H_{i,j}^{k+1}}{T_{i,j}^{k+1}}\left(c_{eq:i,j}^{k+1}-c_\Omega^{k+1}\right)$$

$$\beta_{II}\text{: } \Rightarrow \quad \cdots = -\frac{H_{i,j}^{k+1}c_{eq:i,j}^{k+1}}{T_{i,j}^{k+1}}\left(\frac{V_{m,n}^{k+1}c_{m,n}^{k+1}}{1-\iint_\Omega c_{eq:i,j}^{k+1}H^{k+1}\,d\Omega}\right)$$

It remains to determine the upwind direction for bed load transport. [37] give an overview of possible discretisation schemes and their implications for accuracy and stability. [35] explain that to enhance stability, the upwind direction was chosen based on the direction of the bed celerity instead of the direction of the flow. However, by including lag effects, the bed celerity changed. To determine the full bed celerity, an analysis is made for the full morphodynamic system. Initial steps for this method were performed by [59]. The summation of equations (4.4) and (4.5) results in:

$$(1-p)\frac{\partial \eta}{\partial t}+\frac{\partial cH}{\partial t}+\frac{\partial}{\partial x}\left(q_b^x+cHu\right)+\frac{\partial}{\partial y}\left(q_b^y+cHv\right)=0 \tag{4.27}$$

By introducing $\chi=(1-p)\eta+cH$, $q_T^x=q_b^x+cHu$ and $q_T^y=q_b^y+cHv$, equation (4.27) can be rewritten as:

$$\frac{\partial \chi}{\partial t}+\frac{\partial q_T^x}{\partial x}+\frac{\partial q_T^y}{\partial y}=\frac{\partial \chi}{\partial t}+\boldsymbol{\frac{\partial q_T^x}{\partial \chi}}\frac{\partial \chi}{\partial x}+\boldsymbol{\frac{\partial q_T^y}{\partial \chi}}\frac{\partial \chi}{\partial y}=0 \tag{4.28}$$

This is a full advective equation, similar to the Exner equation without the erosion and deposition terms. The bold printed terms represent the characteristic velocity or the bed celerity (λ) of the morphodynamic system, which predicts the direction of evolution. It is very difficult to determine the bed celerity analytically. Especially in practical applications, where the bathymetry is not defined by a simple mathematical function. However, the bed celerity can be defined in most cases numerically, for example in the x-direction by:

$$\lambda_{i+\frac{1}{2},j}=\frac{q_{T:i+1,j}^x-q_{T:i,j}^x}{\chi_{i+1,j}-\chi_{i,j}}=\frac{q_{b:i+1,j}^x+c_{i+1,j}H_{i+1,j}u_{i+1,j}-q_{b:i,j}^x-c_{i,j}H_{i,j}u_{i,j}}{(1-p)\eta_{i+1,j}+c_{i+1,j}H_{i+1,j}-(1-p)\eta_{i,j}-c_{i,j}H_{i,j}} \tag{4.29}$$

Although, the concentration is not defined on the high resolution grid, it can be estimated from the coarse-grid concentration, using the factor β (4.19 or 4.22).

$$\lambda_{i+\frac{1}{2},j} = \frac{q^x_{b:i+1,j} + \frac{c_{\Omega:i+1,j}}{\beta_{\Omega:i+1,j}} H_{i+1,j} u_{i+1,j} - q^x_{b:i,j} - \frac{c_{\Omega:i,j}}{\beta_{\Omega:i,j}} H_{i,j} u_{i,j}}{(1-p)\eta_{i+1,j} + \frac{c_{\Omega:i+1,j}}{\beta_{\Omega:i+1,j}} H_{i+1,j} - (1-p)\eta_{i,j} - \frac{c_{\Omega:i,j}}{\beta_{\Omega:i,j}} H_{i,j}} \tag{4.30}$$

$\Omega : i,j = \Omega_{m,n}$ for $i,j \in \Omega_{m,n}$. Celerity is determined as long as the denominator is not equal to zero. In that case, the direction of the net transport (the numerator) is leading. Based on λ, the fluxes at the cell faces can be determined, in the x-direction:

$$\tilde{q}^{x*}_{b:i+\frac{1}{2},j} = q^{x:k+1}_{b:i,j} \qquad \text{for} \qquad \lambda_{i+\frac{1}{2},j} \geq 0$$
$$\tilde{q}^{x*}_{b:i+\frac{1}{2},j} = q^{x:k+1}_{b:i+1,j} \qquad \text{for} \qquad \lambda_{i+\frac{1}{2},j} < 0$$

This can also be applied to a second order upwind method.

4.4. Examples

We will present two examples to show the performance of various aspects of the method. The first example is a creek cutting through a tidal flat, which can typically be found on flats in the Westerschelde, the Netherlands. A simplified geometry is used to show specifically the effects of the assumptions made in the derivation of the method and to show the correct numerical implementation. The second example is the development of a channel-shoal system in a tidal basin. As one of the first Hibma (2004) [68] studied the formation of channel-shoal patterns over long periods of time using a process-based model. They showed how morphological instabilities grow and provided insight into the time scales at which equilibrium is reached, which can be on time scales of centuries. This example has been widely used to show that morphodynamic methods were able to successfully reproduce such a channel-shoal system. This example shows the ability of the model to initiate small scale morphological features on the subgrid scale. The dimensions of the model domain are at the scale of estuaries like the Westerschelde (the Netherlands). We simulate the morphological development for different grid sizes over a period of eighty years.

4.4.1. Creek through a tidal flat

The geometry of this example is designed based on the tidal flats of the *Land van Saeftinghe*. This is an extended tidal flat area found in the Westerschelde, which is an estuary at the border between Belgium and The Netherlands. The modelling domain consists of a creek and neighbouring tidal flats. The domain is 66 m wide and 300 m long. The creek is located along the centre line and is 6 m wide and the bed is 3 m below the base level of the flats (Figure 4.4.a).

This example shows the effect of (i) the inclusion of the subgrid; (ii) the resolution of the coarse grid and (iii) the effect of the choice between assuming the concentration to be uniform or non-uniform within a cell. Therefore, simulations for both assumptions, with and without subgrid are run for two different water levels and five different coarse-grid resolutions. The settings of these 26 simulations are shown in Table 4.1. Boundary conditions are required for the hydrodynamics, the

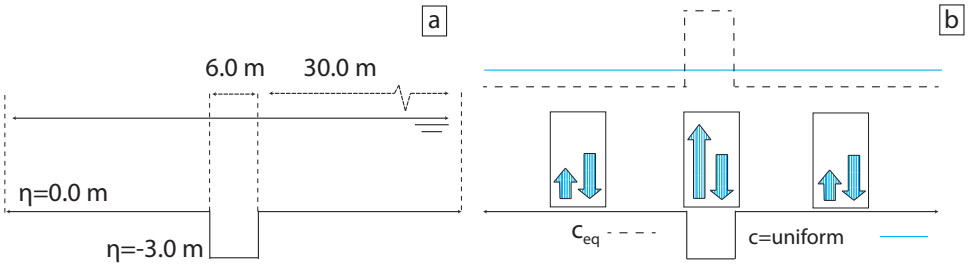

Figure 4.4: a) The geometry of the channel with flood plains. b) A schematic overview of the equilibrium concentration (dashed line) and the concentration using the $c = uniform$ approach (blue line). Arrows represent the erosion and deposition terms.

Table 4.1: An overview of model settings for the simulations of the creek in a tidal flat

Parameter	Value
Sediment formulation	van Rijn [86]
Median grain size D_{50}	$200 \cdot 10^{-6}$ m
Critical shear stress τ_c	0.155 $\frac{kg}{ms^2}$
Chézy coefficient	50 $m^{\frac{1}{2}}/s$
Computational grid resolution	1×1, 6×6, 11×11, 33×33, 66×66 m^2
ζ boundary condition	0.5, 1.0 m
Time-step	1 s

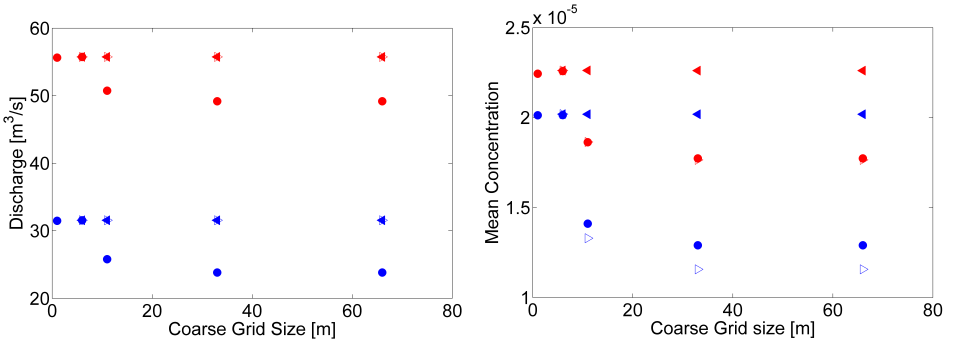

Figure 4.5: a) The total discharge as function of the coarse grid size computed for two different water levels ($\zeta = 0.5\ m$ is blue and $\zeta = 1.0\ m$ is red and for three different model settings (dots are no subgrid, open triangles are with a subgrid using approach I ($c = uniform$) and closed triangles are with a subgrid using approach II ($\frac{c}{c_{eq}} = uniform$). b) The concentration averaged over the full cross-section as function of the coarse grid size using the same symbols

concentration, and the bed. The inflow boundary condition uses a prescribed water level and the out flow boundary condition is a Neumann boundary. This boundary condition sets the water level gradient to its equilibrium. For the concentration, we set the inflow concentration to zero, because the equilibrium concentration depends on the flow conditions, which might be different, because of the differences in grid. This way it could be guaranteed that the incoming settings are the same. The bed slope is in equilibrium and is fixed during the simulations. This is because we are searching for equilibrium conditions for the hydrodynamics and the concentration. These are reached much faster than the morphodynamic time scale.

In Figure 4.5.a, the total discharge as a function of the coarse grid size is shown. Results of all simulations for the different water levels are shown for the systems in steady state. The results from the simulations that do not take the subgrid information into account are indicated with the circles and vary in colour for the different water levels (red and blue). As also shown by [11], the discharge is structurally underestimated, when the grid becomes coarser than the channel width. This deviation is approximately constant for the lower grid resolutions as the system does not capture the channel geometry at all. In other words, the average depth in a cell when no subgrid effects are taken into account, is barely affected by the narrow channel. Therefore, it cannot capture the dynamics any more, when the gird is larger than 12 m. The open and closed triangles are the computed discharges of the subgrid-based simulations. The discharges computed for the various coarse grid sizes are similar, thereby showing the proper implementation of the subgrid approach.

To compare the concentration results for all different resolutions, we consider the concentration averaged over a full cross section. In Figure 4.5.b, the average concentration as a function of the coarse-grid cell size is shown for the two different water levels (red and blue). The concentrations computed using the finest grid resolution ($dy = 6$ m) are accurate for all approaches. For this resolution, the

simple geometry of the creek and its dynamics can be fully captured for all grids and no extra assumptions are needed.

However, the results computed with the coarser grid resolutions differ significantly. Similar to Figure 4.5.a, the circles indicate the results from the simulations without the subgrid approaches. As soon as the coarse grid resolution is larger than the dimensions of the channel, the concentration drops. The decrease is even greater for the simulations based on the lower water levels, as the relative depth variation is larger. For the simulations with a coarser grid resolution, the discharge and the velocities are underestimated. Therefore, the amount of sediment in the water column is also underestimated. For the subgrid approach where the concentration is assumed to be uniform within a cell (open triangles), the concentration is increasingly underestimated for coarser grid resolutions and lower water levels. This is in contrast to the result from the simulations based on the assumption $\frac{c}{c_{eq}} = uniform$ (filled triangles). In that case, the concentration results are accurate even for the coarsest grid resolution.

The term depending on the equilibrium concentration is the same in both approaches, which can be seen in equation (4.23). This means that the erosion rate is the same for both approaches, because it depends on the local bed shear stresses only. The net sedimentation or erosion depends on the local balance between the concentration and the equilibrium concentration. In the creek, the concentration is higher than on the flats, due to the higher velocity. The equilibrium concentration scales non-linearly with the local velocity: $c_{eq} \propto u^n$. For the assumption of a non-uniform concentration, the width-averaged deposition rate can be estimated as: $\tilde{D}_{non-uniform} \propto w_s u^n_{flat} W_{flat}/W_{tot} + w_s u^n_{creek} W_{creek}/W_{tot}$, with W_{flat} the width of the flats, W_{creek} the width of the creek and W_{tot} the total width of the domain. For the assumption of a uniform concentration, the width-averaged deposition rate becomes: $\tilde{D}_{uniform} \propto w_s \tilde{u}^n$ with $\tilde{u}$ the width averaged velocity. It directly follows that for $n > 1$ we get: $\tilde{D}_{non-uniform} > \tilde{D}_{uniform}$. Due to the inconsistency of assuming a uniform concentration while having a varying flow and bed, it is impossible to obtain an equilibrium state within a computational cell. This is visualised in Figure 4.4.b. For this approach, there will always locally be a difference between the equilibrium concentration and the cell concentration. In this specific case, the result for the low water level of the $c = uniform$ approach is even worse for the concentration than computing it with a full coarse-grid approach. However, recall that the flow of the full coarse-grid approach is strongly underestimated. This implies that the total sediment suspended load is underestimated more than can be judged based on the concentrations only.

4.4.2. Idealized tidal basin

In this second example, the focus is on the long-term development of a tidal basin. Starting with a uniformly sloping bed, channels and shoals will evolve in time. Typically, the ebb and flood currents follow different paths. The first observations of this were already made by van Veen (1950) [90]. Ever since, various studies have been performed ranging from analytical models [71] to full numerical studies i.e. [40], [77], [76]. The computational effort for these long term simulations is high.

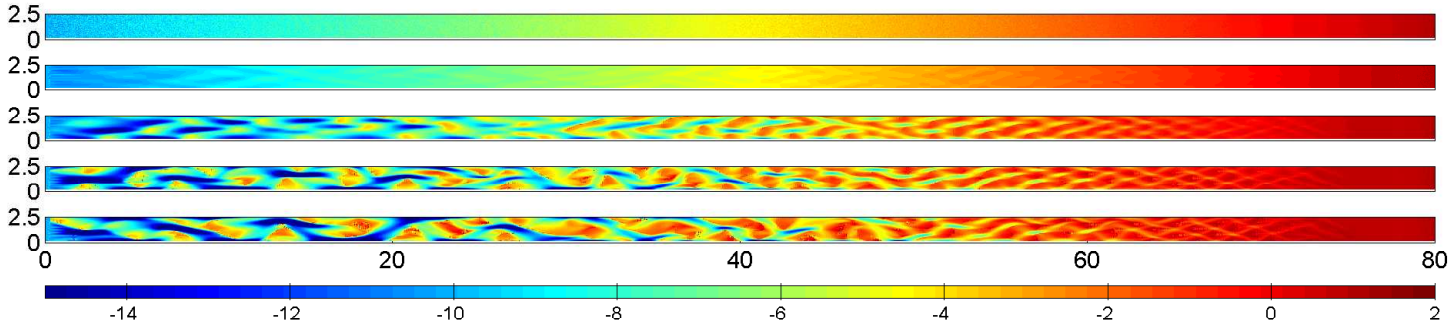

Figure 4.6: Bed evolution of simulation F. From top to bottom; The initial bed and the bed after approximately 20, 40, 60 and 80 years. The dimensions of the axis are in kilometres and the colorbar in metres.

Therefore, a subgrid approach could contribute to a more efficient study of these type of domains.

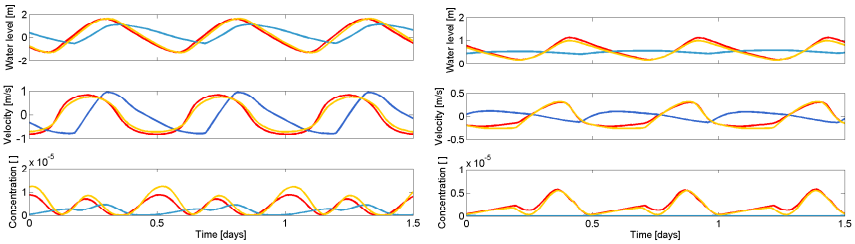

Figure 4.7: The variation in time for the water level, velocity, and concentration in deep (left panel) and shallow water (right panel). These are the results for the high-resolution simulation (A) yellow curve, and the results with (Simulation G: red curve) and without (Simulation C: blue curve) making use of the subgrid.

The main aim of this study is to present a subgrid-based method for suspended sediment in combination with the morphological evolution. It is important that a morphodynamic model is able to initiate morphological features. This implies that the method can initiate the correct instabilities and let them grow towards an equilibrium. Ultimately, when the channel-shoal system is developed, it is shown that the method can deal with a complex bathymetry and extensive flooding and drying. All these facets are illustrated by this example. Therefore, a series of simulations is performed, including runs for various grid sizes, with and without subgrid information.

The bathymetry in this example is similar to the bed used in other studies (e.g. [40], [39]). It has initially a uniformly sloping bed with random perturbations of maximally 5 % of the depth (see first frame of Figure 4.6). The bed level starts at MSL -10.0 m and increases linearly up to MSL 1.0 m at the end of the basin. A harmonic water-level boundary condition is imposed at the sea-side with period representing an M2 tide. This open boundary is both an inflow and an outflow boundary, depending on the tidal phase. The concentration at the boundary is set equal to the equilibrium concentration, when the boundary needs an incoming boundary condition. The outflow condition is based on the concentration in the first cell. The other boundaries are all closed. The sediment formulations used are based on the work of ([86, 87]) including a bed slope effect [39]. Specific details of the simulation settings are listed in Table 4.2.

The results of nine simulations are presented in this study. There is a high-resolution reference simulation (A) and in four steps the resolution of the computational grid is reduced. These simulations are performed with and without making use of the subgrid method. An overview of the nine simulations (A-I) is listed in Table 4.3. The subgrid-based simulations are only presented for the assumption that the ratio of the concentration and the equilibrium concentration is uniform (equation (4.22)). This is because the previous example shows much better results for this method. For some of the results there appears to be a mild growth of erratic numerical modes of scales of $2\Delta x$. A classical conservative method is used to

Table 4.2: An overview of model settings for the simulations of the channel-shoal system

Parameter	Value
Sediment formulation	van Rijn [87],[86]
Median grain size D_{50}	$240 \cdot 10^{-6}\ m$
Critical shear stress τ_c	$0.057\ \frac{kg}{ms^2}$
Morphological factor M	20
Chézy coefficient	$50\ m^{\frac{1}{2}}/s$
Bed slope parameters	$f_n = 5, f_s = 1$
Diffusion coefficient $\tilde{\epsilon}$	$0.3 \cdot 10^{-4}$
Time-step	10-100 s

Table 4.3: The dimensions of the computational cells (dx and dy), of the subgrid (δx and δy), the relative CPU times for all simulations of the channel-shoal system.

Simulation	dx $[m]$	dy $[m]$	δx $[m]$	δy $[m]$	Time Full	Time Reduced
A	50	50	25	25	100 %	100 %
B	100	100	100	100	1.8 %	1.9 %
C	125	250	125	250	0.39 %	0.35 %
D	250	500	250	500	0.09 %	0.07 %
E	500	500	500	500	0.035 %	0.02 %
F	100	100	25	25	7.8 %	4.0 %
G	125	250	25	25	6.2 %	1.3 %
H	250	500	25	25	7.0 %	0.9 %
I	500	500	25	25	4.0 %	0.5 %

smooth these [91].

Figure 4.6 shows the evolution of the bed over eighty years for Simulation F. It can be seen that the size and shape of the bed forms depend strongly on the local depth. The bed forms are much more developed in the deeper area of the basin. The length scales of the bed forms in the shallower area are much shorter and with a smaller amplitude. The different stages of the evolution are similar to those found in previous studies.

To compare the results for the concentration, the concentration is plotted in time. After forty years of bed evolution the results for three different simulations are shown in Figure 4.7. The results of the high-resolution simulation (A, yellow curves) and those with a coarser grid without and with the subgrid (C, blue curves and H, red curves, respectively) are presented. After forty years of bed evolution, the underlying bed is clearly altered. It is difficult to compare local concentration time series, as the value depends strongly on the local circumstances. Therefore, the spatial-averaged values for the water level, velocity, and concentration are shown.

The values are averaged for a section over the full width of the original channel between 20-40 km and between 60-80 km from the entrance. These values are representative for the deep and the shallow areas. The results for the water level and the velocity agree with the expectations based on results and experiences of other subgrid-based models ([25] [16] [44]). The propagation of the tidal wave is elongated by the coarseness of the grid. Due to the distortion of the tidal wave the velocities found in the areas is affected too, both in phase and in amplitude. The effect is larger in the shallow area, as depth variations are relatively more important and the wave shows the cumulative affect of the distortion as the wave is transplanted through the whole channel.

In the lower panels of Figure 4.7, timeseries of the concentration are plotted. First, the concentration of the simulation without the subgrid method (blue curve) is compared to the high-resolution run (yellow curve). Although the forcing (the bed shear stress) is able to resuspend the material, the distorted shape of the velocity wave does not allow enough sediment to be brought into suspension to reach equilibrium. There is insufficient time between low and high water to achieve the equilibrium sediment concentration, but also not enough time for it to settle down. In the shallow area the forcing of the coarse simulation is not able to bring the sediment into suspension. Moreover, because of the water level and the coarse grid, a smaller area can be wet at high tide. The concentration of the subgrid-based simulation (red curve) follows the high-resolution signal well. In the deep area the peaks of the concentration are underestimated. In this domain with deep water, advective processes play a more important role in the transport equation. In such case assumption (4.21) is insufficient to capture all processes.

In figure 4.8 the bathymetries of almost all simulations are shown after eighty years. Simulations D and E are not presented, as these full coarse-grid simulations did not show any significant bed forms. Comparing the other simulations, differences due to the grid resolution are clearly visible. However, in the simulations without subgrid (B and C), long, low bed forms are initiated. These are hard to see as they are small compared to the total depths. The length scales and the amplitude of the bed forms in the subgrid-based simulations are comparable to the high-resolution simulation. They do differ and are less pronounced when the computational grid is coarsened. An important difference for all simulations is that in all simulations the bed forms arise, but the speed at which they grow differs strongly. The results of simulation B, C, and I show some bed forms, but they are still in an initial stage. This is due to the effect of underestimating the tidal wave amplitudes and velocities.

Relative CPU-times are listed in Table 4.3. The CPU-time of the high-resolution simulation is set to 100 %. The times of the other simulations are compared to that, so all simulations were run in less than 8 % of the time it took to run the high-resolution simulation, which was approximately 5 weeks. By coarsening the grid, the computational effort reduces strongly. From these simulations it is also clear that the interpolation of the velocities and the computation of the bed update at high resolution becomes a significant part of the computational effort. A more detailed look at the computational effort, reveal that currently the velocity interpolation is expensive. This has partly to do with the programming style and could be optimised

for speed. Therefore, the computational effort without the velocity reconstruction is offered in Table 4.3 as well.

4.5. Discussion and conclusion

A new method is presented that is able to use high-resolution information in morphodynamic simulations that includes suspended sediment. The main aim of this study was to find a method to increase the accuracy of a coarse-grid based simulation of the sediment transport equation. The computational effort of coarse-grid simulations is much less than those performed at high resolution. However, the accuracy is strongly depended on the grid size. The subgrid-based approach includes high resolution information for solving the sediment transport equation. Thereby, the approach improves the accuracy of coarse-grid simulations, for a limited increase in computational effort.

For efficiency reasons, the sediment transport equation is solved at coarse resolution, while the bed update is performed at high resolution. However, the bed evolution and the sediment transport equations share the terms that describe the exchange of sediment between the water column and the bed. Moreover, local variations in bed characteristics such as depth, roughness, and sediment composition affect the concentration. For this study, it was crucial to find a method that takes these local effects into account and to couple the equations that are solved at different resolutions. To deal with the local variations in coarse-grid based simulations, the concentration was also allowed to vary within the computational domain of a single cell. To couple the sediment transport and the bed evolution equation, a sediment conserving method was defined. The best results were obtained when the local variation of the concentration was based on the zero-order approximation of the sediment transport equation, as derived by [55].

The optimal grid resolution of the coarse grid and the subgrid differs per application. It is suggested to choose the subgrid resolution based on the best available bathymetry data. In the second example, it was demonstrated that it takes some computational effort to include the effect of the high-resolution grid. However, the results improved significantly. As we use a fully explicit scheme, the interpolation method for the velocity and the sediment balances require only local sets of variables. This implies that this part of the computation can be efficiently parallelized. This would ensure a better performance. Still, when choosing the grid resolution of the coarse grid, a compromise is made between computational cost and grid resolution. However, by increasing the accuracy of the coarse-grid results, the balance between computational cost and accuracy improved.

Although, the procedure for choosing the optimal coarse-grid resolution does not change, a few things should be kept in mind. Even though, local variations of the concentration are accounted for on the high resolution grid, the dimensions of the coarse computational grid are still limited. Other processes can become important too, for example, the horizontal exchange by advection and diffusion. This was demonstrated in the concentration results from the simulations based on a coarse grid in Section 4.4.2. The processes for sediment transport are not described properly when the resolution of the coarse mesh is too low. This also applies to

the hydrodynamic solution and the interpolation of the water level and the velocity. However, flow variations in shallow, friction dominated areas, are often bathymetry driven. These effects are taken into account in the interpolation, and thus in the concentration and in the bed evolution.

The subgrid-based approach for suspended sediment is here derived for a structured, Cartesian grid. It is well possible to extend the method for grids that can be locally refined or refined in time [92]. It is quite straightforward to extend this method to a mesh with quadtree refinements [45]. The subgrid-based method was originally developed for three dimensional flow in a full unstructured grid ([16], [42]). However, to apply the subgrid-based approach for morphodynamics in such setting, the physics-based interpolation method described by [35] and the description of the advective terms needs to be generalized to a different grid structure.

Although, only one grain size was used in these examples, in principle this approach can account for varying grain size compositions. This is important as changes in the substrate also have to be included in long term simulations as discussed by [73]. Consequently, the subgrid method offers the potential to carry out multi-scenario, high-resolution morphodynamic simulations for a reasonable computational effort. This is an improvement over the current generation of morphodynamical models.

Acknowledgement
The work presented in this paper is carried out as part of the innovation programs Building with Nature and Knowledge for Climate. The Building with Nature program is funded from several sources, including the Subsidieregeling Innovatieketen Water (SIW, Staatscourant nrs 953 and 17009) sponsored by the Dutch Ministry of Transport, Public Works and Water Management and partner contributions of the participants to the Foundation EcoShape. The program receives co-funding from the European Fund for Regional Development EFRO and the Municipality of Dordrecht.

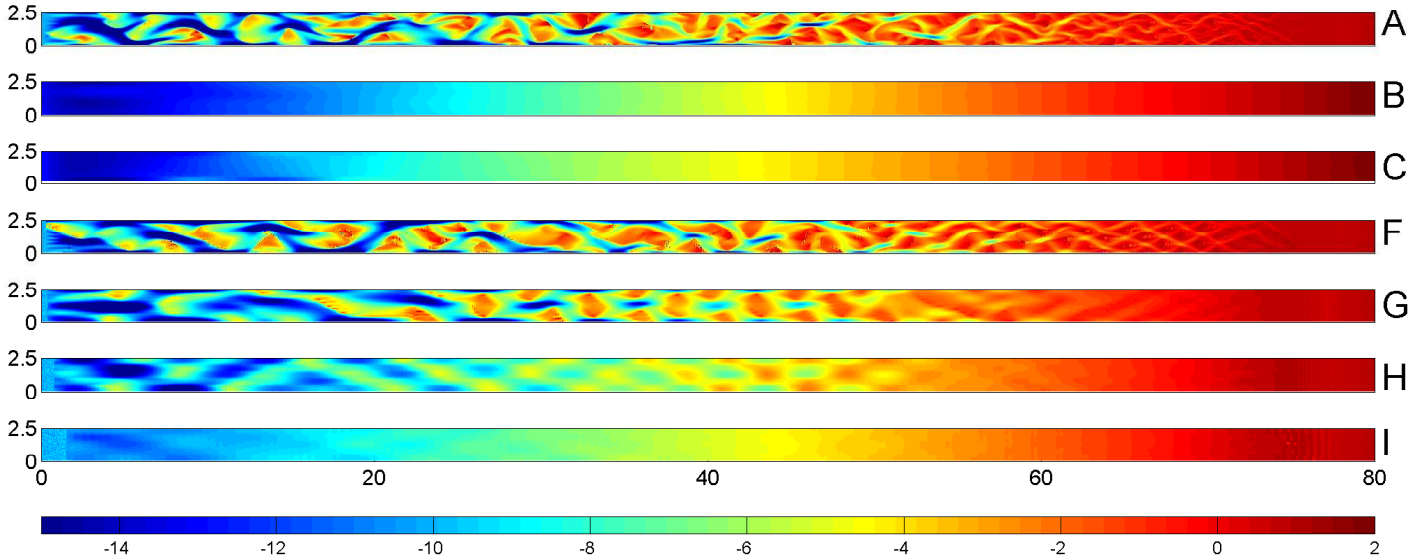

Figure 4.8: From top to bottom the bed after 80 years of evolution of simulations A, B, C, F-I. The dimensions of the axis are in kilometres and the colorbar in metres.

5

Further explorations of the subgrid based approach

Two illustrative examples are presented in this Chapter. The first example is an application of the hydrodynamic model to a real life case: the Westerschelde. This example shows, the positive effect of the subgrid method, when it would be applied in a real application. The second example is an illustration that there are still many topics to be investigated. It introduces a new simplified method for bank erosion. In, for example, river modelling, the erosion of the banks is a serious threat to the stability of the banks and the protection works against flooding.

5.1. A real life example

The Westerschelde is an estuary at the border between Belgium and The Netherlands. It is the main entrance from the open sea to the international harbour of Antwerpen. Therefore, unique habitats for flora and fauna, areas for recreational activities, the fish grounds for fisheries and navigation channels are competing for space. When, for example, maintenance work is planned in the estuary or adaptations to the navigation channels are requested, thorough studies are needed to predict the affects as accurately as possible. Calibrating models or modelling series of scenarios is laborious. An accurate and efficient model, such as the hydrodynamic model that is discussed in Chapter 2, can help in this process.

Model input

The bathymetry of the Westerschelde is shown in Figure 5.1. Characteristic features are the large gradients in the bed and the narrow creeks within the salt marsh at the end of the estuary. The bathymetry data of the Westerschelde[1] has a resolution of 40×40 m^2. The Westerschelde has been modelled numerous times (a.o. [77]

[1] Data recieved from T.van Kessel (Deltares) and D. Vertommen (Departiment Mobiliteit en Openbare Werken Vlaanderen)

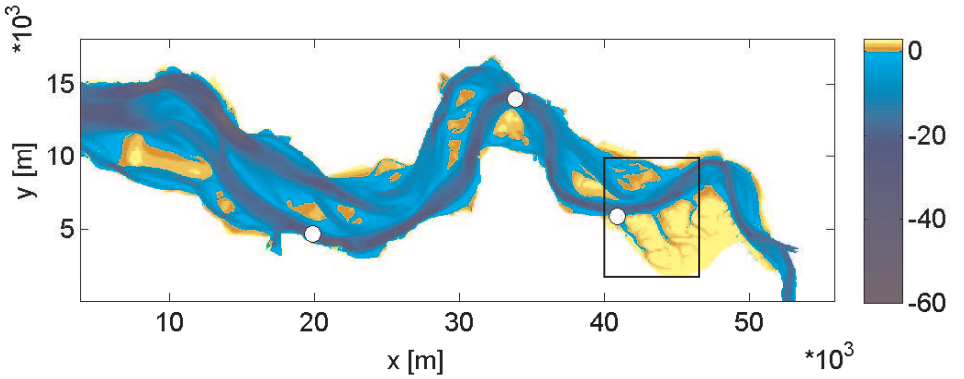

Figure 5.1: Bathymetry of the Westerschelde. The three white circles indicate the locations for which water level results are shown, these are from west to east near Terneuzen, Hansweert and het Land van Saeftinghe. The black box indicates the area in which velocity results are shown.

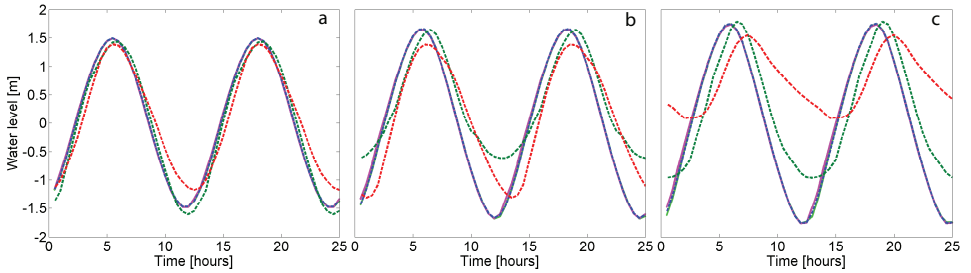

Figure 5.2: Water level result for simulations A (Blue), B (Light Green), C (Pink), D (dashed, Green) and E (dashed, Red). Water level results near: a) Terneuzen, b) Hansweert and c) Land van Saeftinghe.

[93] [94]), however, the resolution of the computational grid is generally chosen coarser than the available bathymetry data. Grid refinement techniques allow only a detailed description of the bed locally. Even though, an accurate representation of the bed elsewhere in the domain is crucial for accurate results, because the flow from these regions act as boundary conditions for the area of interest.

To visualize the effect of accounting for, or neglecting, high resolution bathymetry information, a series of simulations has been performed. The high resolution bathymetry data of the Westerschelde is used. The model domain is shown in Figure 5.1. The boundaries are set at the entrance of the estuary and in a narrow stretch of the river Scheldt. The main aim of these simulations is to show the effect of grid resolution in a real life application. We are not aiming at reproducing the exact flow within the estuary. In that case, the boundary conditions should have been calibrated and placed further outside the domain [77].

Five simulations are performed for this test case using the subgrid-based, two dimensional, depth averaged hydrodynamic model presented in Chapter 2. Simulation A is a high resolution reference run. The resolution of the computational grid is 80×80 m^2, instead of 40×40 m^2. This is, because of the high computational effort of such a high resolution simulation. The high resolution bathymetry information is used in this reference simulation, because the results benefit by it. Simulations B and C are coarse grid simulations that do not make use of subgrid information. The resolution of these simulations is coarse, they have computational cells of 480×480 m^2 and of 960×960 m^2, respectively. Simulations D and E use the same computational grid, but do account for the high resolution subgrid information. An overview of these five simulations is given in Table 5.1. The western boundary condition is a water level boundary defining a M_2-tide. At the eastern boundary the discharge is assumed to be negligible. Table 5.2 contains all settings of the model set up.

Results

Figure 5.2 shows the water level results at three different locations, which are indicated in Figure 5.1. The computed water levels near Terneuzen (Figure 5.2.a) are comparable to the high resolution reference simulation. The water levels, computed by the simulations without subgrid (dashed curves), show some deviation to the other simulations, especially during ebb. The tidal wave, simulated by these coarse grid simulations, arrives late at Terneuzen, whereas the results from the coarse grid simulations with subgrid are indistinguishable from the high resolution result. This trend is even more clearly visible in the water level results further down the estuary near Hansweert and the land van Saeftinghe, Figures 5.2.b and .c. The water level results, from the simulations with subgrid, remain accurate, during the full tidal cycle. Both the amplitude and the wave phase are consistent with the high resolution result. Whereas the results from simulations B and C, the coarse grid simulations without subgrid, do not capture the tidal cycle correctly. The phase and the amplitude deviate from the high resolution result.

In Chapter 2, it is explained, that the use of coarse computational cells can result in an overestimation of the friction. In these simulations, a uniform friction coefficient is used, which is equal for all simulations. An overestimation of the friction slows down the propagation of the tidal wave. This implies, a different behaviour of the flow during a tidal cycle. Moreover, for coarse grid based simulations, the storage capacity is underestimated, especially of the shallow areas, for example the area of the salt marshes. This affects the tidal signal as well.

The velocity results of simulations A, C and E are presented in Figure 5.3. It shows the velocity field within the box indicated in Figure 5.1. The snap shots are taken near maximum flood flow, because at that moment the water level results of all simulations are most similar. Besides, the highest velocities are found around that moment in the tidal cycle. White areas in the figures indicate dry domains. The high resolution velocity field is smooth, but shows various spikes at the wet-dry boundary. This phenomena is due to a lack of friction at the moment that the cell becomes wet. At that moment, there is no velocity computed yet, which can generate friction. This is corrected automatically during the next time step. This

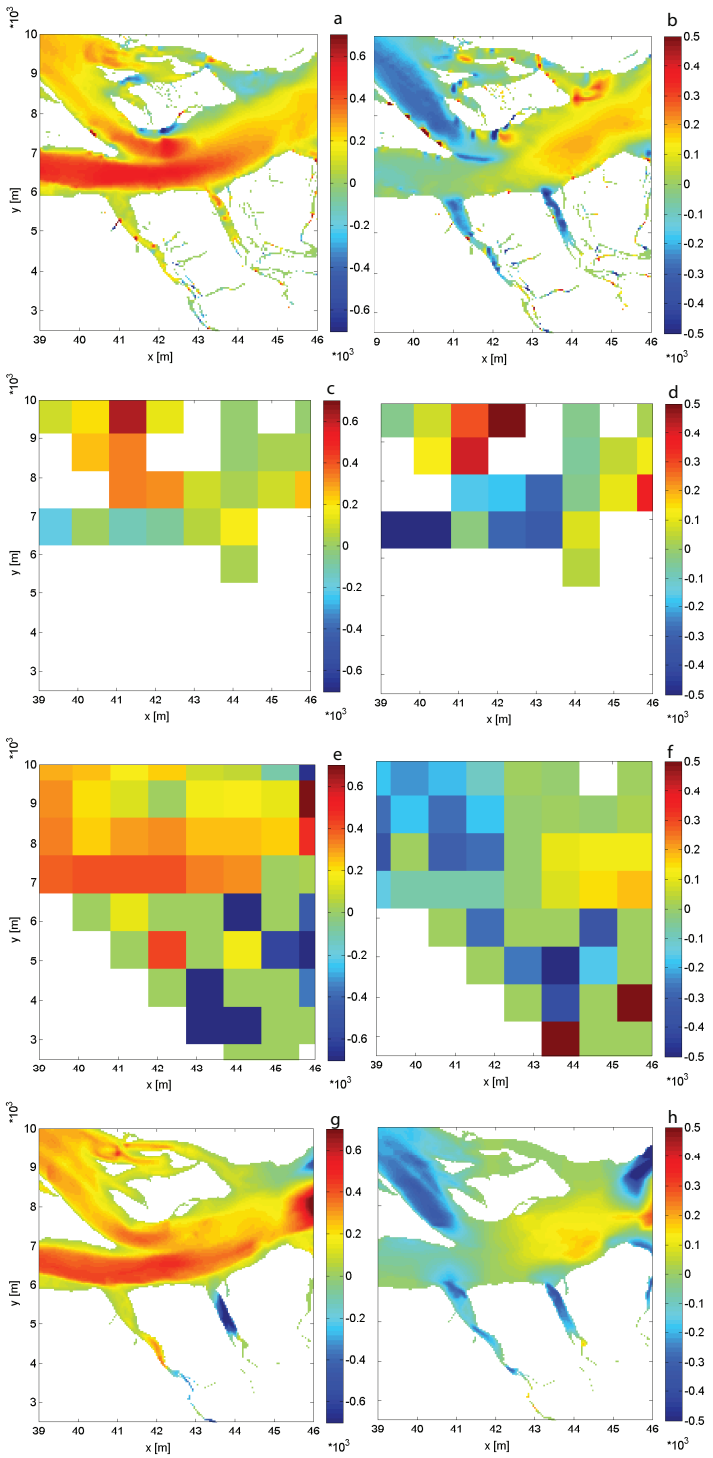

Figure 5.3: Velocity results in x- and y-direction of simulations a & b) A, c & d C and e-h) E. From simulation E both the coarse grid velocity results are shown (e & f) and the interpolated velocity field (g & h).

Run	Grid size	Subgrid	CPU-time
A	80×80 m^2	40×40 m^2	100 %
B	480×480 m^2	no	0.2 %
C	960×960 m^2	no	1.0 %
D	480×480 m^2	40×40 m^2	2.7 % (13 %)
E	960×960 m^2	40×40 m^2	3.2 % (11.9 %)

Table 5.1: Overview of the simulations performed for the Westerschelde. The dimensions of the grid cells are given and the computational cost relative to the high resolution run. The computational cost between brackets for simulation D and E include the velocity interpolation.

Parameter		Value
Time step	Δt	1 s
Chézy coefficient	C_z	50 m$^{\frac{1}{2}}$s^{-1}
Water level boundary	ζ_b	$1.3sin[\omega t]$
Tidal frequency	ω	$1.3963 \cdot 10^4$ s^{-1}

Table 5.2: Model settings for the simulations of the Westerschelde.

can be overcome by iterating the momentum equation locally to guarantee a velocity in that cell. The velocity field of simulation C shows a very coarse pattern, of which it is difficult to extract information. Although the water level at the moment of the snap-shot is similar, the tidal range is completely different. Therefore, the velocities can not be correct either. The coarse grid velocities of simulation E also gives a very coarse representation of the flow field.

In Chapter 3 a physics-based interpolation method is presented and it is used to reconstruct a high resolution velocity field. The overall pattern of the resulting velocity field resembles the high resolution result. There are, however, differences. The small scale features in the velocity field, which can be found in the result of the high resolution simulation, are not represented. On the edge of the reconstructed velocity field, a large eddy exists, which is not found in the high resolution result. In that area, the flow is forced through the bend, where in the high resolution simulation the interactions between the cells allow for a smooth transition of the flow. This is impossible in the coarse grid simulation. The area is covered with such a limited number of computational cells that the transition of the flow is forced abruptly. This might have generated the eddy.

The computational cost of the simulations are given in Table 5.1. The cost of the high resolution simulation is defined as 100 %. The costs of the coarser simulations are much lower than that. Note, that taking the high resolution bathymetry into account does affect the computational cost. However, the increase of the computational cost is limited, whereas the increase in accuracy is significant. The computational cost between brackets is the cost of the simulation when for each time step the high resolution velocity field is computed. Obviously, constructing the high

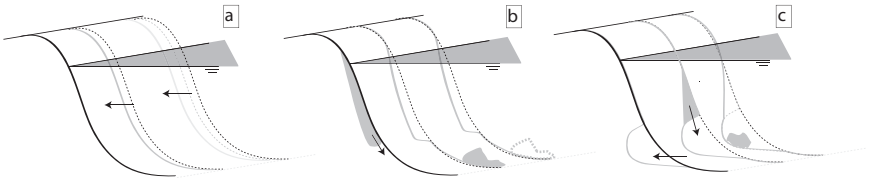

Figure 5.4: Three types of width adjustment; a) erosion b) sliding c) breaking

resolution velocity field for large cells is costly too. But note, this field can be constructed during the simulation, but also by post-processing. More importantly, the interpolation of the velocity field can be efficiently parallised. In such case, the affect on the computational cost will be minor.

Based on the results of the various simulations using the bathymetry of the Westerschelde, we conclude that the subgrid based approach is an accurate and efficient method that can be used in a real life applications.

5.2. A subgrid-based approach for bank erosion

Bank erosion is a phenomenon that can affect the stability of the coast line and river banks. Knowledge about when, where and to what extend banks will be affected is essential for safety. However, bank erosion is very difficult to describe properly. Multiple physical processes affect the erosion, of which many are not fully understood. We do not claim to have solved this problem by being able to model it using a subgrid based approach. We developed a simple routine in order to test, how the model would behave, when allowing bank erosion within a coarse grid cell. It is important to show whether an equilibrium state can develop.

The complexity of bank erosion or channel width adjustment originates from the interaction between various physical processes, which act on different time and length scales. How, when and where bank erosion takes place depends on the local and global flow, on the type of sediment involved, on the pore water pressure, and the availability of vegetation (among others [95] [96]).

Bank erosion takes on different forms of undermining the banks and depositing the sediment. The sediment of the banks can erode, slide as a sheet, or break down (Figure 5.4). These variations can occur simultaneously in the same domain. In the last decade, fully coupled models are being introduced [97]. In these models both the surface flow and the groundwater flow are modelled. Moreover, the local pore pressure and sediment characteristics are coupled with geo-technical relations for the bank stability. Based on these relations the bank behaviour is estimated. An accurate description of the bed, the sediment composition and bed gradient is required when modelling such a domain. We propose a subgrid based approach to couple the different spatial scales efficiently, to reduce the computational cost.

Subgrid based approach for bank erosion

We use the subgrid based, two dimensional, depth averaged hydrodynamic model in combination with the subgrid based approach for morphodynamics as was described

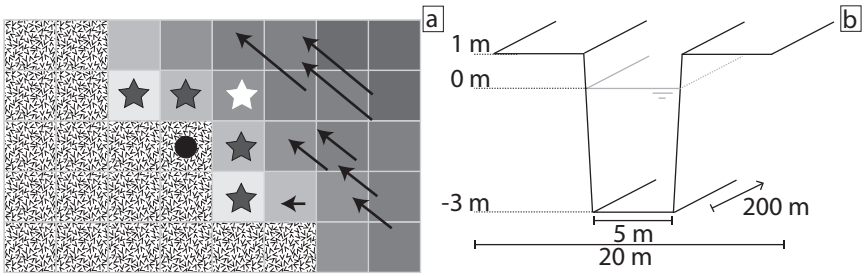

Figure 5.5: a) Schematic overview to determine bank erosion. The cells containing the 'V'-shapes are the cells that are dry. The grey background colour indicates the strength of the flow (from light to dark is for weak to strong flow) and the arrows the direction. The black dot indicates the dry cell of interest and the stars indicate the wet neighbouring cells. However, the white star indicates the cell where the maximum shear stress is and where the eroded material is deposited. b) Schematic view of bathymetry for the test case.

in Chapter 3. This model is extended with a module for bank erosion. We aimed to investigate the stability of the model when dry bed grid cells are eroded. The resolution of the bed grid cells is equal to the resolution of the subgrid. The focus is on bank erosion, due to shear stress (pure erosion), the other causes for bank erosion, sliding and breaking, are not taken into account. By allowing bank erosion, dry subgrid cells participate in the dynamics. For simplicity, the relation for the bank erosion (S) is only based on the maximum shear stress in the surrounding wet area:

$$S = A(\tilde{\tau} - \tau_c)^p \tag{5.1}$$

in which A and p are empirical parameters. A critical shear stress is defined (τ_c), which should be overcome to induce erosion. The erosion here is a function of the maximum shear stress ($\tilde{\tau}$) found in the neighbouring wet cells. The parameters A and τ_c could be functions of the local bed slope. Bank erosion can only take place when a minimum value of the bed slope is overcome. Here, we assumed the sediment to be deposited in the cell, where the maximum shear stress is found. This appears as an extra term in the bed evolution equation. It becomes:

$$(1-p)\frac{\partial \eta}{\partial t} = -\frac{\partial q_x}{\partial x} - \frac{\partial q_y}{\partial y} + S$$

the same notation is used as in Chapter 3. The erosion rate is defined positive. Therefore, the conservation equation for the dry bed grid cell is:

$$(1-p)\frac{\partial \eta}{\partial t} = -S$$

for which the sediment transport rates are zero. It is assumed for simplicity that the porosity p for the dry sediment equals that of the wet sediment.

Example

To test this module for bank erosion, a schematic test case was set up. A narrow channel of 5.0 m wide lies in the middle of two erodible banks, which are 3.0 m

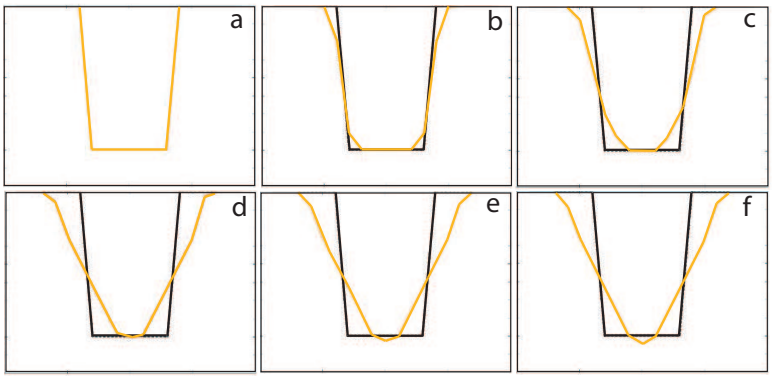

Figure 5.6: Various stages of bank erosion progressing in time from a-f.

higher than the channel bed. The banks are initially each 7.5 m wide. The length of the domain is 200.0 m. At the inflow boundary a discharge ($Q = 13$ m^3/s) is set and at the outflow boundary a Neumann boundary condition is set on the expected equilibrium slope of 0.0001. All other variables are configured as described in Table 3.2 in Chapter 3. The resolution of the subgrid is 0.5×0.5 m^2 and the resolution of the coarse hydrodynamic grid is 20×20 m^2. This implies that there is only one coarse grid cell over the width of the domain.

Figure 5.6 shows the development of the cross-sectional area half way down the channel until the cross-sectional area is stabilized. Initially, the complete banks are dry. In time, the banks erode until they become wet. From that moment the model treats them as normal bed grid cells and apply the normal sediment transport equations.

Although this model simplified the processes involved in bank erosion significantly, it does show the possibilities of using a subgrid based method. The availability of the bed slope and estimate of the bed shear stresses at high resolution can contribute in an improved prediction of bank erosion. This becomes especially important when interested in the affects on larger scales and for long time periods.

The recent developments involving subgrid based modelling are promising for the development of fully coupled models that include bank erosion. Many tools became available after Casulli [16] presented his subgrid based wetting and drying algorithm. For a proper description various facets should be coupled. The morphodynamic concepts should be combined with the possibilities of local grid refinements for optimal flexibility of the model [42] [45]. Moreover, the geo-technical formulations related to the pore pressure, ground water flow need to be included too. These can be applied at high resolution. Ground water flow can be included in a subgrid based model, allowing varying porosities at subgrid scale [98]. When all these facets are combined in a single model, it might be a very promising tool to investigate bank erosion, or river width adjustment and even for breach growth.

6

Discussion and Conclusions

"Life is short and there will always be dirty dishes, so let's dance!"

James Howe, Totally Joe

We have presented a subgrid based approach for the hydrodynamic and morphodynamic equations. High resolution bathymetry and roughness data can be taken into account in coarse grid simulations. This enhances the accuracy of the results for a limited computational cost. There are many advantages to this approach, but as with any method, there are clear limitations to it as well. A detailed discussion about specific aspects of the subgrid based approach is given in Chapters 2-4. A more general conceptual discussion is given here about several aspects of the methods. Additionally, an outlook on the wide range of applications and possibilities of the subgrid approach and an overall conclusion is given as well.

6.1. Before we turn on the music

The initial aim of this study was to improve morphodynamic simulations of inter tidal areas. There are various aspects one can choose to improve. One topic could be improving the knowledge about sediment grain dynamics, which it self is a broad field, that includes large scale effects of variations in grain size [99], but also to studies into the behaviour of individual grains [9]. Another aspect could be to study the effects of ecology on sediment characteristics [100], [101]. However, we have chosen to focus on problems encountered, when modelling the morphodynamic evolution of the bed in friction dominated areas.

Major issues for morphodynamic simulations is the computational effort and the stability of the numerical solution. The simplest solution for reducing the computational effort is reducing the grid resolution. Unfortunately, a reduction in grid resolution results also in a reduction of accuracy. Therefore, we studied various

methods to increase the accuracy of the numerical solution, without increasing the computational effort significantly.

First, a subgrid based approach for the hydrodynamics is presented. The finite volume approach for shallow water flow that accounts for high resolution bathymetry and roughness data is presented in Chapter 2. The approach is based on the flooding and drying algorithm that is developed by Casulli [16]. The approach uses two grids; a (coarse) computational grid and a (fine) subgrid. The computations of water levels and velocities are performed on the coarse computational grid. However, for many aspects of the computations the high resolution information, defined on the subgrid, is used. Within a coarse grid cell the water level is assumed uniform, while the bed level can vary. Based on these principles cell volumes and cell cross-sections can be based on the high resolution information. Since the water level is assumed uniform, it is inconsistent to assume a uniform velocity field within a cell. The velocity variation affects significantly the amount of friction and the flow distribution within a coarse grid cell. Therefore, an estimate of the velocity variation within a coarse grid cell is made, based on the high resolution bathymetry and roughness data. In order to define the friction and the advection terms, the local flow variations are taken into account by defining the so-called friction-depth. Thereby increasing the accuracy of the model results significantly, for a limited increase of computational effort. Moreover, the definition of the friction depth does not prefer a specific friction formulation. Chézy, Manning or any other formulation for the bed friction can be implemented.

The second step in improving the accuracy and the efficiency of morphodynamic modelling, was to determine the bed evolution at high resolution, while the forcing is computed at coarse resolution. The method is described in Chapter 3, but a key aspect of the subgrid based approach for morphodynamic modelling is the coupling between the coarse hydrodynamic grid and the high resolution bed grid. The physics-based interpolation method is developed, to reconstruct the high resolution velocity field. A combination of a simplified momentum balance and the continuity equation is used to combine the information from the coarse grid velocities, the bathymetry and roughness data to compute high resolution velocities. Based on this velocity field, bed shear stresses can be computed, to determine the sediment transport rates. The reconstruction works well in a wide range of applications, however, convergence, divergence and internal circulations within a coarse computational cell are excluded. This is a limitation to the resolution of the coarse computational grid.

The morphodynamic solution improved in two ways. First, the high resolution bed information could be preserved and updated. This has a significant positive effect on the accuracy of the hydrodynamic solution during the full morphodynamic simulation. This is important, because it implies an improvement of the forcing of the morphodynamical model. Secondly, the numerical diffusion is strongly reduced by computing the bed evolution at high resolution. The bed evolution equation lacks a natural damping term. This makes the system sensitive to artificial damping. This effect is stronger than in a hydrodynamic system, because in such system, damping is naturally caused by bed friction. As there is such a natural damping term for a hydrodynamic system, the artificial diffusion is often small compared to the natural

damping terms. In reality, the morphodynamic evolution is affected by damping as well. However, the bed evolution is described by a conservation law and empirical relations. These equations do not capture damping automatically. Damping is in such case only caused by numerical diffusion. This is not a good alternative to mimic natural damping, because numerical diffusion scales with the grid size and has no physical basis.

The local bed slope can affect the magnitude and the direction of the sediment transport [58] [88]. The terms describing this effect can serve as a damping term in the bed evolution equation [49]. The sensitivity to instabilities of the bed evolution equation is another consequence of the lack of damping terms. This remains an issue even when bed slope effects are taken into account, because of strong non-linear effects within the bed evolution equation and in the coupling with the hydrodynamic system. There are numerous approaches to deal with instabilities (for example [51]). In addition to those, an upwind numerical scheme based on the bed celerity was presented in Chapter 3. This approach enhances the stability significantly, without smoothing the solution.

The third step in improving the accuracy and efficiency of morphodynamic models is to include lag effects in the subgrid based approach for morphodynamic modelling. For optimal efficiency, the sediment transport equation is solved at a coarse computational grid. The consequence of this choice is that the deposition and erosion rates need to be defined at the coarse and the fine grid. Since, the bed update is computed at the high resolution grid. To take high resolution effects into account in the sediment transport equation, the concentration is allowed to vary within a computational domain. The variation is estimated based on the dominant balance within the transport equation [55]. Based on this local estimated concentration, the deposition rates are determined more accurately. The erosion rates are based on the constructed high resolution velocity field. Defining the net sediment balance at high resolution, improved the results of the bed evolution and the concentration computations significantly. However, by assuming a local balance between erosion and deposition other processes are neglected at this scale. This is a clear limitation to the size of the coarse grid cell.

Although we have shown that the results improved significantly by taking the high resolution information into account, the subgrid based approach is not a solution for lack of resolution. The subgrid based approach improves the accuracy of coarse grid based simulations by accounting for high resolution information. The main aim was to improve the morphodynamic modelling of inter-tidal areas. Flows in estuaries, coastal areas and in low land rivers share some key characteristics. All these systems have friction dominated flows. With that in mind, we could include additional information into the model within a computational domain. However, this also implies, that at small scale other processes are neglected. When interested in local convergence, divergence or circulations or their affects, the computational grid needs to be fine enough to resolve this. For detailed computations of the flow, high resolution simulations are still necessary.

Throughout the thesis, we have claimed that the accuracy of the solution increased significantly due to the use of the subgrid based approach. However, the

accuracy of numerical methods is often defined by the convergence rate of the solution. This is the rate with which the solution converges to the ideal solution when decreasing the grid size. Based on such analysis, higher order discretisation schemes are more accurate than lower order schemes. The results from the subgrid based simulation show a strong consistency for different grid sizes. This implies a very low convergence rate. However, this does not mean that the subgrid based approach is inaccurate. An accurate description of the system is essential in obtaining the correct solution. The increase in accuracy of the subgrid based method is due to a precise representation of the system for all different computational grid sizes. The solution of a model based on a higher order numerical scheme in a coarse grid based simulation without using the subgrid based approach gives a more accurate result of the wrong system. This is in comparison to a lower order scheme. Note, that the subgrid based method does allow for higher order discretisation schemes, which can still improve the results.

High resolution simulations contain details of the flow, which cannot be obtained by coarse grid based simulations. The optimal ratio between the resolution of the subgrid and the coarse grid differs per application. However, based on our experience and the experience from other subgrid based models [16], [42], [45], [44] there are some general remarks to be made. The resolution for the subgrid should be the dataset with the highest resolution that is still reliable, because of the large efficiency of the model approach. The optimal coarse grid resolution for a specific application depends on the purpose, the available time and the required accuracy. The trade off, between accuracy and computational effort, remains challenging. However, the results from coarse grid simulations, for example those of the Westerschelde case (Section 5.1), show a strong consistency between the various grid resolutions. Differences do appear at local scale in the flow distribution, but the large scale phenomena are captured well. Due to this high accuracy of the results even for large computational cells, the trade off between resolution and computational cost is improved.

The consistency in the results would allow to carry out numerous coarse grid simulations for a limited computational cost. This has a strong advantage during the calibration process of a model. This also holds, when investigating a range of conditions. Instead of a small number of high resolution simulations, numerous coarse grid simulations can be performed for the same computational cost. This is especially valuable for morphodynamic simulations, because these still suffer from many uncertainties as the included processes are strongly empirical based.

6.2. We still need some dance lessons

The subgrid based approach on which we have based our method is a relatively new development, that was first initiated by Casulli [16]. A wide range of new aspects is still to be explored. First, we will discuss some issues concerning the grid and the computational efficiency. After which, we elaborate on some aspects related to more physical phenomena.

Within the full flow domain of, for example a river or an estuary, the characteristic length scales of the flow can vary, therefore local refinements of the computational

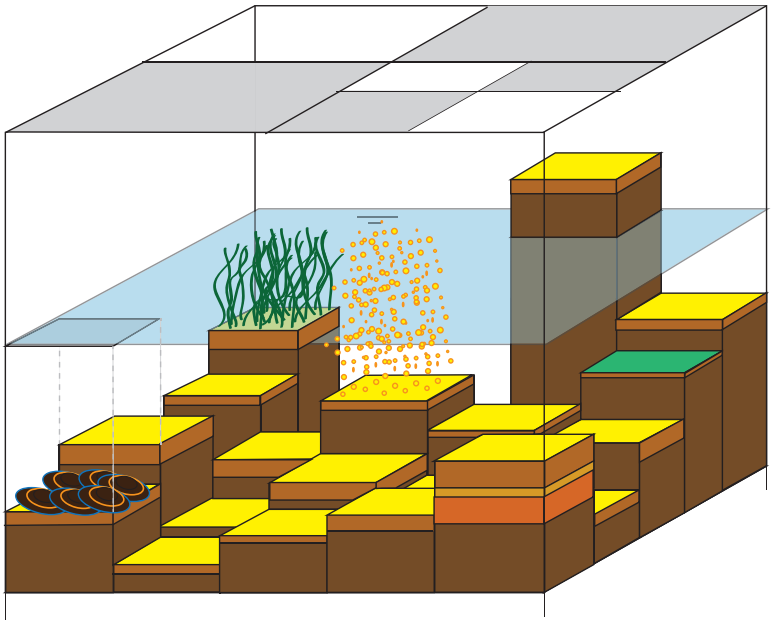

Figure 6.1: An overview of various possible new aspects.

grid can be important for optimal efficiency of the model. The subgrid based approach, as presented in this thesis, is not limited to regular, structured grids. There are several methods for local refinements developed, also in combination with subgrid. One option is to use a fully unstructured grid, which allows the grid to be fully adjusted to bathymetry and flow variations [42]. Another option to refine the computational grid locally, is using quad-tree based grid [45]. The flexibility of a fully unstructured grid, can be advantageous, although the discretisation of some processes can become very complex. However, when using a subgrid based method, the grid is allowed to have partly wet and dry cells. The actual computational domain of the model adjusts automatically in time and space. In a quad-tree based grid, it is possible to have local refinement, but much of the regularity of the grid is preserved. This limits the flexibility of the refinements, but it allows for more simple discretisation schemes.

When the computational domain is large, but the details of the flow are only of interest in a much smaller domain, two different models can be nested. Coupling of the two models is difficult, because the input and the solution are different, depending on the resolution of the two models. The subgrid based approach allows for a more smooth transition, as cross-sectional areas, amount of friction and storage capacity are nearly equal. Eventually, both models could make use of the same high resolution information.

A recent development to increase the efficiency of hydrodynamic models is the use of a multiple grid solver. This is especially useful for the simulation of (near) stationary flows. Such a solver uses hierarchical grids in solving the hydrodynamic

system. The set of equations is solved sequentially on different grid resolutions. First, it is solved on a coarse grid of which the solution is interpolated on a finer grid. This fine solution is used as initial condition to compute a higher resolution solution. This process is repeated until the desired resolution is reached or reversed when necessary. Perturbations in the solution of different length scales can be more efficiently filtered at the different grids. A subgrid based model allows a good representation of the volume and the flow for all grid resolutions. This implies that perturbations introduced by changing the grid resolution are reduced. This results in a better convergence of the method [102].

Still, computer power is increasing and also the use of using multiple CPU's in combination with GPU's. The use of multiple computer cores allow to divide some of the computer tasks. When multiple cores are used, the computer can compute various processes simultaneously, which naturally reduces the total computational cost. Especially GPU's are becoming cheaper and the number of applications for which they are useful is growing. Therefore, their use will be extended in the future [103]. However, the use of multiple cores can be complex, especially when the processes that are being computed are strongly dependent. In such case, a core needs input from other cores. From the examples in Chapter 3-5 it appeared that the full velocity reconstruction and computing the morphodynamic response is relatively costly. Yet the reconstruction of the velocities is a local computation, which does not require input from other areas and is completely explicit. For the morphodynamic computations is also an explicit discretisation scheme used. Therefore, this part of the computations is very suited to be computed simultaneously, which could enhance the efficiency significantly.

The subgrid based approach has more advantages than only grid related issues. There are various physical processes of which the implementation can benefit from high resolution data. Especially, for processes that act locally, but affect a large system. Dealing with local phenomena in large domains is still a major challenge. However, we do see opportunities for a subgrid based approach. This is mainly, because a subgrid based approach would allow to take local effects into account in a much larger domain at a acceptable computational cost. In Section 5.2 we already illustrated how bank erosion could be captured at subgrid level. We will give here some other examples of local phenomena that affect the system at much larger scale.

In recent years, it appears that the effects of biota on the system characteristics is important. Vegetation, oyster reefs, patches of shells and benthic fauna can change the bed roughness and the sediment characteristics [101]. Vegetation changes the forcing of the bed, but also the erodibility of the sediment [104]. Benthic species can also directly affect the erosion by feeding [100]. Such local processes can be implemented directly in the erosion equation on subgrid level.

Numerical models have recently been applied to simulate marsh development [105] to be combined with hydrodynamic and morphodynamic models. Such models are applied to predict, for example, the effects of marshes on flood risk. These type of simulations require a very high spatial resolution as channels cut through the vegetated areas. This high spatial resolution has a large impact on the computational effort. This is unfortunate, because for understanding the processes in these

types of areas multiple scenarios studies would be valuable. These channels are well captured when using a subgrid based approach. In Chapter 2 it was shown that the roughness can be varied within a coarse computational cell. A roughness that varies in time and space within a computational cell could be an adequate approach for low vegetation and for patches with shells. However, for vegetation that not only covers the bed, but grows much higher as, for example, reed marshes or even mangroves, such an approach would not be sufficient. This type of vegetation affects not only the roughness, but also the drag and the storage capacity of an area [106, 107]. In that case, a relation for the drag from vegetation should be added to the momentum balance. This could be done by defining a term that is quadratic to the velocity and a porosity function. These should be related to the type of vegetation and allow for changes in space and time.

Dealing with a porosity in combination with a subgrid based approach is already developed for ground water flow. An adjusted Newton iteration can solve such a non-linear system [98]. Moreover, the effects from biota on sediment transport could be locally taken into account by adjusting the erosion rates at high resolution. Nonetheless, many of the required relations are not yet known.

Originally, the subgrid based approach was presented for a three dimensional unstructured orthogonal grid [16]. It appeared, however, that also in the three dimensional case the friction was overestimated when accounting for subgrid topography, but assuming a uniform velocity within a computational domain [44]. This effect is similar to what was found for the depth averaged case. Two types of solutions are already presented for this issue. The first solution is similar to the approach presented for the depth averaged case in Chapter 2. It makes an estimation of the velocity variation within a cell, however the extension to three dimensions requires an empirical tuning parameter Sehili *et al.* [44]. The second method allows to solve a momentum equation for all sub cells on the edge of a coarse grid cell. This has the advantage that velocities are computed at higher resolution based on a full momentum equation. However, this is difficult to combine with a momentum conserving formulation for advection. Moreover, only the bathymetry variation along the edge is taken into account, whereas friction is typically a force acting on a surface. Especially, when using large cells in combination with a strong varying bathymetry this needs to be taken into account. The method introduced in Chapter 2 can be extended to three dimensions. A pre-liminairy derivation is included in the Appendix A.

Another application, where the subgrid based approach has proven to be very promising, is in flooding simulations. As flooding and drying is automatically taken into account, the subgrid based approach is very suited for this type of modelling. It has been proven, that the method is also effective in urban areas, where flooding can also be caused by, for example, precipitation. The full sewer system and ground water flow can be taken into account [45] [108]. It would be very interesting to extend the use in early warning systems for tsunamis and to determine in real time the effects of storm surges [109]. In addition, subgrid based models can be very suited to determine the withdrawal of water after a hazard. Many innovative techniques have been developed in recent years, but we do believe there are still

many opportunities left, which are worth to be investigated.

6.3. Let's dance!

The present day society is challenged to improve and to preserve a high level of security against floods and natural hazards under changing conditions. This challenge is in addition to the improvement and maintenance of the navigability and the area use in and near rivers, coastal areas and estuaries. However, measures that have worked in the past, are often not sufficient any more, because other aspects, such as water quality and ecology, have gained in importance. Therefore, the impact of measures on these aspects need to be known in advance. This is a huge challenge for scientists and for policy makers, as knowledge about these aspects and how they influence larger systems is still limited.

The subgrid based approach for hydrodynamic and morphodynamic modelling is an accurate and efficient tool to investigate long term effects on the bed evolution and the sediment concentration. The method provides accurate results even for coarse grid based simulations. This is important when results are needed at short term and when long simulation periods are required. The method takes flooding and drying automatically into account, which makes the method very useful in tidal areas and for flooding applications. Still there is a trade off in grid resolution and computational effort. However, due to the subgrid based approach this trade off shifted, because the accuracy significantly improved for coarse grid based simulations. Moreover, there are many opportunities to take new processes into account that are locally defined, but affect systems as a whole. The subgrid based approach is a new development, therefore many opportunities still need to be investigated. However, the initial results are promising and trigger us to do more. Therefore, it is time to start using the subgrid based approach for hydrodynamic and morphodynamic modelling beyond the scientific environment.

Acknowledgements

Acknowledgements have the tendency to get very cheesy. This is partly because you are allowed to thank people, who had nothing to do with the content of the work, that has been done. However, these people did make my life much more interesting and enjoyable during the same period. Therefore, I would like to thank my friends; my paranymphs, de supernerden, de overvechtpossie and all the others, and my family; my mother, my sister, Maup and of course especially Minne for being around, for sympathising with my moments of sadness and creating moments for celebration.

Naturally, there are quite some people who made major contributions to this thesis. First of all, I would like to thank Guus for his fantastic stories about all topics ranging from numerical methods to politics, love, songs of Jaap Fisher and sports. Especially, the stories about numerical methods have helped my research itself, but the others made our meetings extremely enjoyable. Guus his knowledge of and experience with numerical methods and approaches seems endless, as well as his ideas to improve them. I admire his practical views on mathematical and physical principles.

Bram, being your first official phd student we took a journey together. We had lots of discussions, trips and we learned a lot. Your input for the morphodynamic part has been very important$*$. Also your critical views on results and methods we have tried, were very valuable. I really enjoyed working with you, organising NCK days, our field trips and definitely also discussing daily life issues.

Julie, you joined our little team halfway the project, when Guus became officially an emeritus professor. Your enthusiasm to get to know a new field of science is inspiring. Your critical views on our Dutch version of English taught me a lot about Monty Python styles and that when you intend to say when something is important you should actually say it is crucial or essential (see $*$, but for my Dutch ears, it sounds just too theatrical).

Frank started his research related to subgrid methods a bit after me. I really enjoyed sharing our findings and results about our research. Being the only 'subgrid-phds', we shared our specific subgrid issues with each other. Fortunately, we are certain that in the end 'everything is fine on subgrid'.

I definitely need to thank my Roomies at the TU for their distractions, advice, warm words and hugs, which kept me sane when searching for code bugs, words, coffee or just entertainment. Actually, I also could thank all my other colleagues at the TU for that as well. These people made sure I have had a terrific time.

Finally, I want to mention the people I yearly encountered at the UnTrim Workshop. I was allowed to present my small steps towards the subgrid based morphodynamic method, even though I was not using UnTrim. I always felt, that all

Figure 6.2: A crab from the Wadden Sea. (This picture is made by J. de Jong. Thank you for this picture, it played an important role in many of my presentations.)

participants; Vincenzo Casulli, those of the BAW, and the users from other locations in the world, were genuinely interested in the methods and the results.

In short, the main message of this small chapter is that I had a great time, thanks to all the different kinds of support I have had.

A

Subgrid Based Approach for Bed Friction in a Three Dimensional Finite Volume Model

A.1. Introduction

The accuracy and the efficiency of coarse grid models increased significantly by the introduction of subgrid based models [16] [11] [45] [67]. In these models high resolution bathymetry and roughness information can be taken into account on the subgrid. The accurate description of the bathymetry is essential to obtain accurate results. However, it also appeared that this information should also be taken into account in the formulation of the friction [11] [44]. When the water level is uniform within a coarse grid cell and the bed level varies, it is inconsistent to assume the velocity to be uniform. The internal variation of the flow has especially consequences for the friction formulation.

Bed friction is formulated as a non linear relation of the bed shear stress, which includes the velocity and the roughness. Chapter 2 shows the importance of including the high resolution information in the formulation of the bed friction in a two dimensional depth averaged model. Chapter 6 discusses that in a three dimensional model it is also important to include high resolution information in the formulation of the bed friction. Here, the approach as described in Chapter 2 is extended to a three dimensional setting.

A.2. Derivation

To improve the accuracy of subgrid based three dimensional models, we would like to improve the formulation of the bed friction. A similar approach is used as was

A

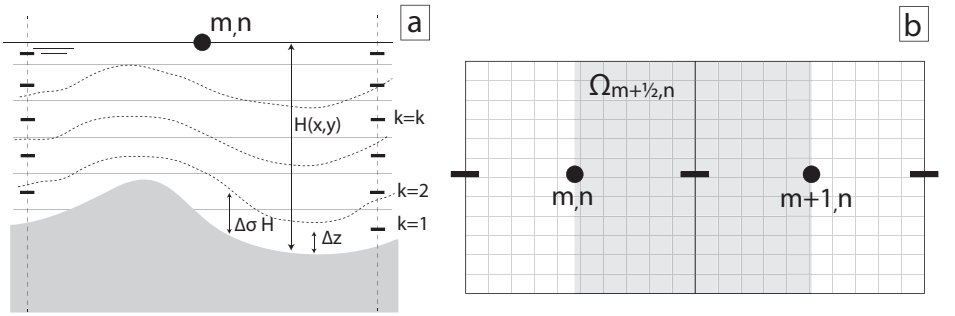

Figure A.1: a) An overview of a coarse grid cell with a varying bed. There are z-layers and σ-layers. b) Top view of two coarse grid cell with an underlying subgrid.

presented in Chapter 2 for a depth averaged model. The bed friction was then based on an estimate of the high resolution variation of the depth averaged velocities. Here, an estimate will be made of the high resolution variation of the shear velocity. In order to make the estimate, the key assumptions are that the flow is friction dominated and that the velocity profile in the bottom layer acts according to a logarithmic profile.

Figure A.1.a shows a grid cell with multiple vertical layers and a varying bed. The derivation is performed for a Cartesian grid, where water levels/ pressure points are defined at the cell centres and velocities at the cell/ layer edges. The vertical distribution of the layers can be in a three dimensional model along depth contours (z-layers) or a specific number of layers is defined and distributed according to the local depth (σ-layers). Both types are included in the figure. For the derivation, the vertical layers are locally σ-layers. This does not imply that the whole model should be based on σ-layers. This will become clear at the end of the derivation. The notation for the variables of Chapter 2 is used, only an index is added to indicate the vertical layers ($k = 1, \ldots, K$, starting from the bottom layer). Table A.1 contains various variables and there meaning. For simplicity, the derivation is performed for a x, z -model, however there is variation on subgrid level in y-direction.

In order to define the bed friction in terms of the coarse grid velocity of the bottom layer and the high resolution bathymetry and roughness information, the bed friction is rewritten in terms of the shear velocity (u_*):

$$\tilde{F}_{b;\Omega} = \iint_{\Omega} \frac{\tau_b}{\rho} \, d\Omega = \iint_{\Omega} u_*^2 \, d\Omega \qquad \Omega \in \Omega_{m+\frac{1}{2},n} \tag{A.1}$$

in which the bed friction is normalised by the density. The velocity profile within the bottom layer is assumed to follow a logarithmic profile:

$$u_k(x, y, z, t) = \frac{u_*}{\kappa} ln \left[\frac{z + z_0}{z_0} \right] \tag{A.2}$$

in which z_0 is the roughness height. The roughness height is added to z, this is a choice to guarantee the velocity to be zero at the bed. This is independent of the

Table A.1: Definitions, water levels and velocities are piecewise continuous functions, which are defined using the discrete variables and the indicator function.

$\Omega_{m+\frac{1}{2},n}$	Wet domain within momentum domain $m+\frac{1}{2},n$
$\zeta(x,y,t)$	Water level
$u_k(x,y,z,t)$	High resolution velocity in x-direction of layer k
$v_k(x,y,z,t)$	High resolution velocity in y-direction of layer k
$u_{c:k}(x,y,z,t)$	Coarse grid velocity in x-direction of layer k
$v_{c:k}(x,y,z,t)$	Coarse grid velocity in y-direction of layer k
ρ	The density, which is assumed constant
κ	The von Karman constant
$H(x,y,t)$	Total depth
σ_k	Depth distribution according to σ-layers
Δz	Height of lowest velocity point
z_0	Roughness height

subgrid based approach and can be chosen differently. The shear velocity can be determined when the velocity at a specific depth, the velocity point (Δz), is known according to:

$$u_* = \frac{\kappa}{ln\left[\frac{z+z_0}{z_0}\right]} u_k(x,y,z,t) \quad \rightarrow \quad \begin{aligned} u_* &= \frac{\kappa}{ln\left[\frac{\Delta z+z_0}{z_0}\right]} u_k(x,y,\Delta z,t) \\ &= \tilde{c}_f u_k(x,y,\Delta z,t) \end{aligned} \tag{A.3}$$

A modified friction coefficient ($\tilde{c}_f$) is introduced, which is independent of the velocity. This friction coefficient can vary at high resolution scale. The high resolution velocity $u_k(x,y,\Delta z,t)$ varies within a momentum domain $\Omega_{m+\frac{1}{2},n}$. However, this velocity is unknown. Therefore, two relations between the coarse grid velocity and the subgrid velocity are defined:

$$u_{c:k}(x,y,\Delta z,t) = \frac{\iint_\Omega u_k(x,y,\Delta z,t)\sigma_1 H \, d\Omega}{\iint_\Omega \sigma_1 H \, d\Omega} \quad \text{for} \quad (x,y) \in \Omega = \Omega_{m+\frac{1}{2},n} \tag{A.4}$$

$$u_{c:k}(x,y,\Delta z,t) = \gamma(x,y,t) u_k(x,y,\Delta z,t) \quad \text{for} \quad (x,y) \in \Omega = \Omega_{m+\frac{1}{2},n} \tag{A.5}$$

The first relation defines that the coarse grid velocity of the bottom layer is the volume average of the high resolution velocities in that layer. The second equation defines that the coarse grid velocity is linearly related by γ and the high resolution velocity. When equation A.5 is submitted in equations A.3 and A.1:

$$\tilde{F}_b = \iint_\Omega \frac{\kappa^2}{ln^2\left[\frac{\Delta z+z_0}{z_0}\right]} u_k^2 \, d\Omega = \iint_\Omega \tilde{c}_f^2 \frac{u_{c:k}^2}{\gamma^2} \, d\Omega = u_{c:k}^2 \iint_\Omega \frac{\tilde{c}_f^2}{\gamma^2} \, d\Omega \tag{A.6}$$

The factor γ is unknown. Therefore, we assume similar as in Chapter 2, a uniform friction slope. This implies that the balance between friction and forcing is assumed

A

to be dominant and uniform within a momentum domain. The friction slope (S) is defined as:

$$S = \frac{u_*^2}{gH} = \frac{\tilde{c}_f u_k^2}{gH} = uniform \quad \text{for} \quad (x,y) \in \Omega = \Omega_{m+\frac{1}{2},n} \tag{A.7}$$

Combining the uniform friction slope with equations A.4 and A.5 expresses γ in terms of the high resolution information:

$$\begin{aligned} \gamma = \quad & \frac{u_{c;k}}{u'_k} = \frac{\iint_\Omega u_k \sigma_1 H \, d\Omega}{u'_k \iint_\Omega \sigma_1 H \, d\Omega} = \frac{\sqrt{\frac{\tilde{c}_f}{gH}} \iint_\Omega u_k \sigma_1 H \, d\Omega}{\sqrt{\frac{\tilde{c}_f}{gH}} u'_k \iint_\Omega \sigma_1 H \, d\Omega} \\ = \quad & \frac{\sqrt{\frac{\tilde{c}_f}{H}} \iint_\Omega \frac{u_k}{u'_k} H^{\frac{3}{2}} \tilde{c}_f^{-\frac{1}{2}} \sigma_1 \, d\Omega}{\iint_\Omega \sigma_1 H \, d\Omega} = \frac{\sqrt{\frac{\tilde{c}_f}{H}} \iint_\Omega H^{\frac{3}{2}} \tilde{c}_f^{-\frac{1}{2}} \, d\Omega}{\iint_\Omega H \, d\Omega} \end{aligned} \tag{A.8}$$

for $(x,y) \in \Omega = \Omega_{m+\frac{1}{2},n}$ and $u'_k = u_k(x', y', \Delta z, t)$. Note that the relative depth of the vertical layer is uniform, by choosing σ-layers σ cancels out. By defining γ the relation between the coarse grid velocity and the subgrid velocity is determined. Equation A.6 becomes after substituting γ:

$$\begin{aligned} \tilde{F}_b = \quad & \iint_\Omega \frac{\tilde{c}_f u_k^2 \left(\iint_\Omega H \, d\Omega \right)^2}{\frac{\tilde{c}_f}{H} \left(\iint_\Omega H^{\frac{3}{2}} \tilde{c}_f^{-\frac{1}{2}} \, d\Omega \right)^2} = \frac{u_k^2 V_\Omega^3}{\left(\iint_\Omega H^{\frac{3}{2}} \tilde{c}_f^{-\frac{1}{2}} \, d\Omega \right)^2} \\ = \quad & \frac{u_k(x,y,\Delta z,t)^2 V_\Omega^3}{\left(\iint_\Omega H^{\frac{3}{2}} \left(\frac{\kappa}{ln\left[\frac{\Delta z + z_0}{z_0} \right]} \right)^{-\frac{1}{2}} d\Omega \right)^2} \end{aligned} \tag{A.9}$$

The bed friction is now expressed in terms of the coarse grid velocity and the high resolution bathymetry and roughness data. The expression is independent of the type of vertical layers. The derivation is performed or a two dimensional x,z-models. Chapter 2 shows by introducing four sub-domains within a coarse grid cell how it can be extended to a full three dimensional setting.

References

[1] UNPF, *State of World Population 2007, Unleashing the Potential of Urban Growth*, Tech. Rep. (United Nations Populations Fund, 2007).

[2] T. H. Flowers, *The design of colossus,* Annals of the History of Computers **5** (1983).

[3] M. B. Abbott, *Computational Hydraulics* (Pitman Publishing Limited, 1979).

[4] P. D. Lax, *Weak solutions of non-linear hyperbolic equations and their numerical applications,* Communications Pure and Applied Mathematics **7** (1954).

[5] Wesseling, *Principles of computational fluid dynamics* (Springer, 1991 (updated in 2000)).

[6] T. Petrila and D. Trif, *Basics of fluid mechanics and introduction to computational fluid dynamics* (Springer, 2005).

[7] J. D. Loftis, H. V. Wang, R. J. DeYoung, and W. B. Ball, *Using lidar elevation data to develop a topobathymetric digital elevation model for sub-grid inundation modeling at langley research center,* Journal of Coastal research (2015), 10.2112/SI76-002.1.

[8] F. M. Exner, *Zur physik der dunen (in german),* Sitzber. Akad. Wiss Wien (1920).

[9] M. Nabi, H. J. de Vriend, E. Mosselman, C. J. Sloff, and Y. Shimizu, *Detailed simulation of morphodynamics: 3. ripples and dunes,* Water Resources Research **49**, 5930 (2013).

[10] H. J. de Vriend, *Analysis of horizontally two-dimensional morphological evolutions in shallow water,* Journal of geophysical research, Oceans **92(C4)**, 3877 (1987).

[11] N. D. Volp, B. C. van Prooijen, and G. S. Stelling, *A finite volume approach for shallow water flow accounting for high-resolution bathymetry and roughness data,* Water Resources Research **49**, 4126 (2013).

[12] B. F. Sanders, J. E. Schubert, and H. A. Gallegos, *Integral formulation of shallow-water equations with anisotropic porosity for urban flood modeling,* Journal of Hydrology **362**, 19 (2008).

[13] L. Cea and M. E. Vázquez-Cendón, *Unstructured finite volume discretization of two-dimensional depth-averaged shallow water equations with porosity,* International Journal for Numerical Methods in Fluids **63**, 903 (2010).

[14] P. D. Bates, *Development and testing of a subgrid-scale model for moving-boundary hydrodynamic problems in shallow water,* Hydrological Processes **14**, 2073 (2000).

[15] D. Yu and S. N. Lane, *Urban fluvial flood modelling using a two-dimensional diffusion-wave treatment, part 1: mesh resolution effects,* Hydrological Processes **20**, 1541 (2006).

[16] V. Casulli, *A high-resolution wetting and drying algorithm for free-surface hydrodynamics,* International Journal for Numerical Methods in Fluids **60**, 391 (2009).

[17] H. Lorentz, H. Wortman, E. van Everdingen, W.F.Stoel, W. K. Behrens, P. Gallé, C. Lely, A. van Loon, L. H. Mansholt, R. de Muralt, J. Phaff, C. Reigersman, J. van der Stok, D. Wouda, J. Wijtenhorst, and L. de Nerée tot Babberich, *Verslag Staatscommissie Zuiderzee 1918-1926*, Tech. Rep. (Staatscommissie (Govermental Commision), 1926).

[18] G. K. Lotter, *Considerations on hydraulic design of channels with different roughness of walls,* Transactions All Union Science Rescources, Inst. Hydraulic Engineering **9**, 238 (1933).

[19] M. J. Aftosmis, M. J. Berger, and J. E. Melton, *Robust and efficient cartesian mesh generation for component-based geometry,* AIAA Journal **36**, 952 (1998).

[20] T. Ye, R. Mittal, H. S. Udaykumar, and W. Shyy, *An accurate cartesian grid method for viscous incompressible flows with complex immersed boundaries,* Journal of Computational Physics **156**, 209 (1999).

[21] D. M. Causon, D. M. Ingram, and C. Mingham, *A cartesian cut cell method for shallow water flows with moving boundaries,* Advances in Water Resources **24**, 899 (2001).

[22] R. Mittal and G. Laccarino, *Immersed boundary methods,* Annu. Rev. Fluid Mech. **37**, 239 (2005).

[23] I. Poretti and M. G. M. De Amicis, *An approach for flood hazard modelling and mapping in the medium valtellina,* Natural hazards and earth system sciences **11**, 1141 (2011).

[24] Q. Liang and A. G. L. Borthwick, *Adaptive quadtree simulation of shallow flows with wet-dry fronts over complex topography,* Computers and Fluids **38**, 221 (2009).

[25] A. Defina, *Two-dimensional shallow flow equations for partially dry areas,* Water Resources Research **36**, 3251 (2000).

[26] D. Yu and S. N. Lane, *Interactions between subgrid-scale resolution, feature representation and grid-scale resolution in flood inundation modelling,* Hydrological Processes **25**, 36 (2011).

[27] V. T. Chow, *Open-Channel Hydraulics* (McGraw-Hill International Editions, 1959) pp. 128–132.

[28] J. A. Cunge, F. M. Holly, and A. Verwey, *Practical aspects of computational river hydraulics* (Pitman Publishing Limited, 1980) pp. 19–23.

[29] B. C. Yen, *Open channel flow resistance,* Journal of Hydraulic Engineering-ASCE **128**, 20 (2002).

[30] G. S. Stelling and S. P. A. Duinmeijer, *A staggered conservative scheme for every froude number in rapidly varied shallow water flows,* International Journal for Numerical Methods in Fluids **43**, 1329 (2003).

[31] S. C. Kramer and G. S. Stelling, *A conservative unstructured scheme for rapidly varied flows,* International Journal for Numerical Methods in Fluids **58**, 183 (2008).

[32] H. W. J. Kernkamp, A. van Dam, G. S. Stelling, and E. D. de Goede, *Efficient scheme for the shallow water equations on unstructured grids with application to the continental shelf,* Ocean Dynamics **61**, 1175 (2011).

[33] S. Fagherazzi and D. J. Furbish, *On the shape and widening of salt marsh creeks,* Journal of Geophysical Research **106**, 911 (2001).

[34] G. Rosatti, D. Cesari, and L. Bonaventura, *Semi-implicit, semi-lagrangian modelling for environmental problems on staggered cartesian grids with cut cells,* Journal of Computational Physics **204**, 353 (2005).

[35] N. D. Volp, B. C. van Prooijen, J. D. Pietrzak, and G. S. Stelling, *A subgrid based approach for morphodynamic modelling,* Advances in Water Resources **93, Part A**, 105 (2016).

[36] J. A. Roelvink, *Coastal morphodynamic evolution techniques,* Coastal Engineering **53**, 277 (2006).

[37] D. P. Callaghan, F. Saint-Cast, P. Nielsen, and T. E. Baldock, *Numerical solutions of the sediment conservation law; a review and improved formulation for coastal morphological modelling,* Coastal Engineering **53**, 557 (2006).

[38] F. Benkhaldoun, I. Elmahi, S. Sari, and M. Seaid, *An unstructured finite-volume method for coupled models of suspended sediment and bed load transport in shallow-water flows,* International Journal for Numerical Methods in Fluids **72**, 967 (2013).

[39] M. van der Wegen and J. A. Roelvink, *Long-term morphodynamic evolution of a tidal embayment using a two-dimensional, process-based model,* Journal of geophysical research: Oceans (1978–2012) **113**, 1 (2008).

[40] A. Hibma, M. J. F. Stive, and Z. B. Wang, *Estuarine morphodynamics,* Coastal Engineering **51**, 765 (2004).

[41] B. Lin and S. N. Chandler-Wilde, *A depth-integrated 2d coastal and estuarine model with conformal boundary-fitted mesh generation,* International Journal for Numerical Methods in Fluids **23**, 819 (1996).

[42] V. Casulli and G. S. Stelling, *Semi-implicit subgrid modelling of three-dimensional free-surface flows,* International Journal for Numerical Methods in Fluids **67**, 441 (2011).

[43] P. J. Kinzel, C. J. Legleiter, and J. M. Nelson, *Mapping river bathymetry with a small footprint green lidar: Applications and challenges,* JAWRA Journal of the American Water Resources Association **49**, 183 (2013).

[44] A. Sehili, G. Lang, and C. Lippert, *High-resolution subgrid models: background, grid generation, and implementation,* Ocean Dynamics **64**, 519 (2014).

[45] G. S. Stelling, *Quadtree flood simulation with sub-grid digital elevation models,* Proceeding of the institution of civil engineers ICE **165**, 567 (2012).

[46] J. Hudson and P. K. Sweby, *A high-resolution scheme for the equations governing 2d bed-load sediment transport,* International Journal for Numerical Methods in Fluids **47**, 1085 (2005).

[47] W. Long, J. T. Kirby, and Z. Shao, *A numerical scheme for morphological bed level calculations,* Coastal Engineering **55**, 167 (2008).

[48] M. Colombini, G. Seminara, and M. Tubino, *Finite-amplitude alternate bars,* Journal of Fluid Mechanics **181**, 213 (1987).

[49] H. J. Vriend, *2dh computations of transient sea bed evolutions,* Coastal Engineering Proceedings **1**, 1698 (1986).

[50] H. K. Johnson and J. A. Zyserman, *Controlling spatial oscillations in bed level update schemes,* Coastal Engineering **46**, 109 (2002).

[51] A. B. Fortunato and A. Oliveira, *Improving the stability of a morphodynamic modeling system,* Journal of Coastal Engineering **SI50**, 486 (2007).

[52] G. R. Lesser, J. A. Roelvink, J. A. T. M. van Kester, and G. S. Stelling, *Development and validation of a three-dimensional morphological model,* Coastal Engineering **51**, 883 (2004).

[53] J. C. Warner, C. R. Sherwood, R. P. Signell, C. K. Harris, and H. G. Arango, *Development of a three-dimensional, regional, coupled wave, current, and sediment-transport model,* Computers & Geosciences **34**, 1284 (2008), predictive Modeling in Sediment Transport and Stratigraphy.

[54] D. de Vries, *Solving river problems by hydraulic and mathematical models* (Waterloopkundig laboratorium Delft, 1969).

[55] G. Galappatti and C. Vreugdenhil, *A depth-integrated model for suspended sediment transport,* Journal of Hydraulic Research **34**, 359 (1985).

[56] M. Garcia, *Sedimentation Engineering* (American Society of Civil Engineers, ASCE Libraries, 2008) Chap. 2.

[57] J. S. Ribberink, *Bed-load transport for steady flows and unsteady oscillatory flows,* Coastal Engineering **34**, 59 (1998).

[58] R. Bagnold, *An approach to the sediment transport problem from general physics,* US Geol. Surv. Prof. Paper **422**, 231 (1966).

[59] H. Talstra, G. S. Stelling, J. A. Roelvink, and A. Hibma, *Master thesis: Numerieke modellering van het lange termijn morfologische gedrag van estuaria*, Master's thesis, University of Technology Delft (2003).

[60] P. L. Roe, *Characteristic-based schemes for the euler equations,* Annual Review of Fluid Mechanics **18**, 337 (1986).

[61] M. Castro Díaz, E. Fernández-Nieto, A. Ferreiro, and C. Parés, *Two-dimensional sediment transport models in shallow water equations. a second order finite volume approach on unstructured meshes,* Computer Methods in Applied Mechanics and Engineering **198**, 2520 (2009).

[62] A. Siviglia, G. Stecca, D. Vanzo, G. Zolezzi, E. F. Toro, and M. Tubino, *Numerical modelling of two-dimensional morphodynamics with applications to river bars and bifurcations,* Advances in Water Resources **52**, 243 (2013).

[63] R. A. Callander, *Instability and river channels,* Journal of Fluid Mechanics **36**, 465 (1969).

[64] R. Schielen, A. Doelman, and H. E. De Swart, *On the nonlinear dynamics of free bars in straight channels,* Journal of Fluid Mechanics **252**, 325 (1993).

[65] D. Vanzo, A. Siviglia, G. Zolezzi, G. Stecca, and M. Tubino, *Interaction between steady and migrating bars in straight channels.* in *RCEM2011*, IAHR No. 7th, RCEM (Tsinghua University Press, Beijing, China., 2011) pp. 1–4.

[66] A. Crosato, F. B. Desta, J. Cornelisse, F. Schuurman, and W. S. J. Uijttewaal, *Experimental and numerical findings on the long-term evolution of migrating alternate bars in alluvial channels,* Water Resources Research **48**, 1 (2012).

[67] A. Defina, *Numerical experiments on bar growth,* Water Resources Research **39**, 1 (2003).

[68] A. Hibma, H. M. Schuttelaars, and H. J. de Vriend, *Initial formation and long-term evolution of channel-shoal patterns,* Continental Shelf Research **24**, 1637 (2004).

[69] F. Schuurman, W. A. Marra, and M. G. Kleinhans, *Physics-based modeling of large braided sand-bed river: Bar pattern formation, dynamics, and sensitivity,* Journal of Geophysical Research **118**, 2509 (2013).

[70] N. D. Volp, B. C. van Prooijen, J. D. Pietrzak, and G. S. Stelling, *A subgrid based approach for suspended sediment,* Unknown (2016).

[71] H. E. de Swart and J. T. F. Zimmerman, *Morphodynamics of tidal inlet systems,* Annual Review of Fluid Mechanics **41**, 203 (2009), http://arjournals.annualreviews.org/doi/pdf/10.1146/annurev.fluid.010908.165159 .

[72] European Commission, *Natura 2000, http : //ec.europa.eu/environment/nature/natura2000/index$_e$n.htm,* (2016).

[73] Z. Wang, P. Hoekstra, H. Burchard, H. Ridderinkhof, H. De Swart, and M. Stive, *Morphodynamics of the Wadden Sea and its barrier island system,* Ocean & Coastal Management **68**, 39 (2012).

[74] A. Collins, S. E. Allen, and R. Pawlowicz, *The role of wind in determining the timing of the spring bloom in the strait of georgia,* Canadian Journal of Fisheries and Aquatic Sciences **66**, 1597 (2009), http://dx.doi.org/10.1139/F09-071 .

[75] S. C. James, C. A. Jones, M. D. Grace, and J. D. Roberts, *Advances in sediment transport modelling,* Journal of Hydraulic Research **48**, 754 (2010), http://dx.doi.org/10.1080/00221686.2010.515653 .

[76] R. Marciano, Z. B. Wang, A. Hibma, H. J. de Vriend, and A. Defina, *Modeling of channel patterns in short tidal basins,* Journal of Geophysical Research: Earth Surface **110**, n/a (2005), f01001.

[77] M. van der Wegen and J. A. Roelvink, *Reproduction of estuarine bathymetry by means of a process-based model: Western Scheldt case study, The Netherlands,* Geomorphology **179**, 152 (2012).

[78] Q. Yu, Y. Wang, S. Gao, and B. Flemming, *Modeling the formation of a sand bar within a large funnel-shaped, tide-dominated estuary: Qiantangjiang Estuary, China,* Marine Geology **299**, 63 (2012).

[79] G. J. de Boer, J. D. Pietrzak, and J. C. Winterwerp, *SST observations of upwelling induced by tidal straining in the rhine ROFI,* Continental Shelf Research **29**, 263 (2009).

[80] L. Guo, M. van der Wegen, D. J. Roelvink, Z. B. Wang, and Q. He, *Long-term, process-based morphodynamic modeling of a fluvio-deltaic system, part I: The role of river discharge,* Continental Shelf Research **109**, 95 (2015).

[81] H. J. Vested, C. Tessier, B. B. Christensen, and E. Goubert, *Numerical modelling of morphodynamics, Vilaine estuary,* Ocean Dynamics **63**, 423 (2013).

[82] D. A. Edmonds and R. L. Slingerland, *Significant effect of sediment cohesion on delta morphology,* Nature Geoscience **3**, 105 (2010).

[83] M. Garcia and G. Parker, *Entrainment of bed sediment into suspension,* Journal of Hydraulic Engineering **117**, 414 (1991).

[84] R. L. Soulsby and J. S. Damgaard, *Bed load sediment transport in coastal waters,* Coastal Engineering **52**, 673 (2005).

[85] L. C. van Rijn, *Unified view of sediment transport by currents and waves. I: Initiation of motion, bed roughness, and bed-load transport,* Journal of Hydraulic Engineering **133**, 649 (2007).

[86] L. C. van Rijn, *Sediment transport, part II: Suspended load transport,* Journal of Hydraulic Engineering **110**, 1613 (1984).

[87] L. C. van Rijn, *Sediment transport, part I: Bed load transport,* Journal of hydraulic engineering **110**, 1431 (1984).

[88] S. Ikeda, *Closure to lateral bed load transport on side slopes,* Journal of Hydraulic Engineering **110**, 200 (1984).

[89] Z. B. Wang, *Theoretical analysis on depth-integrated modelling of suspended sediment transport,* Journal of Hydraulic Research **30**, 403 (1992).

[90] J. Van Veen, *Ebb and flood channel systems in The Netherlands tidal waters.* Journal of the Royal Dutch Geographical Society (KNAG) 67 (1950), translated in 2002, https://www.vssd.nl/hlf/f015.htm.

[91] C. Forester, *Higher order monotonic convective difference schemes,* Journal of Computational Physics **23**, 1 (1977).

[92] F. W. Platzek, G. S. Stelling, J. A. Jankowski, and J. D. Pietrzak, *Accurate vertical profiles of turbulent flow in z-layer models,* Water Resources Research **50**, 2191 (2014).

[93] A. de Brauwere, B. de Brye, S. Blaise, and E. Deleersnijder, *Residence time, exposure time and connectivity in the scheldt estuary,* Journal of Marine Systems **84**, 85 (2011).

[94] B. de Brye, A. de Brauwere, O. Gourgue, T. Kärnä, J. Lambrechts, R. Comblen, and E. Deleersnijder, *A finite-element, multi-scale model of the scheldt tributaries, river, estuary and rofi,* Coastal Engineering **57**, 850 (2010).

[95] "ASCE Task Committee on Hydraulics, Bank Mechanics, and Modeling of River Width Adjustment 1", *River width adjustment. i: Processes and mechanisms,* Journal of Hydraulic Engineering (1998).

[96] "ASCE Task Committee on Hydraulics, Bank Mechanics, and Modeling of River Width Adjustment 1", *River width adjustment. ii: Modeling,* Journal of Hydraulic Engineering (1998).

[97] M. Rinaldi and S. E. Darby, *9 modelling river-bank-erosion processes and mass failure mechanisms: progress towards fully coupled simulations,* Developments in Earth Surface Processes **11**, 213 (2007).

[98] V. Casulli and P. Zanolli, *Iterative solutions of mildly nonlinear systems,* Journal of Computational Applied Mathematics **236**, 3937 (2012).

[99] A. Blom, *Different approaches to handling vertical and streamwise sorting in modeling river morphodynamics,* Water resources research **44** (2008).

[100] B. C. van Prooijen, F. Montserrat, and P. M. Herman, *A process-based model for erosion of macoma balthica-affected mud beds,* Continental Shelf Research **31**, 527 (2011).

[101] M. A. Lucas Pardo, D. Sarpe, and J. C. Winterwerp, *Effect of algae on flocculation of suspended bed sediments in a large shallow lake. consequences for ecology and sediment transport processes,* Ocean Dynamics **65**, 889 (2015).

[102] F. W. Platzek, G. S. Stelling, J. A. Jankowski, R. Patzwahl, and J. D. Pietrzak, *An efficient semi-implicit subgrid method for free-surface flows on hierarchical grids,* International Journal for Numerical Methods in Fluids (2015), 10.1002/fld.4172, fld.4172.

[103] H. Khatter and V. Aggarwal, *Efficient parallel processing by improved cpu-gpu interaction,* in *Issues and Challenges in Intelligent Computing Techniques (ICICT), 2014 International Conference on* (2014) pp. 159–161.

[104] E. M. Follett and H. M. Nepf, *Sediment patterns near a model patch of reedy emergent vegetation,* Geomorphology **179**, 141 (2012).

[105] S. Fagherazzi, M. L. Kirwan, S. M. Mudd, G. R. Guntenspergen, S. Temmerman, A. D'Alpaos, J. Koppel, J. M. Rybczyk, E. Reyes, C. Craft, and J. Clough, *Numerical models of salt marsh evolution: Ecological, geomorphic, and climatic factors,* Reviews of Geophysics **50** (2012), 10.1029/2011RG000359.

[106] E. Horstman, M. Dohmen-Janssen, P. Narra, N.-J. van den Berg, M. Siemerink, T. Balke, T. Bouma, and S. Hulscher, *Wave attenuation in mangrove forests; field data obtained in trang, thailand,* Coastal Engineering Proceedings **1**, 40 (2012).

[107] J. Q. Yang, F. Kerger, and H. M. Nepf, *Estimation of the bed shear stress in vegetated and bare channels with smooth beds,* Water Resources Research **51**, 3647 (2015).

[108] V. Casulli, *A semi-implicit numerical method for the free-surface navier–stokes equations,* International Journal for Numerical Methods in Fluids **74**, 605 (2013).

[109] H. V. Wang, J. D. Loftis, Z. Liu, D. Forrest, and J. Zhang, *The storm surge and sub-grid inundation modeling in New York City during Hurricane Sandy,* Journal of Marine Science and Engineering **2**, 226 (2014).

Curriculum Vitæ

Nicolette Dominique Volp

08-03-1985	Born in Hellevoetsluis, The Netherlands.

Education

1997–2003	VWO, Edison College, Apeldoorn, The Netherlands
2003–2007	Bachelor in Physics, Utrecht University, The Netherlands
2007–2009	Master Meteorology, Physical Oceanography and Climate, Physics Department, Utrecht University, The Netherlands
2009–2016	PhD. Researcher Faculty of Civil Engineering & Geosciences Delft University of Technology, The Netherlands

List of Publications

Journal Articles

- De Swart, H.E. and Volp, N.D., *Effects of hypsometry on the morphodynamic stability of single and multiple tidal inlet systems*, Journal of Sea Research, 2012

- Ysebaert, T.J.W., Walles, B., Dorsch, C., Dijkstra, J., Troost, K., Volp, N. D., van Prooijen, B.C., De Vries, M., Herman, P. and Hibma, A., *Ecodynamic solutions for the protection of intertidal habitats: the use of oyster reefs*,Journal of Shellfish Research, 2012

- Volp N. D., van Prooijen B.C. and Stelling G.S., *A finite volume approach for shallow water flow accounting for high-resolution bathymetry and roughness data*, Water Resources Research, 2013

- Volp, N. D., van Prooijen, B. C. and Pietrzak J.D. and Stelling, G. S., *A subgrid based approach for morphodynamic modelling*, Advances in Water Resources, 2015

- Volp, N. D., van Prooijen, B. C. and Pietrzak J.D. and Stelling, G. S., *High resolution morphodynamic modelling using a subgrid based approach*, (to be submitted 2017)